PNNL-33651

Pacific Northwest
NATIONAL LABORATORY

WECC Wide-Area Oscillation Assessment and Trending Study Report

October 2022

R. Huang, U. Agrawal, N. Zhou (Binghamton University),
J. Follum, S. Wang, P. Etingov, Y. Chen, Z. Huang
A. Ghassemian (Office of Electricity, Department of Energy)
B. Barazesh, K Davis (Federal Energy Regulatory Commission)

U.S. DEPARTMENT OF
ENERGY

DISCLAIMER

PACIFIC NORTHWEST NATIONAL LABORATORY
operated by
BATTELLE
for the
UNITED STATES DEPARTMENT OF ENERGY
under Contract DE-AC05-76RL01830

Printed in the United States of America

Available to DOE and DOE contractors from the Office of Scientific and Technical Information,
P.O. Box 62, Oak Ridge, TN 37831-0062
www.osti.gov
ph: (865) 576-8401
fax: (865) 576-5728
email: reports@osti.gov

Available to the public from the National Technical Information Service
5301 Shawnee Rd., Alexandria, VA 22312
ph: (800) 553-NTIS (6847)
or (703) 605-6000
email: info@ntis.gov
Online ordering: http://www.ntis.gov

PNNL-33651

WECC Wide-Area Oscillation Assessment and Trending Study Report

October 2022

R. Huang, U. Agrawal, N. Zhou (Binghamton University),
J. Follum, S. Wang, P. Etingov, Y. Chen, Z. Huang
A. Ghassemian (Office of Electricity, Department of Energy)
B. Barazesh, K Davis (Federal Energy Regulatory Commission)

Prepared for
the U.S. Department of Energy
under Contract DE-AC05-76RL01830

Pacific Northwest National Laboratory
Richland, Washington 99352

Executive Summary

With the high penetration of renewable energy sources (RES), conventional synchronous generators with rotating mass are being displaced by inverter-based resources (IBRs) to meet mandates such as Renewable Portfolio Standards (RPS). The inherent properties and characteristics of the transitioned generation mix may significantly impact the grid behavior. Therefore, it is of paramount significance that the impact and the consequences of the resource mix transition is thoroughly understood to adopt measures to maintain reliable grid operations. For example, without mitigatory measures, the increased penetration of IBRs may lead to a decrease in system inertia. This among other effects, may also impact the inter-area low-frequency oscillatory behavior of the system. These inter-area low-frequency oscillations could propagate through a large region, and may have a system-wide impact. Such system-wide oscillations may lead to unnecessary or inadvertent tripping of generators that are simply reacting to oscillations originating from geographically remote sites. This may lead to cascading outages, system splits, or load shedding events as experienced in the past[1][2][3]. A summary of some of the system wide oscillation events observed over the past few years has been provided in the North American Electric Reliability Corporation (NERC) reports[1][2][3]. NERC has also published white papers[1][2][3] that summarize the wide-area oscillation modes of the three US interconnections, and recently one of its recent reports provides guidelines for monitoring and managing oscillations. The Western Electricity Coordinating Council (WECC) has also performed comprehensive analysis of the small-signal stability and system-wide oscillations of the western interconnection following the 1996 blackout event[4]. WECC continues to study and analyze system-wide oscillations[5]. These efforts have been assisted significantly by the increased deployment of phasor measurement units (PMUs) across the WECC over the past 20 years. Despite these efforts, however, no comprehensive analysis has been performed to-date to understand the impact of the on-going resource mix transition and to capture and analyze the patterns of change in system wide-area oscillatory behavior and modal properties.

This project, titled Wide-area Oscillation Assessment and Trending Study and sponsored by the Office of Electricity (OE) of the Department of Energy (DOE), aims to conduct the required research to capture and analyse the on-going changes in wide-area oscillatory behavior of the system. The Pacific Northwest

---

[1] https://www.nerc.com/pa/rrm/ea/Documents/January_11_Oscillation_Event_Report.pdf
[2] https://www.nerc.com/comm/PC/SMSResourcesDocuments/Interconnection_Oscillation_Analysis.pdf
[3] https://www.nerc.com/pa/rrm/ea/System%20Disturbance%20Reports%20DL/1996SystemDisturbance.pdf
[4] D. N. Kosterev, C. W. Taylor and W. A. Mittelstadt, "*Model validation for the August 10, 1996 WSCC system outage*," in IEEE Transactions on Power Systems, vol. 14, no. 3, pp. 967-979, Aug. 1999, doi: 10.1109/59.780909.
[5] https://www.wecc.org/Reliability/Modes%20of%20Inter-area%20Power%20Oscillations%20in%20the%20WI.pdf

National Laboratory (PNNL) conducted this research and technical staff of Federal Energy Regulatory Commission (FERC) served as advisors to the project. The primary objective of this study is to assess whether there are significant change patterns in the wide-area oscillatory behavior of the interconnection as a result of the changing generation mix. The work performed in this project is complimentary to previous and on-going work by NERC and others in the industry; the study covers the aspects that have not been studied previously, and the analysis can serve as an informational guide in future grid planning and system operation considerations.

The research conducted in this project, first thorough a data-based method, identifies the variation trends in system performance using recorded data. Thereafter, it evaluates the oscillation behavior of the future WECC system using a model-based approach, in order to validate the employed models against the actual system performance. The work performed includes the following:

1. Field PMU data was collected from the Bonneville Power Administration (BPA) area of the WECC system, from 06/30/2018 to 10/01/2019 (15 months) with a sampling rate of 30 frames per second. The frequencies and damping ratios (DR) of the two dominant inter-area modes were estimated using the field-collected PMU data. Data for solar, wind, conventional generation, and load in the WECC system were collected from the Energy Information Administration (EIA, 2019) for the same period the PMU data was collected over.

2. Advanced statistical methodologies were used to extract the significant trends between the system operating conditions and two dominant inter-area oscillation modes for the WECC system at the system performance level.

3. The observed trends based on the historical PMU data and system operation conditions were cross-checked against results obtained from analytical models.
4. Tools were developed to populate/increase renewables at different locations with different penetration levels for WECC systems.
5. Multiple future resource mix scenarios with different renewable penetrations were developed through close collaboration with several WECC working groups. Also, the developed future resource mix scenarios with detailed power flow and dynamic models were analyzed using Prony-based and eigenvalue-based methods to extract the trends in the wide-area oscillatory behavior with respect to the future generation-mix changes. The analysis tasks were performed using industry popular software packages PowerWorld and SSAT of PowerTech's DSA Tools.

The findings of the oscillation trending analysis are summarized as follows:

1. The damping ratio (DR) of one of the WECC inter-area modes will decrease with the increase of RES penetration level.

2. The DRs of two of the WECC inter-area modes will decrease with the increase of California-Oregon-Intertie (COI) power flow (from north to south).

3. The impact of increased RES penetration level is highly dependent on which conventional synchronized resources are being retired and the location of the replacing RES. This observation is of great significance. Based on this observation, before retirement of a conventional synchronized plant and the associated controls, a thorough analysis needs to be performed to make sure that required measures are planned in in order to maintain reliable oscillatory behavior of the system.

As shown in Figure ES-1, our study contains four main tasks as follows:

Task 1: Collecting past/future generation mix and load data for the WECC system. More than one year of data for solar, wind, conventional generation, and load in the WECC system were collected from the U.S. Energy Information Administration (EIA, 2019). This data was leveraged for further trending analysis.

Task 2: Collecting historical ambient phasor data (PMU measurements) of the WECC system and performing oscillation detection and analysis using the Mode Meter tool to scan the collected ambient phasor data and estimate the dominant wide-area oscillation modes of the WECC system.

Task 3: Evaluating how different factors (e.g., renewable penetration levels, load levels) could impact the inter-area oscillation modes by correlating oscillation modal information obtained in Task 2 to determine the oscillation trends with respect to generation/load mixes obtained in Task 1. The correlation analysis is performed under a statistical framework, which can quantify the uncertainty of the correlation analysis with a confidence level.

Task 4: Performing model-based wide-area oscillation assessment with respect to future grid scenarios having a high penetration level of RES for the WECC system. Past WECC operating models were collected and model-based wide-area oscillation assessment was carried out to validate results obtained using data-based oscillation assessment and trending analysis results from Task 2 and Task 3. Furthermore, model-based analysis was extended to study and correlate future system oscillation trends with multiple future generation-mix scenarios at different penetration level of RES. The future

generation-mix scenarios we have investigated include: (1) Systemwide increase in RES penetration level (up to 70% in the whole WECC); (2) Systemwide increase in the RES penetration level but reversing the order in which a group of generators were replaced in several cases; (3) Increase in RES penetration level in Alberta only; (4) Increase in RES penetration level throughout the system except in Alberta; and (5) Decrease in the power flow from north to south caused by an increased RES generation in the south of WECC. A detailed eigenvalue analysis was carried out to have a better understanding of the trends observed in the system modes for these scenarios.

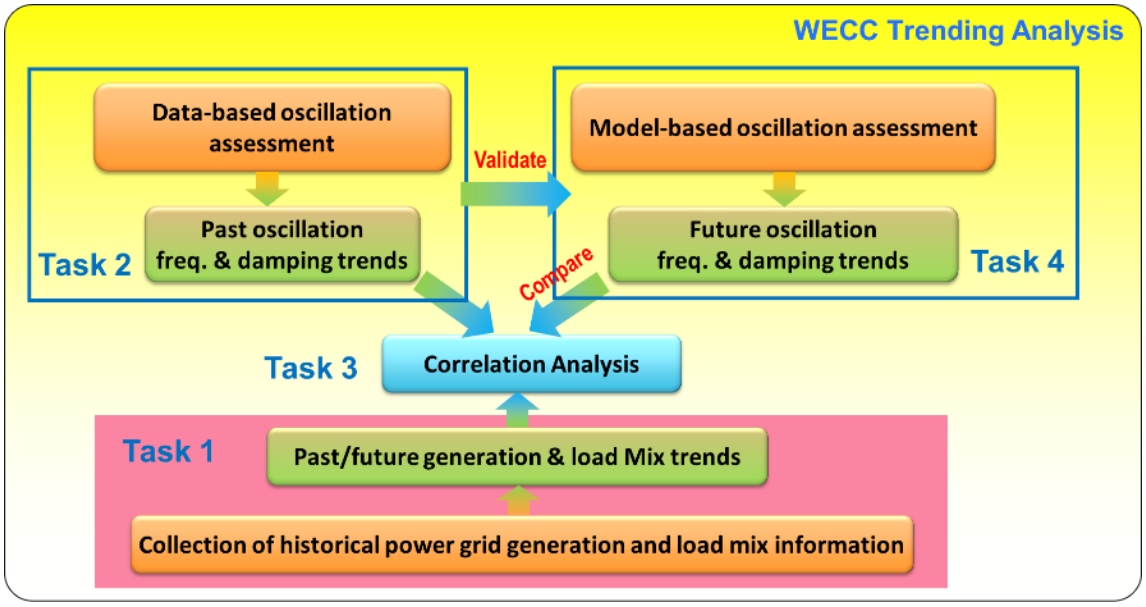

Figure ES-1. Methodology for wide-area oscillation assessment and trending study.

The **data-based analysis** results of the correlation between the dominant wide-area oscillation modes and different impact factors, such as solar generation, wind generation, system load level, and COI power flow, are summarized in Table ES-1. The observation includes:

- The DR of mode North-South Mode A (NS-A) will decrease with the increase of the penetration level of solar and wind generation.
- The DR of both modes NS-A and North-South Mode B (NS-B) will decrease with the increase of the COI power flow (from north to south).
- Impact from the increase of penetration level of the solar and wind generation on the DR of NS-B is not conclusive; in other words, the data-based correlation analysis does not show a strong correlation between the DR of NS-B and the solar and wind generation penetration level.

It should be noted that the data-based correlation analysis can only identify the phenomena that occurred during the observed duration. It should also be noted that the results represent correlation and do not necessarily indicate causality.

Table ES-1 Impact of mixed generation on inter-area oscillation modes (**data-based assessment**).

Increased Variables	Damping Ratio (%)		Frequency (Hz)	
	NS-A	NS-B	NS-A	NS-B
Solar	Decrease	Inconclusive	Decrease	Decrease
Wind	Decrease	Inconclusive	Increase	Increase
Load	Inconclusive	Increase	Decrease	Decrease
COI flow	Decrease	Decrease	Increase	Inconclusive

Table ES-2 summarizes the **model-based wide-area oscillation assessment** with respect to future operation scenarios with high RES penetration for the Heavy Summer (HS) load WECC model. Five different scenarios of future generation-mix scenarios are investigated: (1) systemwide RES high-penetration level up to 70% in the whole WECC system – Scenario S1; (2) Scenario S1 but reversing the order of generators replaced – Scenario S2; (3) Increase of renewable penetration level in Alberta only – Scenario S3; (4) Increase of renewable penetration in all areas except Alberta – Scenario S4; (5) significant decrease in the COI flow from north to south caused by an increased RES generation in the south of WECC – Scenario S5.

As shown in Table ES-2:

- For NS-A, the systemwide RES generation increase will change the damping ratio for Scenarios S1 and S2 depending on which generators are replaced. For Scenario S1, the damping ratio

initially did not change much and then it decreased sharply. The trend reversed by reversing the order of replacing generators in Scenario S2.

- For NS-A, increasing renewable penetration level only in Alberta will result in decreased damping ratio.
- For NS-A, increasing renewable penetration throughout the system except in Alberta decreases the damping ratio slightly.
- For NS-A, the DR will increase if COI flow decreases from north to south as a result of an increased RES generation in the south of WECC.
- For NS-B, the generation-mix change with high RES penetration does not have a significant impact on the damping ratio.

For the model-based study, the trends observed in the damping ratio and frequency of modes cannot be directly related to the renewable penetration level or system inertia. These trends are in fact determined by which generators are replaced, as well as how remaining synchronous generators interact among each other with respect to their mode shape and participation factor.

Table ES-2. Summary of impact of RES penetration level increase on the inter-area oscillation modes – **model-based assessment**.

Scenarios	Damping Ratio (%)		Frequency (Hz)	
	NS-A	NS-B	NS-A	NS-B
Systemwide RES increase (S1, S2)	Depends on generator being replaced	Not significant	Increase	Increase
Area-specific RES increase in Alberta only (S3)	Decrease	Not significant	Increase	Increase
Systemwide increase in all areas except in Alberta (S4)	Depends on generator being replaced	Not significant	Increase	Increase
Increase in RES in south and decrease in COI + PDCI flow (S5)	Increase	Not significant	Decrease	Not significant

The trends obtained based on data-based assessment, which is summarized in Table ES-1, can be explained based on the carried-out model-based detail assessment, results of which are summarized in Table ES-2. The decreasing trend of damping ratio of NS-A with increased solar and wind generation indicates that the specific group of generators that are taken offline when renewable generation is high results in the decrease of the damping ratio of NS-A. The trend observed in the damping ratio and frequency of NS-A with increased COI flow aligns well with the model-based assessment results.

Acknowledgments

The project team at PNNL would like to acknowledge the funding supports from DOE Office of Electricity Advanced Grid Modeling (AGM) program, and continued feedback and comments from the project technical advisors.

In addition, the project team is grateful to Bonneville Power Administration for providing measurement data and to Jeff Banning of PNNL for his help accessing the data.

The authors also acknowledge our colleagues Dr. Xiaoyuan Fan, Dr. Frank Tuffner, Dr. Shuchismita Biswas, and Dr. Hisham Mahmood at Pacific Northwest National Laboratory for their support, comments, and review of this work.

Acronyms and Abbreviations

3D	three dimensional
BANC	Balancing Authority of North California
BPA	Bonneville Power Administration
CDF	cumulative distribution function
COI	California-Oregon Intertie
DR	damping ratio
DER	distributed energy resource
EIA	U.S. Energy Information Administration
EIOC	Electric Infrastructure Operation Center
HS	heavy summer
IBR	inverter based resources
LS	light summer
LSR	least-square regression
MAD	median absolute deviation
NERC	North American Electric Reliability Corporation
NS-A	North-South Mode A
NS-B	North-South Mode B
PDCI	Pacific Direct Current Intertie
PDF	probability distribution function
PMU	phasor measurement unit
PNNL	Pacific Northwest National Laboratory
PV	photovoltaic
QR	quantile regression
RES	renewable energy sources
RPS	renewable portfolio standards
SMS	Synchronized Measurement Subcommittee
WECC	Western Electricity Coordinating Council
WI	Western Interconnection

Contents

Figures

Tables

1.0 Introduction

Several states throughout the United States have developed renewable portfolio standards (RPS) to address the need for clean, sustainable, and renewable energy. The RPS are expected to structurally alter the characteristics of the power systems. The RPS mandates have required some states to increase their level of renewable generation to up to 100% by the year 2045 (Sierra, 2019). Hence, large-scale power generation from renewable resources is no longer a vision but a foreseeable reality. As more inverter-based renewable systems are installed in existing grids, more conventional generation units may be displaced. With these unprecedented rapid changes, special measures may be required to accommodate needs of the future power systems. It is of great necessity that these new changes and their impact be thoroughly investigated to help maintain reliable grid operations. For example, the increase in penetration of IBRs may lead to a decrease in system inertia if mitigatory measures are not adopted. This among many factors, may also impact the inter-area low-frequency oscillatory behavior of the system.

Oscillations are always present in the bulk power system due to the electromechanical nature of the electric grid. Under no significant external influence on the system, the grid still oscillates at its natural frequencies for small disturbances such as constant changes in load. These oscillations are usually well-damped and contained; however, growing or high-energy oscillations can present system instability, potential equipment damage, safety concerns, and power quality issues. In addition to these natural oscillations, forced or "rogue" inputs to the system can also cause oscillations and should be detected and mitigated to the extent possible. To explain these concepts of oscillations on the bulk power system, it is important to clearly differentiate between the types of electromechanical oscillations that are present. From a practical standpoint, power system oscillations can be categorized as follows (NERC, 2019b):

- **System (Natural)**: low-frequency rotor angle oscillations caused by instantaneous power imbalances. These are often differentiated further as follows:
    - **Local**: oscillations where one power plant or generating unit oscillates with the rest of the system, generally caused by heavy loading and generator controls
    - **Intra-plant**: oscillations where generating units within a power plant oscillate with each other at the same location, generally caused by poor tuning, unit control interactions, and unit operating modes

    - **Inter-area**: oscillations characterized by several coherent units or parts of the system oscillating against other groups of machines, often predominant in power systems with relatively weaker inter-area connections

    - **Torsional**: high frequency oscillations caused by resonance conditions between highly compensated transmission lines and the mechanical modes of a steam-turbine generator (typically referred to as sub-synchronous resonance).

- **Forced**: sustained oscillations driven by external inputs to the power system, such as unexpected equipment failures, control interactions, or abnormal operating conditions that can occur at any frequency.

The nature of those System oscillations is characterized by their frequency and damping ratio. Damping ratio plays a critical role for the inter-area oscillations as it determines the decay rate of the oscillation magnitude and thus indicates whether the inter-area oscillation is stable or not. The inter-area low-frequency oscillations usually propagate through a large region and have systemwide impact. These oscillations may lead to unnecessary or inadvertent tripping of generators that are reacting to the oscillations originating from geographically remote sites. Such tripping of generators can lead to cascading outages, system splits, and load-loss events. In recent years, several systemwide oscillation events have been observed across the interconnections of the North American Electric Reliability Corporation (NERC, 2017), (NERC, 2019a), (NERC, 2019b). Forced or "rogue" inputs to the system can also cause oscillations and if a forced oscillation occurs near the frequency of an inter-area natural oscillation mode that has weak damping, the forced oscillation can "excite" the inter-area natural oscillation mode so the oscillations propagate through wide geographical areas where the system mode is active. Under certain circumstances, the interactions can also lead to a "resonance" effect, resulting in systemwide oscillations that are much larger than oscillations at the source. In this case, even small oscillatory inputs can induce larger, systemwide oscillations from resonance amplification (NERC, 2019a), (NERC, 2017), (Quint, 2019). It is very critical for the power grid to sustain certain damping ratio for its wide-area low-frequency natural oscillation modes, to avoid such kind of "resonance" effect.

The wide-area proliferation of phasor measurement units (PMUs) across each of the North American interconnections over the past decade and the use of other types of disturbance monitoring equipment have facilitated monitoring and analysis of systemwide oscillations. Since 2015, based on a certain technical criterion, the NERC Synchronized Measurement Subcommittee (SMS) judiciously selects events for analysis of inter-area oscillatory modes or other oscillatory anomalies on the system (NERC,

2019b) (NERC, 2019a), coordinating with the regional entities and reliability coordinators to collect wide-area PMU data. A recent report by NERC (NERC, 2019b) summarizes the analysis of a total of 19 such oscillatory events in all three interconnections (seven Eastern, five Texan, and seven Western) in 2016 and 2017. In addition, an Eastern Interconnection event on January 11, 2019, was published by NERC SMS (Quint, 2019). At present, information of the past oscillatory events is based on published NERC material that includes only the events selected by NERC SMS for analysis but not all of the occurrences or near misses of the selection criteria. Such events are not in the direct purview of the current version of the Reliability Standards.

The impact of renewable generation on power system wide-area oscillations may be attributed to various aspects, but the findings of existing literature are not consistent. For example, the New England and New York test system was used to investigate the renewable generation impact on its established inter-area oscillation mode. It was found that renewable generation could detrimentally affect the inter-area oscillation mode as photovoltaic (PV) integration results in larger angular separation among synchronous generators (Shah, Mithulananthan, & Bansal, 2013). Furthermore, using small signal analysis and transient simulation, the study in (Eftekharnejad, Vittal, Heydt, Keel, & Loehr, 2013) indicated that the increase of utility scale and residential renewable may decrease damping of inter-area oscillation modes due to reduced system inertia. However, other studies have found it is also possible that renewable integration could improve small-signal stability. For example, the study in (Shah R. , Mithulananthan, Sode-Yome, & Lee, 2010) concluded that renewables could increase oscillation damping because it adds damping to critical modes, and the scattered integration pattern is more beneficial than the concentrated pattern. Other studies that have similar findings include (Tamimi, Cañizares, & Bhattacharya, 2011) and (Shah, Mithulananthan, & Bansal, 2012). Additionally, other literature observed both beneficial and detrimental influence of renewable on oscillations. A study by (Du, Wang, & Dunn, 2009) looked at the impact of increased renewables on system small-signal stability based on a single-machine infinite-bus system. It found that renewable resources could either have positive or negative impact on oscillation damping, with similar findings in (Quintero, Vittal, Heydt, & Zhang, 2014) and (Elliott, Byrne, Ellis, & Grant, 2014). The operation limit of renewable generation also plays a significant role on the contribution of damping torque. Evidently, the impact of renewable penetration level on power system inter-area oscillations is not yet well understood. (Elliott, Byrne, Ellis, & Grant, 2014) and (You, et al., 2017) evaluated the impact of PV generation on the wide-area oscillation modes for the Western Electricity Coordinating Council (WECC) and Eastern Interconnection (EI) systems by incrementally displacing synchronous generators with PV in the system dynamic model and investigating how the dynamics of PV affect inter-area oscillation frequency and damping ratio (DR). Since there are so many factors that may

play a role in this phenomenon, the impact of renewable on inter-area oscillations may need to be studied on a case-by-case and system-by-system basis at this stage. All of the above existing reports and papers, investigating the impact of renewable penetration level on power system inter-area oscillations, only used model-based analysis and do not validate the results with the existing system data.

The WECC has spent significant efforts in understanding the oscillatory behavior of the interconnection due to the small-signal stability risks experienced in the 1996 blackout event and continued oscillatory risks during highly stressed operating conditions. With the high penetration of RES with less inertia, more attention has been brought to the currently unknown nature of the potential impact on system modal properties and wide-area oscillatory behaviors in the WECC system. The wide-area deployment of PMUs across the WECC over the past 20 years has facilitated monitoring and analysis of systemwide oscillations. However, no analyses have been performed comprehensively to understand the impact of the ongoing power system resource mix transition on wide-area oscillatory behaviors in the present and future WECC system.

This report presents a comprehensive oscillation trending analysis methodology that can potentially guide future grid planning and operation under high penetration of RES and provide a set of tools and procedures for future oscillation assessment and analysis. This report focuses on assessing whether there are significant trends in WECC wide-area oscillatory behaviors at the WECC system performance level with respect to generation-mix changes brought by the increased penetration of RES. The work performed in this report is complimentary to previous work and is covering the research area of investigating trended system behavior and looking at the potential future impact of various resource mix change scenarios on the WECC system, which is not covered by previous works.

In this report, we present how the changes in generation-mix can impact frequency and DR of WECC dominant wide-area oscillation modes. Thorough data-based and model-based analyses have been carried out to determine current trends, and have been extended to evaluate oscillation behaviors of the future WECC system. The WECC PMU data, as well as the WECC generation-mix data, have been collected and analyzed to find out the correlation and determine past trends between the penetration level of RES and the wide-area oscillation modes in the WECC system. Past WECC operation models have also been collected and a model-based wide-area oscillation assessment has been conducted to validate the data-based oscillation assessment and trending analysis results. Furthermore, model-based analysis has been extended to study and correlate future system oscillation trends with multiple future generation-mix scenarios with a very high penetration level of RES. The future generation-mix scenarios investigated include: (1) Systemwide increase in RES penetration level (up to 70% in the whole WECC); (2)

Systemwide increase in the RES penetration level but reversing the order in which a group of generators were replaced in several cases (3) Increase in RES penetration level in Alberta only; (4) Increase in RES penetration level throughout the system except in Alberta and (5) Decrease in the power flow from north to south caused by an increased RES generation in the south of WECC. Both the data-based and model-based trending analyses show that high penetration of RES has a significant impact on the wide-area oscillation modes in WECC.

2.0 Objective and Methodology

2.1 Objective

The primary objective of this study is to assess whether there are significant trends in the wide-area oscillatory behaviors with respect to the the significant generation-mix changes brought by the increased penetration of RES in the WECC system. Our primary motivation is the currently unknown nature of the potential impact of ongoing power system transition on system modal properties and wide-area oscillatory behavior, as no analyses have been performed comprehensively. The trending analysis presented in this report can serve as reference for future grid planning and operation of the WECC system.

With the high penetration of RES, conventional synchronous generators having rotating mass are being displaced by inverter-interfaced and inertia-less RES to meet the mandates set by RPS. The new uncertainties and dynamics of these generation-mix changes have significant impact on grid behaviors, and it is necessary to be thoroughly investigated, which can help maintain reliable grid operations. As the increase of inverter-interfaced RES generation will reduce the system's inertia, of great concern is the inter-area low-frequency oscillation that usually propagates through a large region and has systemwide impact. Such oscillations may lead to unnecessary or inadvertent tripping of generators that are reacting to the oscillations originating from geographically remote sites. Tripping of generators can lead to cascading outages, system splits, and load-loss events as experienced in the past. In recent years, several systemwide oscillation events have been observed across interconnections as summarized in the recent NERC reports (NERC, 2019b) (NERC, 2019a) (NERC, 2017) (Quint, 2019).

2.2 Methodology

We performed both data-based and model-based correlation analyses for the wide-area oscillation assessment and trending study of WECC. As shown in Figure 2-1, the wide-area oscillation assessment and trending study contains four main tasks as follows.

Task 1: Collecting past/future generation and load data for the WECC system. Data for solar, wind, conventional generation, and load in the WECC system were collected from the U.S. Energy Information Administration (EIA) (EIA, 2019). These data were parsed and preprocessed for further analysis.

Task 2: Collecting historical ambient phasor data (PMU measurement) of the WECC system and performing oscillation detection and analysis using the Mode Meter tool to scan collected ambient phasor data and estimate the dominant wide-area oscillation modes of WECC system.

Task 3: Evaluating how different factors (e.g., renewable penetration levels, load levels) could impact the inter-area oscillation modes by correlating oscillation modal information obtained in Task 2 to determine the oscillation trends with respect to generation/load mixes obtained in Task 1. The correlation analysis is performed under a statistical framework, which can quantify the uncertainty of the correlation analysis to describe how much confidence can be placed on the results.

Task 4: Performing a model-based wide-area oscillation assessment with respect to future operation scenarios with a high-penetration level of RES for the WECC system. Past WECC operation models have been collected and model-based wide-area oscillation assessment conducted to validate against the data-based oscillation assessment and trending analysis results from Task 2 and Task 3. Furthermore, model-based analysis has been extended to study and correlate future system oscillation trends with multiple future generation-mix scenarios with a very high penetration level of RES. The future generation-mix scenarios we have investigated include: (1) systemwide increase in RES penetration level (up to 70% in the whole WECC); (2) Increase in RES penetration level in specific areas only, such as Alberta and California; (3) Increase in RES penetration level throughout the system except in Alberta and (4) significant decrease in the power flow from north to south caused by an increased RES generation in the south of WECC. The following sections give detailed description for the methodologies used and the results obtained in the four tasks.

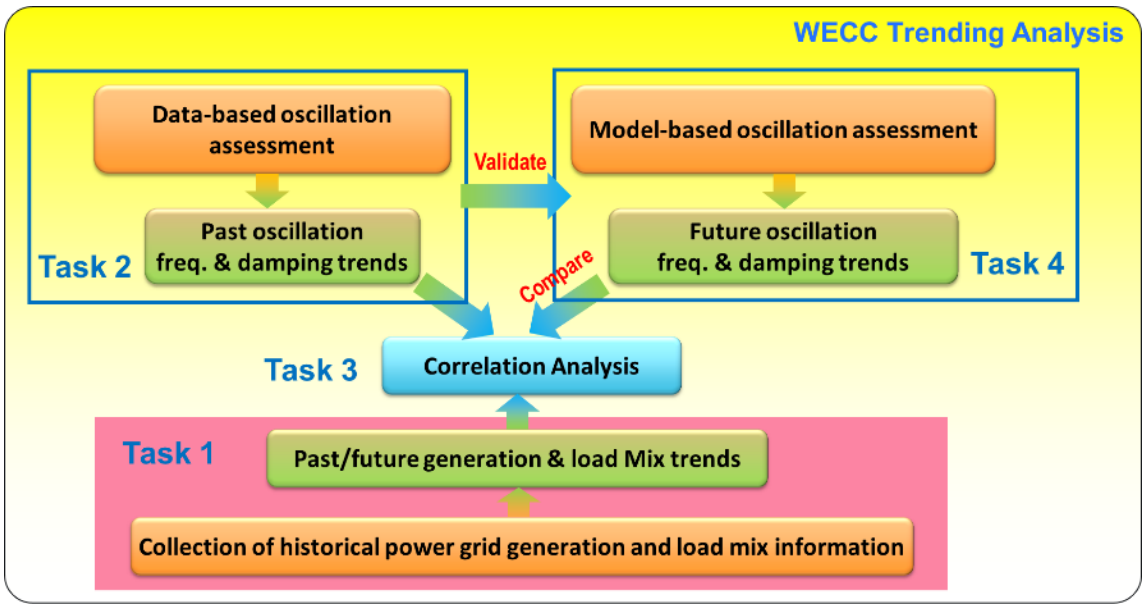

Figure 2-1. Methodology for wide-area oscillation assessment and trending study.

3.0 WECC Generation and Load-Mix Data Collection and Analysis

In recent years, significant changes have been observed in generation and load mix throughout the United States, particularly the increased proportion of solar and wind energy. As these renewable generation sources are highly intermittent in nature, system operating conditions change through the day depending on the variability observed in solar irradiance and wind. This section presents the analysis conducted to identify trends in generation/load mix in recent years using real-world data. Data sources, data processing, and the methodology used for generation/load data collection and assessment are described next. This analysis helped to understand the wide range of operating conditions observed in the WECC grid in recent years, which were then used for the data-based oscillation assessment.

3.1 Data Source

Data for solar, wind, conventional generation, and load in the WECC system were collected from the EIA (EIA, 2019). These data were parsed and preprocessed for further analysis. The resulting data files after the preprocessing are summarized in Table 3-1.

Table 3-1. Summary on Preprocessed Data File

Filenames	Description	Starting Date	Ending Date	Resolution
dataSolar2019110408.mat	WECC Solar Generation	06/30/2018	10/01/2019	60 minutes; Control Area
dataWind2019102916.mat	WECC Wind Generation	06/30/2018	10/01/2019	60 minutes; Control Area
dataCoal20180630_20191001.mat	WECC Coal Generation	06/30/2018	10/01/2019	60 minutes; Control Area
dataHydro20180630_20191001.mat	WECC Hydro Generation	06/30/2018	10/01/2019	60 minutes; Control Area
dataNG20180630_20191001.mat	WECC Natural Gas Generation	06/30/2018	10/01/2019	60 minutes; Control Area
dataOil20180630_20191001.mat	WECC Oil Generation	06/30/2018	10/01/2019	60 minutes; Control Area
dataOther20180630_20191001.mat	WECC Other Generation	06/30/2018	10/01/2019	60 minutes; Control Area
dataLoad2019102916.mat	WECC Load Data	06/30/2018	10/01/2019	60 minutes; Control Area
data_renewable.mat	WECC Percentage of Renewable Generation	06/30/2018	10/01/2019	60 minutes; Control Area

The spatial resolution of these data sets is a control area. The covered areas are divided into three regions: Northwest Region, Southwest Region, and California Region, which have 21, 10, and 5 control areas,

respectively. A screenshot of the map for the control areas is shown in Figure 3-1[1]. The renewable generation data (including solar and wind) were first recorded on 06/30/2018. Thus, a 15-month data was collected from 06/30/2018 to 10/01/2019. The temporal resolution of the original data is 60 minutes. The time tag of the data was originally recorded in Coordinated Universal Time zone and converted into Western time zone (i.e., America/Los Angeles time) so the daily cycles can be better revealed.

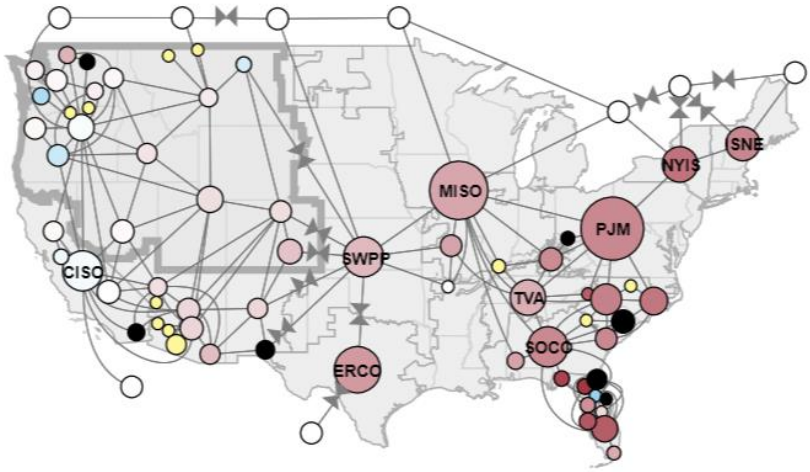

Figure 3-1. Control areas in the US power systems (retrieved from eia.gov[1]).

3.2 Data Preprocessing

The raw data downloaded from the EIA website (eia.gov) may require curation. Missing data and outliers were firstly identified by visually inspecting the time-series plot, as illustrated in Figure 3.2. The missing data are marked as "NAN" (i.e., not a number) and are easily identified and removed from the database to reduce their negative impact on the correlation analysis. The missing data could be caused by temporary communication failure or faulty remote terminal units. Unlike missing data, outliers are not marked in the database. Outliers are data points abnormally far away from normal observations. Outliers could be caused by temporary sensor failure or electrical disturbance and interference. Outliers must be carefully identified and removed, or they will cause detrimental impacts on the statistical analysis (e.g., correlation analysis).

Because of the randomness of the observation data, identifying outliers is performed under a statistical framework designed to balance the risks of false and missing outliers. A false outlier is a normal data point mistakenly identified as an outlier. A missing outlier is mistakenly identified as a normal data point. In this study, outliers were identified for each area using the following two methods in series.

[1] https://www.eia.gov/electricity/gridmonitor/dashboard/electric_overview/regional/REG-NW

3.2.1 Statistical Metric Method

Because of the randomness of solar generation, outliers in the data were identified using statistical metrics. The median and median absolute deviation (MAD) were used instead of mean and standard deviation because they are more robust in identifying outliers (Leys, Ley, Klein, Bernard, & Licata, 2013). The procedure outlined below was followed to identify outliers.

(a) Categorize data into different groups with similar distributions. The goal is to increase the detectability of outliers by reducing the variance within a group. For example, solar generation is categorized into 24 groups, which corresponds to 24 hours of a day. Notice that variations of solar generation at a certain hour are smaller than those within a day.

(b) Calculate the median of the data within a group, i.e., $\bar{X} = median(X), X = \{X_i | X_i \in Group\}$.

(c) Calculate the MAD, i.e., $MAD = median(|X_i - \bar{X}|)$. Note that for Gaussian distribution, the standard deviation is σ) $\sigma = 1.4826 \cdot MAD$.

(d) Detect an outlier by comparing its distance from the median value ($\bar{X}$) and a scaled MAD, i.e., $X_i \; is \begin{cases} an\ outlier & if\ |X_i - \bar{X}| \geq s \cdot MAD \\ not\ an\ outlier & if\ |X_i - \bar{X}| < s \cdot MAD \end{cases}$. Here, *s* is a scaling factor that determines how much risk one wants to take in assigning a false outlier. For example, in Gaussian distribution, setting $s = 3 \cdot 1.4826 = 4.45$ gives the boundary of 3σ, which assigns a risk of the false outlier at 0.3%.

In this study, *s* was set to 6 using trial and error to balance the risk between false and missing outliers.

3.2.2 Sanity-Check Method

When visually inspecting the plot of the figure, some irrational data were also identified. For example, the solar generation in the Balancing Authority of North California (BANC) area stay the same for over 8 days from 03/29/2019 13:00 through 04/06/2019 22:00 at 156 MW (https://www.eia.gov/electricity/data/browser/). The data are irrational because it is impossible for the solar generation to stay at the same level for so long and especially during the nighttime. This might have been caused by a bug in the data recording system, thus a script was written to remove the portion of data that did not change over 3 consecutive hours.

To illustrate the effectiveness of the proposed outlier identification procedure, the solar generation from the BANC area is shown in Figure 3-2. The first row of the subplots are raw data downloaded from the EIA website. The second row of the subplots are preprocessed data with identified outliers removed. It can be observed in the top-left subplot that several outliers were identified in the time-series plot. These outliers were more obvious in the box-whisker plot in the top-middle after the data were categorized into

24 groups according to hours of a day. The color-coded three-dimensional (3D) scatter plot in the third column reveals the daily trend of solar generation over the years. After the outliers were removed, the data are more consistent in their distributions over time. Similar observations were made over other data and not shown here to stay concise.

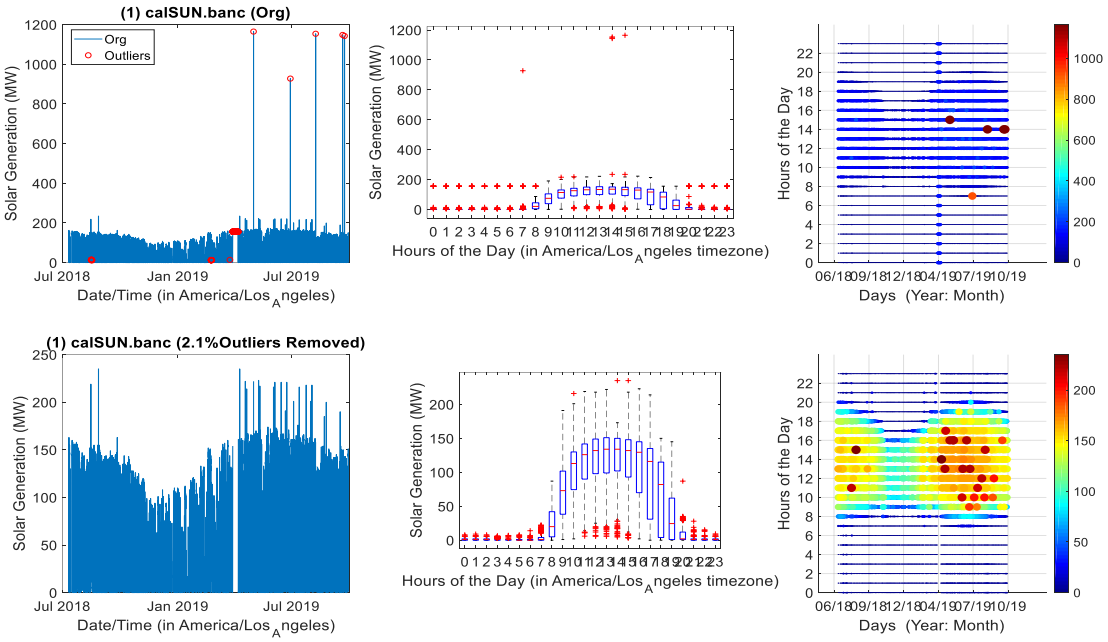

Figure 3-2. Time-series (first column), box-whisker (second column), and heat-map (third column) plots of the solar generation from the BANC region before (first row) and after (second row) preprocessing.

3.3 Trends Observed in Load and Generation

This subsection provides a detailed description of identified trends observed in generation based on fuel type, such as natural gas, hydro, coal, solar, and wind, in the WECC. The trends were also identified for generation, net load in the United States, and the WECC model.

3.3.1 Net Generation

The net generation of different types of generators can be downloaded from the EIA website at the following link (https://www.eia.gov/electricity/data/browser/). The results are summarized in Figure 3-3 and Figure 3-4. There is an obvious decrease in coal generation while the generations from natural gas, wind, and solar increase significantly. There is also a burst growth for wind generation starting in year 2001, while the burst growth for solar generation started in year 2011. From the perspective of oscillation analysis, the observations indicate that the U.S. power grid is losing inertia that comes with conventional

coal generation. Also, the system dynamic responses of the grid are more driven by the faster inverter-driven solar and wind generations.

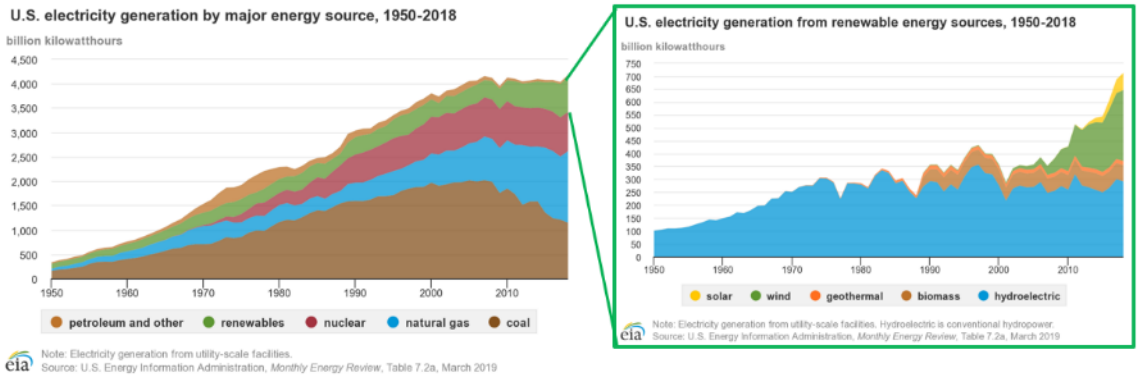

Figure 3-3. Constituent changes for different types of generations from year 1950 to year 2018 (figures are collected from the EIA).

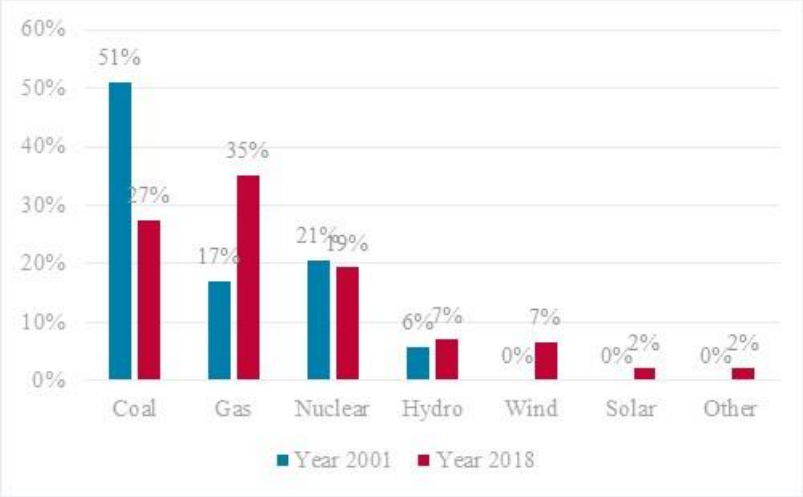

Figure 3-4. Constituent changes for different types of generations in year 2001 and year 2018 (data are collected from the EIA).

3.3.2 Renewable Generation by States

Renewable generation data are collected from the EIA with a time resolution of a month and geo-resolutions of the states. Solar and wind generation for different states in June 2019 are shown in Figure 3-5. California is significantly leading other states in solar generation, while Texas is leading other states in wind generation.

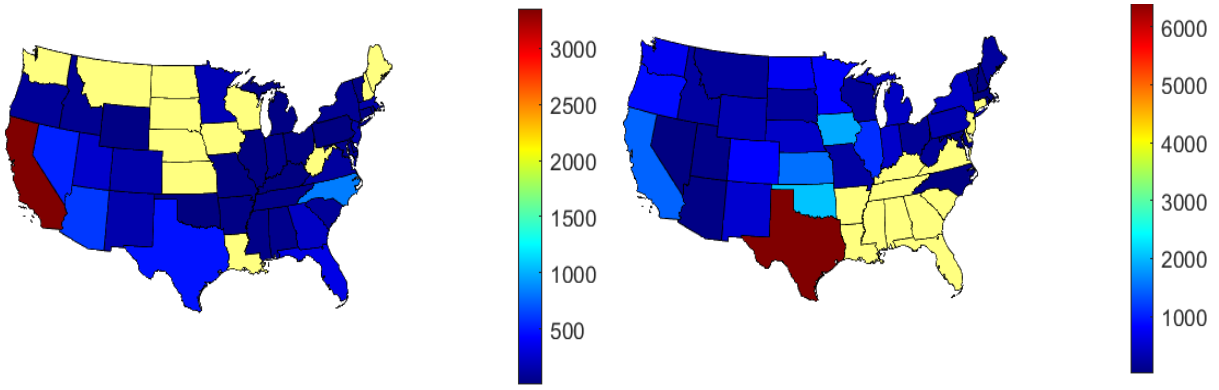

Figure 3-5. Solar (left) and wind (right) generations in different states in June 2019 (GWh).

3.3.3 Generations and Loads in WECC

The total load and generation from solar, wind, natural gas, coal, nuclear, and hydro from 06/30/2018 to 10/01/2019 (15 months) in the WECC system were downloaded from the EIA website (EIA, 2019). Trends observed in generation and load are summarized as follows.

The **total load** is plotted in Figure 3-6. In a yearly cycle, the load in the WECC peaks during the summertime. In a daily cycle, the peak hours are from around 12:00 to 22:00. The peak load was lower in year 2019 than that in 2018.

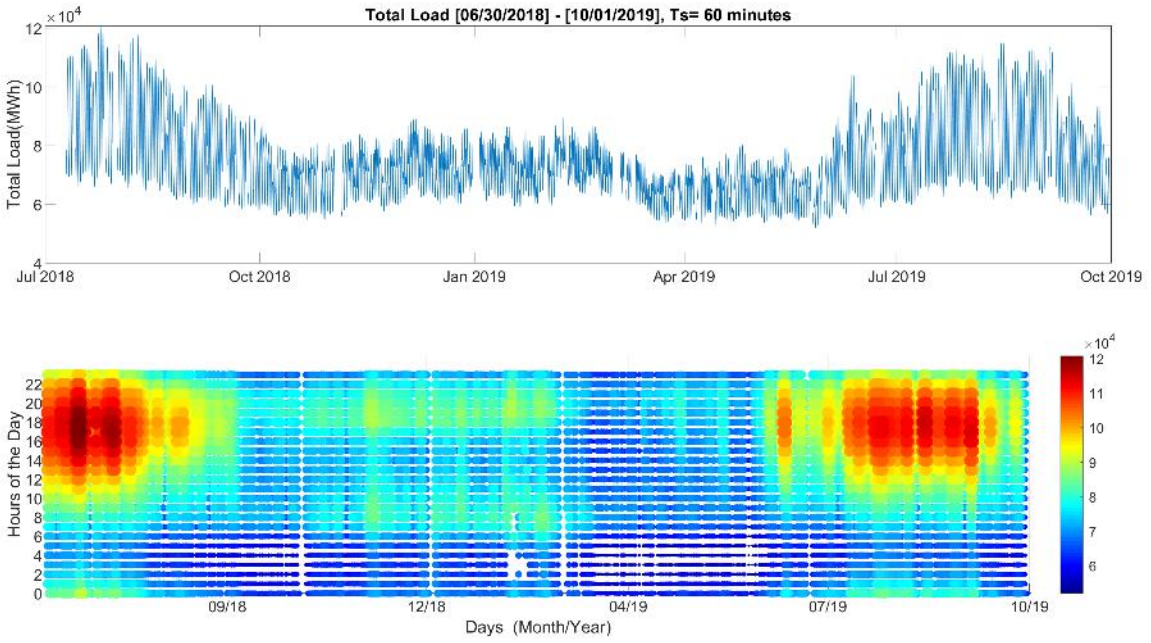

Figure 3-6. Total load time-series plot (top) and 3D scatter plot (bottom).

Total solar generation is plotted in Figure 3-7. In a yearly cycle, solar generation in the WECC peaks during the summertime. In a daily cycle, the peak hours are from around 9:00 to 16:00. The peak in year 2019 is higher than that in 2018.

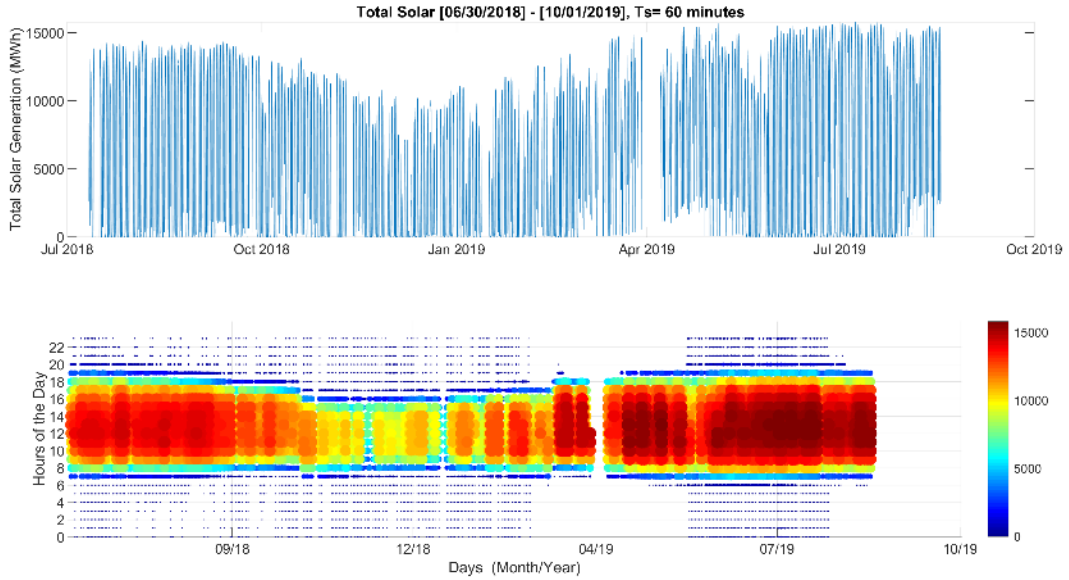

Figure 3-7. Total solar generation time-series plot and 3D scatter plot.

Total wind generation is plotted in Figure 3-8. In a yearly cycle, wind generation in the WECC peaks during the summertime. The peak in year 2019 is higher than that in 2018.

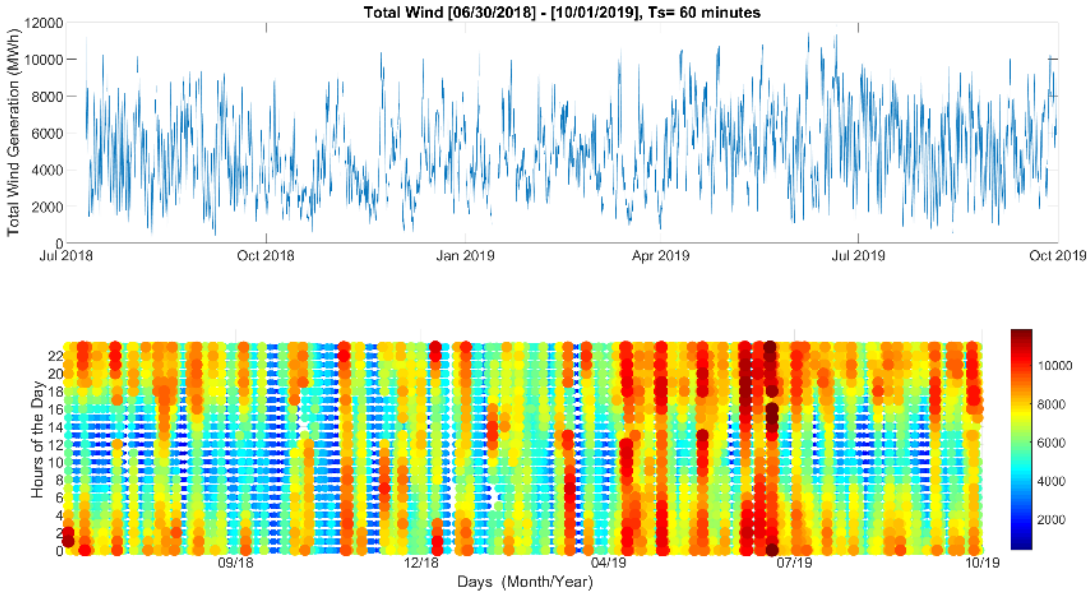

Figure 3-8. Total wind generation time-series plot and 3D scatter plot.

Total natural gas-based generation is plotted in Figure 3-9. Natural gas-based generation has a yearly peak during the summer between July and October. In its daily cycle during the summer, the peak values are between 14:00 and 22:00, which pick up the load when solar generation ramps down.

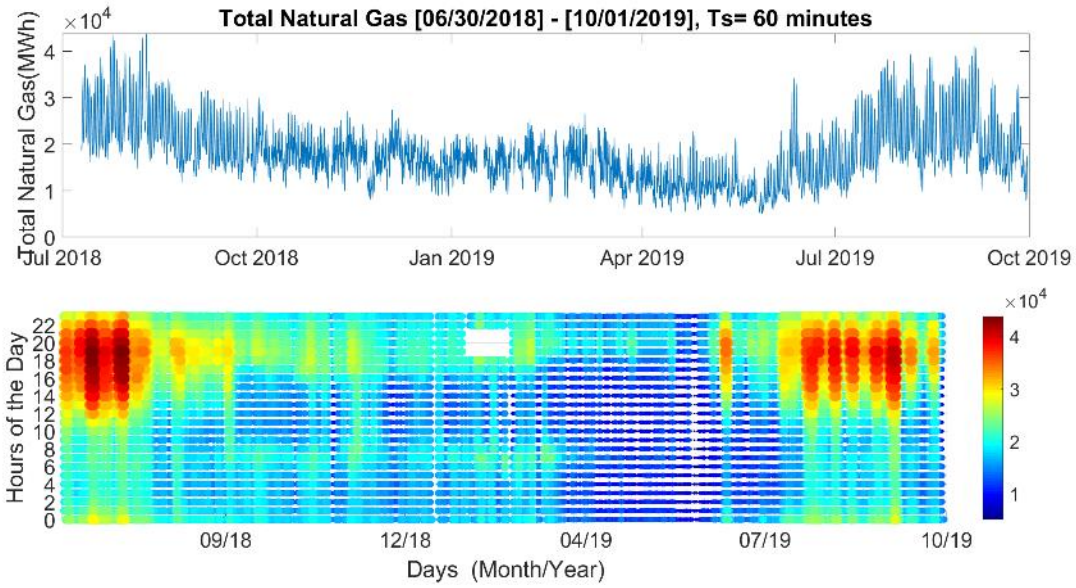

Figure 3-9. Total natural gas generation time-series plot and 3D scatter plot.

Total coal-based generation is plotted in Figure 3-10. Coal-based generation has a valley between April 2019 and July 2019. This is coincident with the peak of hydro generation in Figure 3.14. There is no obvious daily cycle in coal-based generation.

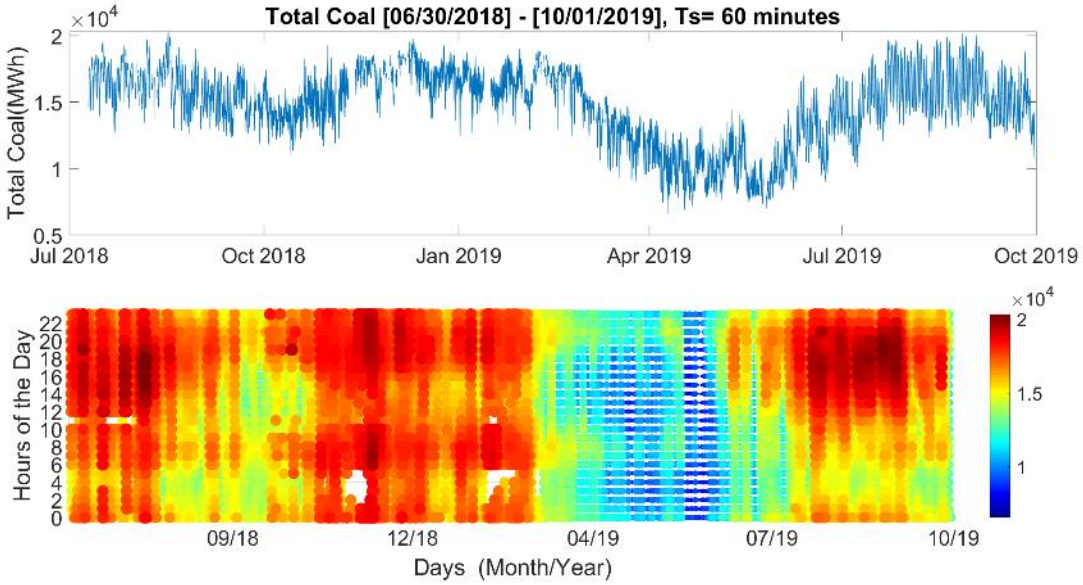

Figure 3-10. Total coal generation time-series plot and 3D scatter plot.

The total hydro generation is plotted in Figure 3-11. In its yearly cycle, there is a peak between April and July 2019. In its daily cycle, there are two peaks. The major peak is around between18:00 and 22:00. The secondary peak is between 6:00 and 8:00.

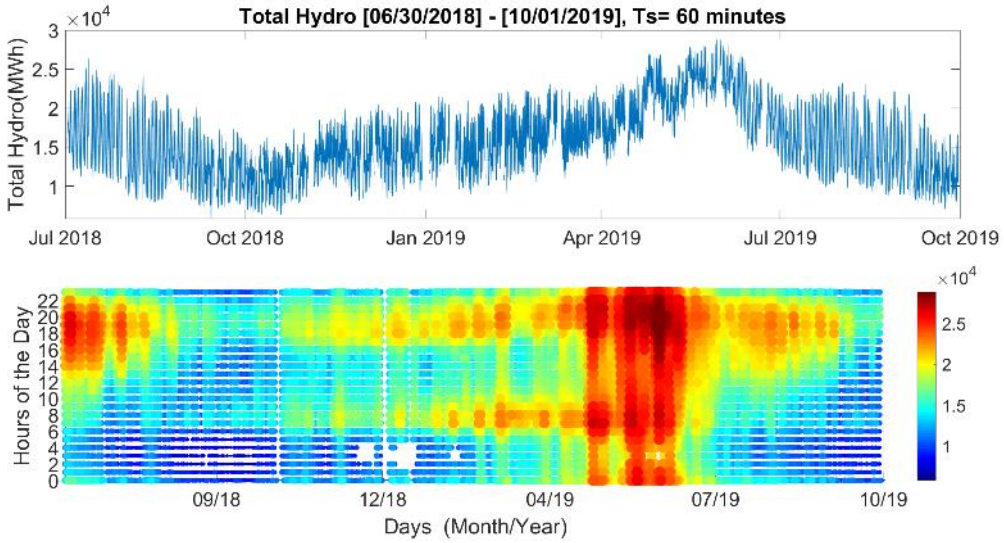

Figure 3-11. Total hydro generation time-series plot and 3D scatter plot.

3.3.4 Future Generation and Load Mix

As indicated in Figure 3-12, generation will continue growing during the next 30 years[1]. The major growth will come from solar generation.

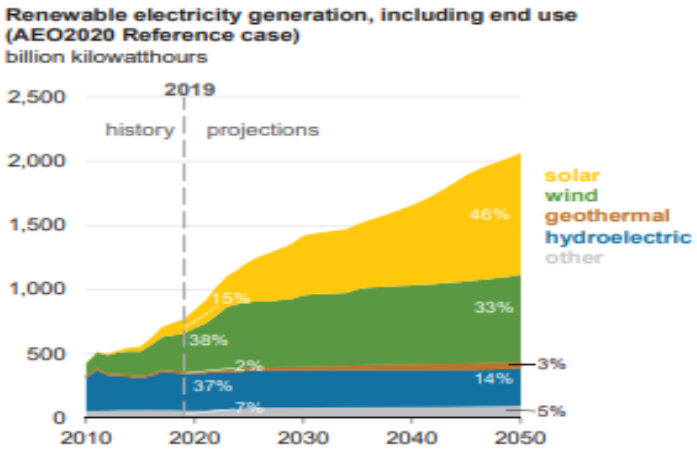

Figure 3-12. Projected change in the generation-mix over the next 30 years.

[1] https://www.eia.gov/outlooks/aeo/pdf/aeo2020.pdf

4.0 PMU Data-Based Wide-Area Oscillation Modes Assessment

PMU data of the WECC system are collected from Pacific Northwest National Laboratory's (PNNL's) Electric Infrastructure Operation Center (EIOC) through streaming data provided by the Bonneville Power Administration (BPA). The data covers the major 500 kV substations of BPA and is archived in EIOC using BPA's custom software in 1-minute files that span the period from January 1, 2017 to August 19, 2019.

The WECC has several well-studied system modes as shown in Table 4-1. Each of these modes have their own unique characteristics of frequency and mode shapes, also provided in Table 4-1. The DRs of these modes are determined by system topology and system stress. When Alberta is disconnected, North-South Mode A (NS-A) and North-South Mode B (NS-B) combine to form a single north-south mode near 0.32 Hz with the northern half oscillating against the southern half and the dividing line being near the COI.

Table 4-1. Well-known system modes in the Western Interconnection (WI) (WECC JSIS, 2013).

Mode Name	Frequency (Hz)	Mode Shape
NS-A	0.25	Northern half vs. southern half
NS-B	0.4	Alberta vs. British Columbia (B.C.) and Northern U.S. vs. Southern U.S.
East-West Mode A	0.45	Eastern portion of the system centralized in Colorado vs. rest of the system
British Columbia	0.6	B.C. vs. Northwest
Montana	0.8	Montana vs. Northwest

The two most dominant electromechanical modes in the WECC system are estimated from the collected PMU data to determine if there are significant trends in the oscillatory characteristics associated with the increased renewable penetration. These are the NS-A and NS-B; detailed descriptions can be found in (WECC JSIS, 2013). NS-A typically has a frequency near 0.25 Hz and is characterized by generators in the northern part of the system swinging against those in the south. NS-B has a typical frequency of 0.4 Hz. The typical shape of NS-B has generators in Alberta and the Southwestern United States swinging against those in B.C. and the Northwestern United States.

NS-A and NS-B were evaluated over 32 months spanning January 1, 2017 to August 19, 2019. The BPA provided estimates beginning December 1, 2018, at 15-minute intervals. PNNL's Archive Walker tool was used to generate mode estimates for the remaining 23 months by analyzing PMU data collected at the

EIOC. Archive Walker is an open-source tool developed by PNNL with funding from BPA and the U.S. Department of Energy (PNNL, 2019). It includes a mode meter capable of closely replicating the commercial analysis engine used by the BPA. The Yule-Walker algorithm (Trudnowski, Pierre, Zhou, Hauer, & Parashar, 2008) implemented in Archive Walker was configured with the same parameters as those used by BPA. Additionally, measurements from the same substations used by the BPA were analyzed within Archive Walker. Thus, the estimates generated by Archive Walker are very consistent with those provided by the BPA.

Figure 4-1 and Figure 4-2 give the time-series plot and 3D scatter plot for the estimated frequency and DR for NS-A mode in the WECC system from PMU data.

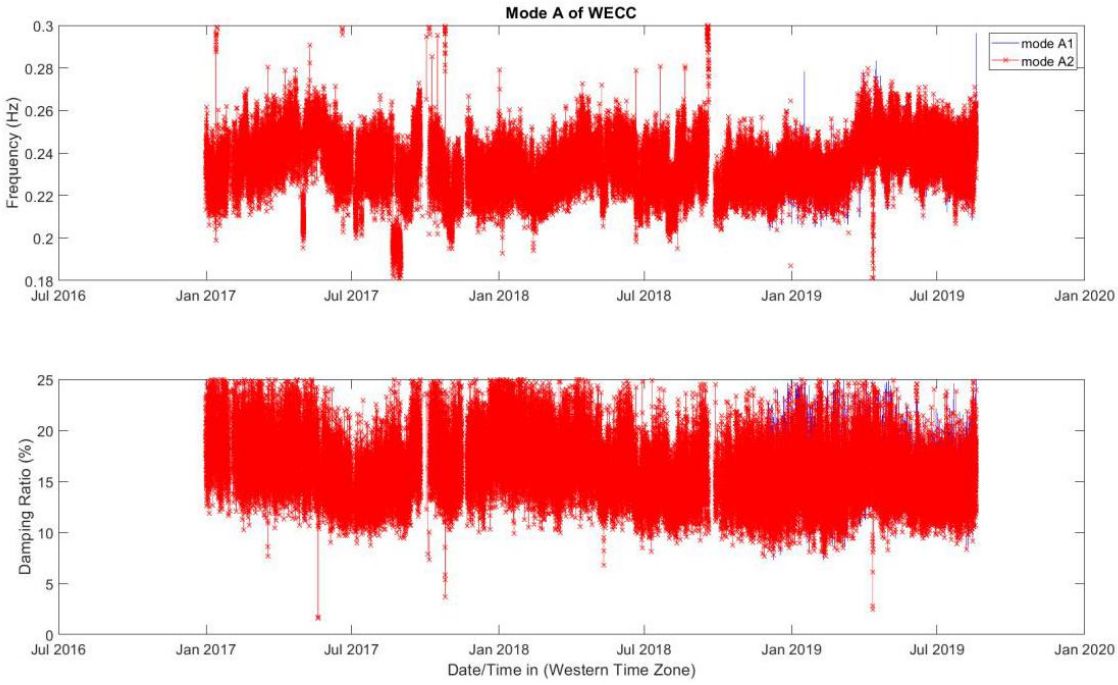

Figure 4-1. Time-series plot of wide-area NS-A mode (0.25 Hz).

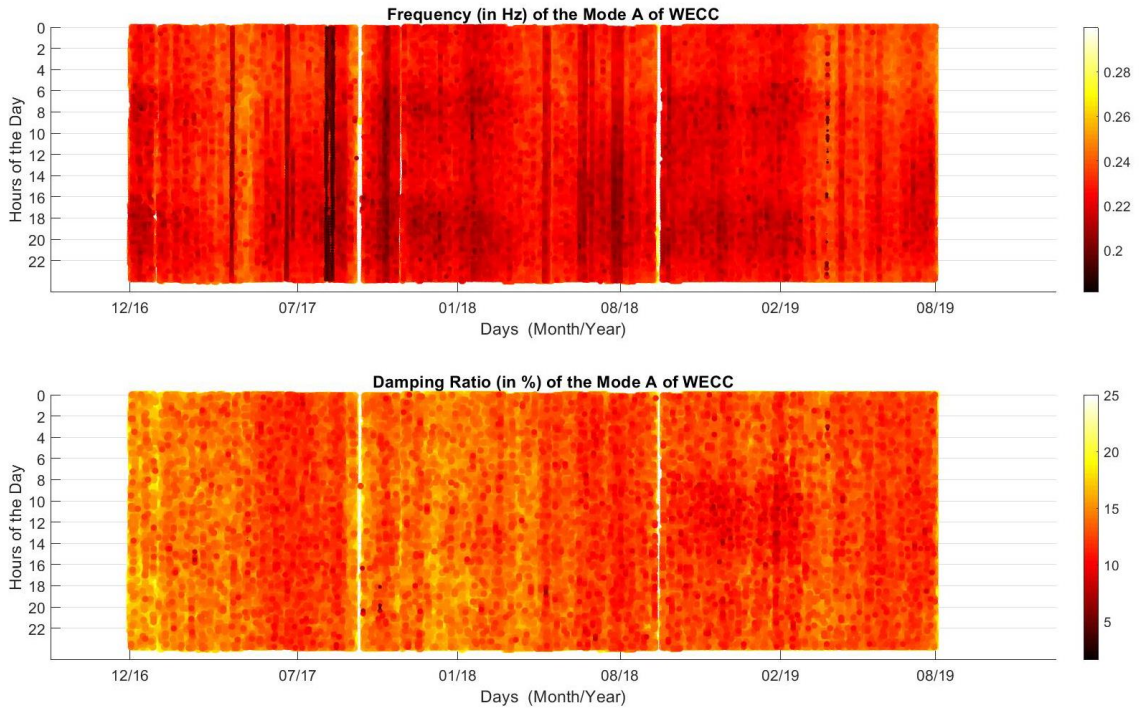

Figure 4-2. 3D scatter plot of wide-area NS-A mode (0.25 Hz).

Figure 4-3 and Figure 4-4 give the time-series plot and 3D scatter plot for the estimated frequency and DR for NS-B mode of the WECC from PMU data.

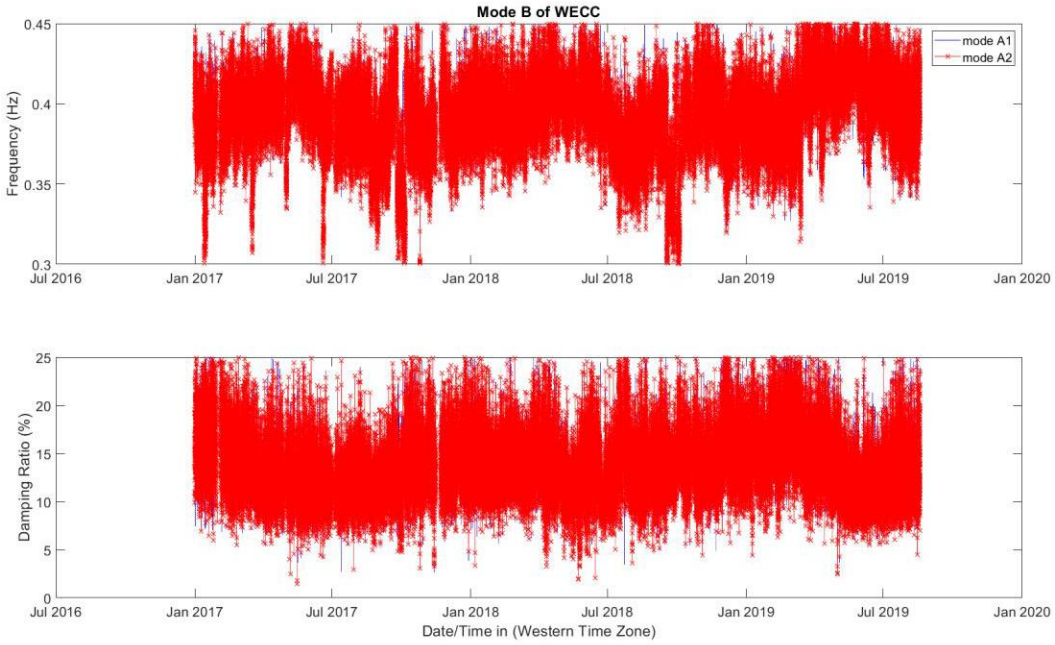

Figure 4-3. Time-series plot of wide-area NS-B mode (0.4 Hz).

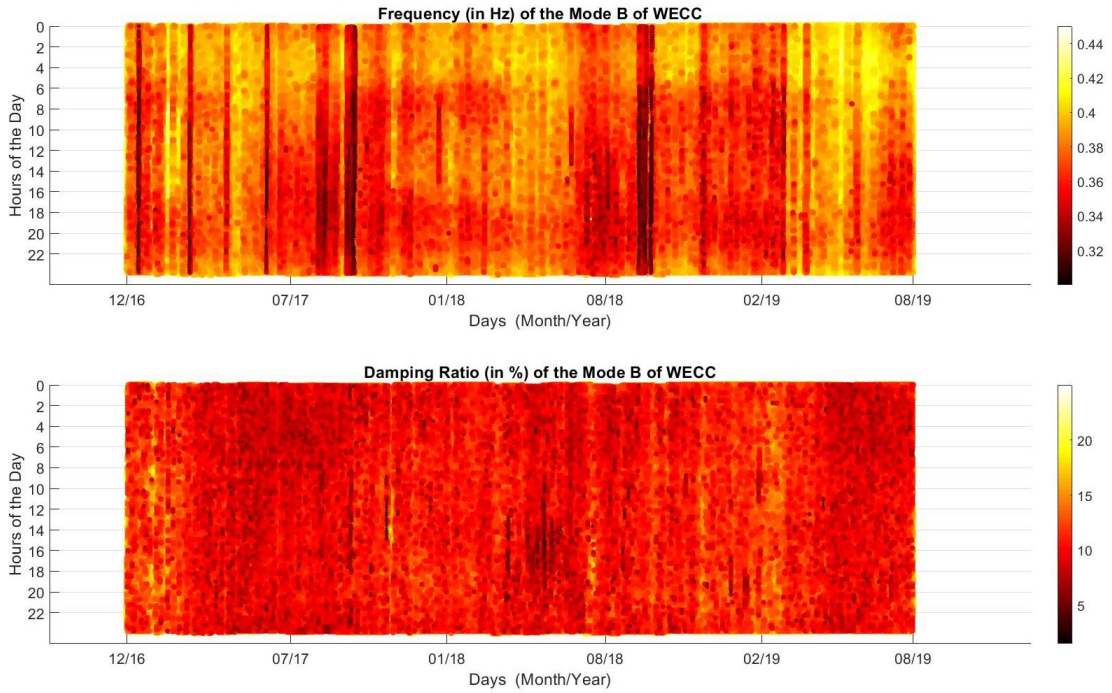

Figure 4-4. 3D scatter plot of wide-area NS-B mode (0.4 Hz).

In addition to generating mode estimates, Archive Walker was used to retrieve the COI and Pacific Direct Current Intertie (PDCI) power flows from the synchrophasor measurements. These power flows correspond to important interfaces in the WECC system.

Figure 4-5 shows the power flow of the PDCI from January 2015 to January 2019.

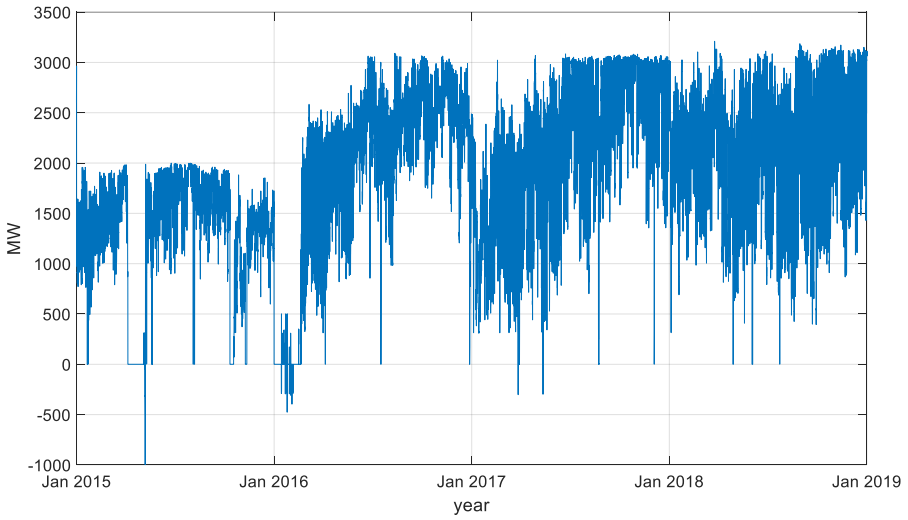

Figure 4-5. Historical PDCI power flow data (source: bpa.gov, available online at https://transmission.bpa.gov/Business/Operations/Paths/).

Figure 4-6 gives the power flows of the COI from January 2017 to December 2019. During the 2019 spring season, the direction of the COI power flow was negative (from south to north of the WECC system), which is seldom observed in previous years. The reason for the negative flow was due to the increasing penetration level of solar generation in the California areas.

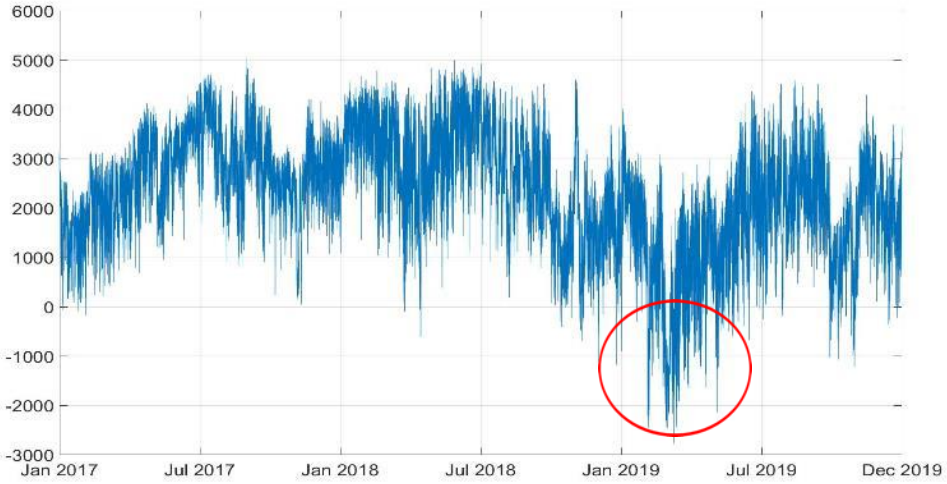

Figure 4-6. Historical COI flow data (source: bpa.gov, available online at https://transmission.bpa.gov/Business/Operations/Paths/).

5.0 Data-Based Correlation Analysis

Because of the complexity of the power grid and wide-area oscillation problems, many factors (such as tie-line flow, operational points, generation/load distributions, and load/generation mixes) influence the wide-area oscillation modes in a complex way (Huang, et al., 2010). The time-variant and complex natures of these factors determine that uncertainty levels in the correlation analysis are high. In addition, estimates of the modes from PMU data also contain uncertainty caused by the randomness of measurement and ambient noises (Anderson, Zhou, Pierre, & Wies, 2005). Often the estimation accuracy is high when actual mode damping is low, while the estimation accuracy is low when actual mode damping is high. Thus, the response variables (i.e., estimated modes) also have varying uncertainty. As such, uncertainty associated with correlation analysis in wide-area oscillations cannot be ignored. The correlation analysis should be performed under a statistical framework, which can quantify the uncertainty to describe how much confidence can be placed on the correlation analysis results. A detailed description of the algorithms used for the correlation analysis and the results that correlate mode estimates to the changing generation/load mix are provided next.

5.1 Correlation Algorithms

There are many correlation analysis methods under statistical frameworks (Cohen, Cohen, West, & Aiken, 2002). The least-square regression (LSR) method (Smith, 1967) is arguably the most widely-used because of its simplicity of implementation and lower computational complexity. Under the assumption of the Gaussian noise, LSR estimates the conditional mean of the response variables. The major drawbacks of applying LSR in the correlation analysis of wide-area oscillations include: (1) the Gaussian noise assumption of LSR is often not valid for unsymmetrical estimation errors in mode estimation; (2) LSR is not robust to outliers because the l_2 norm in its objective function can exacerbate the negative impact of an outlier; and (3) LSR only provides a point estimate (i.e., conditional mean), which is often not sufficient when uncertainty levels are high. As such, LSR is only used as a reference method in this study.

The quantile regression (QR) method (Koenker & Hallock, 2001) is chosen to perform the correlation analysis because of the following features in dealing with uncertainty: (1) QR makes no assumption on the probability distribution of the regression residuals, which provides the flexibility needed for correlating estimated oscillation modes; (2) QR is more robust to outliers than LSR because its objective function is of the l_1 norm instead of the l_2 order norm in LSR; and (3) QR provides the estimate of the conditional probability distribution function (PDF). Even though the computational complexity of QR is

higher than that of LSR, the computational time is not a major constraint for the offline application in this study. As such, QR is chosen as the focus of this study to perform the correlation analysis.

5.1.1 Regression Model of the Quantile Regression

The regression model of QR is shown in (5-1).

$$y_i = \boldsymbol{x_i'}\,\boldsymbol{\beta_\tau} + e_i \tag{5-1}$$

y_i is the scalar of the response variable (e.g., damping) at measurement instance i, $i = 1,\ 2,\ \cdots,\ N$.

$\boldsymbol{x_i} = \begin{bmatrix} 1 \\ x_{1,i} \\ x_{2,i} \\ \vdots \\ x_{n,i} \end{bmatrix}$ is the vector of predictor variables (e.g., solar generation, wind generation, load).

$\boldsymbol{\beta_\tau} = \begin{bmatrix} \beta_{0,\tau} \\ \beta_{1,\tau} \\ \beta_{2,\tau} \\ \vdots \\ \beta_{n,\tau} \end{bmatrix}$ is the vector of unknown parameters to be estimated.

τ is the quantile level ($0\% < \tau < 100\%$, assigned by users).

e_i is the noise, which is used to model the impacts of the unknown inputs on y_i.

For each τ, there is a corresponding set of $\boldsymbol{\beta_\tau}$. The $\boldsymbol{x_i'}\,\boldsymbol{\beta}_\tau$ gives the prediction of the response variable at the quantile (percentage) level of τ, i.e., $P\{Y \le \boldsymbol{x_i'}\,\boldsymbol{\beta}_\tau | \boldsymbol{x_i}\} = \tau$.

5.1.2 Objective Function of Quantile Regression

Given τ, the samples of y_i and $\boldsymbol{x_i}$, the regression coefficients $\boldsymbol{\beta_\tau}$ can be found by solving (5-2) and (5-3).

$$\widehat{\boldsymbol{\beta}}_{\boldsymbol{\tau}} = argmin\,\{J(\boldsymbol{\beta_\tau})\} \tag{5-2}$$

$$J(\boldsymbol{\beta_\tau}) = \tau \sum_{i:y_i > \boldsymbol{x_i'}\boldsymbol{\beta_\tau}}^{N} (y_i - \boldsymbol{x_i'}\boldsymbol{\beta_\tau}) + (1-\tau) \sum_{j:y_j < \boldsymbol{x_j'}\boldsymbol{\beta_\tau}}^{N} -\left(y_j - \boldsymbol{x_j'}\boldsymbol{\beta_\tau}\right) \tag{5-3}$$

For a special case with $\tau = 50\%$, the corresponding objective function is the least absolution value regression as shown in (5-4).

$$J(\boldsymbol{\beta}_{50\%}) = 0.5 \sum_{i=1}^{N} |y_i - \boldsymbol{x}_i' \boldsymbol{\beta}_{50\%}| \quad (5\text{-}4)$$

5.1.3 Application of Quantile Regression

QR can be used to estimate the conditional distribution by giving the quantile at different levels. The quantile at the level of τ is defined as $Q_Y(\tau) = F_Y^{-1}(\tau) = inf\{y: P(Y \leq y) \geq \tau\}$. Here, $F_Y(y)$ is the cumulative distribution function (CDF). As such, once τ is given, QR can give its corresponding y. The curve of $[\tau, y]$ determined by QR is the cumulative distribution of Y.

As an application example, Figure 5-1 gives the correlation analysis results between the tie-line flow and 0.64 Hz inter-area modes of the two-area four-machine model. In this example, the tie-line flow (denoted as *TieLine*) is used as the only independent variable. The impact of other independent variables (e.g., generation/load mixes and distributions) are treated as noise e_i as in (5-1). The distribution of the measured points indicates a non-linear relationship. Thus, the predictor variables x_i set up a second-order polynomial of *TieLine* as in (5-5). Note that the relationship between the independent variable *TieLine* and the dependent variable y_i is non-linear, whereas the relationship between coefficients β_i and the dependent variable y_i is still linear.

$$\boldsymbol{x_i} = \begin{bmatrix} 1 \\ TieLine_i \\ TieLine_i^2 \end{bmatrix} \quad (5\text{-}5)$$

The DR of the 0.64 Hz inter-area mode are considered as response (dependent) variable, (i.e., $y_i = DR_i$). To construct the conditional distribution of the $Yy = Q_Y(\tau)$ $\tau = \{5\%, 50\%, 95\%\}$. The resulting curves are shown in Figure 5-1, which also shows the correlation analysis results from LSR (marked out by "Linear Regression" in the legend). Note that $\tau = 50\%$ gives the conditional median. In addition, QR can also give other sampling points on the CDF of $DRy = Q_Y(\tau)$.

To illustrate the meaning of $y = Q_Y(\tau)$, assume that DR of 0.64 Hz mode follows the Gaussian distribution at *TieLine* = 200. The three values of *y* at $\tau = \{5\%, 50\%, 95\%\}$ are the sampling points at the CDF and the PDF of *Y* (or *DR*) as they are illustrated in Figure 5-2. If needed, more sampling points can be added by inserting quantile levels in τ. Therefore, QR can give a distribution of the estimated dependent variables (i.e., the mode *DR* in this study). As a result, LSR can answer how renewable penetration influences damping *on average*. QR can answer how the renewable penetration influences the damping *when damping is low, medium, and high*.

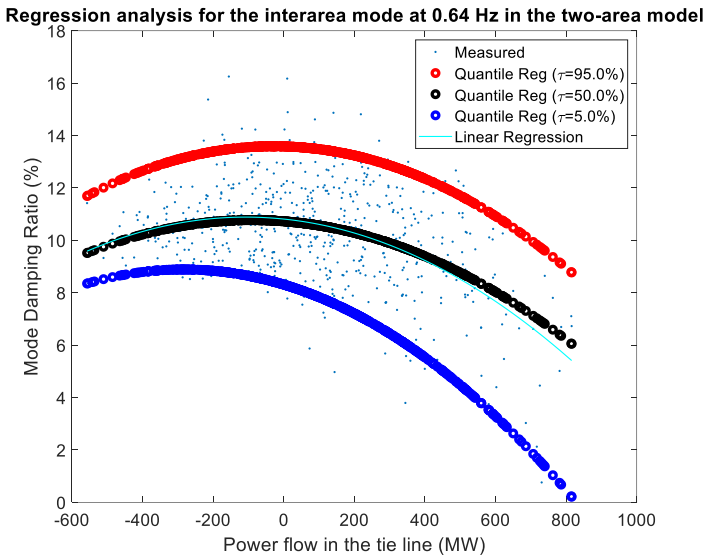

Figure 5-1. Correlation between tie-line flow and inter-area oscillation mode using QR analysis.

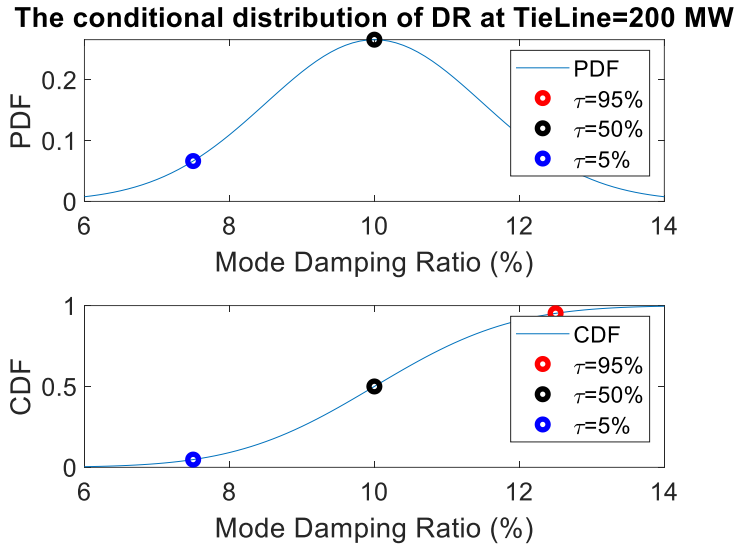

Figure 5-2. Analysis results from QR at *Tie-Line Flow* = 200 MW as a conditional distribution.

5.1.4 Quantify Uncertainty of Coefficients in Regression Models

Because of the limited number and quality of measurement data, the estimation results from QR (i.e., the CDF and the PDF of the conditional distribution) have uncertainty. To interpret the reliability of the estimated correlations, it is important to quantify the uncertainty of the QR analysis results. Confidence intervals of the coefficients $\widehat{\boldsymbol{\beta}}_{\boldsymbol{\tau}}$ from QR can be estimated using the bootstrapping method. The asymptotic covariance matrix of the QR estimator requires an estimate of the error density at the quantile of interest (Koenker, 1994). In this case, we have two choices: namely the residual bootstrap and the *xy*-pairs bootstrap. We chose the residual bootstrap, which involves resampling with replacement from the residual vector,

($\mathbf{Y}_{meas}$ - $\mathbf{Y}_{fit}$). It then adds these samples to the fitted vector $\boldsymbol{X\widehat{\beta}_{\tau}}$ and re-estimates the response variable with the assumption that the error process is independent and identically distributed. Repeating this procedure B times (*nBoot* in the Matlab code) yields a sample of B *p*-vectors whose covariance matrix constitutes a valid estimator of the original QR estimator (Koenker & Hallock, 2001). Then we use the so-called percentile method to compute the confidence intervals for the quantile of interest from the empirical distribution of the sample of bootstrapped $\boldsymbol{\widehat{\beta}_{\tau}}$s. Taking the 2.5 percentile and the 97.5 percentile of the bootstrap distribution provides us with a 95% confidence interval (Hahn, 1995). The algorithm to implement the bootstrapping is as follows:

1. Obtain the fitted vector, $\mathbf{Y}_{fit}$ using the traditional QR method.
2. Calculate the residuals ($\mathbf{Y}_{meas}$ - $\mathbf{Y}_{fit}$).
3. Bootstrap the residuals to obtain the $\boldsymbol{\widehat{\beta}_{\tau}}$'s.
4. Recalculate $\boldsymbol{X\widehat{\beta}_{\tau}}$ for each resampling.
5. Calculate the 95% confidence interval using the percentile method.

Figure 5-3 shows an example for quantifying the confidence intervals using the bootstrap method for QR. The black solid line in the figure shows results of QR using (5-2) and (5-3) with $\tau = 50\%$; in addition, the pink dashed line is for $\tau = 95\%$, and the red dotted line is for $\tau = 5\%$.

To quantify their uncertainties, the bootstrapping method discussed above is applied to quantify the uncertainty of the QR results. The confidence intervals are calculated and marked out as near-by thin lines around the QR results for the pink dashed line, the black solid line, and the red dotted line. In the subplot on the right, the confidence intervals are larger at the two ends than those in the center. This observation indicates the sparser data points at the two ends can result in large uncertainty in the QR results.

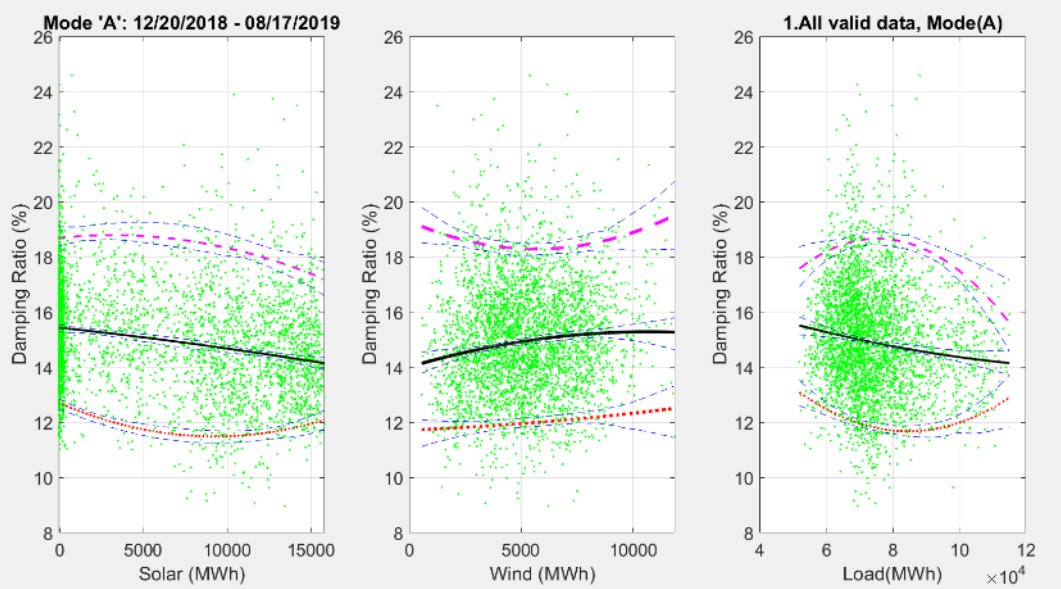

Figure 5-3. Example of uncertainty quantification in QR results using bootstrapping method. The pink dashed line and near-by thin lines show results for $\boldsymbol{\tau = 95\%}$ with 95% confidence level. The black solid line and near-by thin lines show results for $\boldsymbol{\tau = 50\%}$ with 95% confidence level. The red dotted line and near-by thin lines show results for $\boldsymbol{\tau = 5\%}$ with 95% confidence level.

5.2 Correlation Analysis Results

The objective of the correlation analysis study is to evaluate how different factors (e.g., generation mixes) impact the inter-area oscillation modes. Based on the model analysis, the following are identified as independent variables, which may impact the inter-area oscillation modes:

- Average real power of total solar generation (denoted as *S*)
- Average real power of total wind generation (denoted as *W*)
- Average real power of total load (denoted as *L*)
- Average real power of COI.

To focus on linear trend, the regression model in (5-1) is used to study the trend.

$$y_i = \beta_0 + S_i\,\beta_s + W_i\,\beta_w + L_i\,\beta_L + COI_i\,\beta_{COI} + e_i \qquad (5\text{-}6)$$

Here, coefficient β_0 is the intercept included to account for the average impact from other unknown factors. Coefficients $\beta_s,\ \beta_w,\ \beta_L, and\ \beta_{COI}$ are for the slope of solar generation, wind generation, load, and the COI flow. Symbol e_i is for unknown noise.

Because the study is carried out using field measurement data, the impacts of many factors are mixed in a complex way. To single out the impacts from a single factor, impacts from other factors should be reduced or even excluded. To achieve this objective, data are carefully selected so the studied factor varies over a wide range while other factors vary within a very limited range.

5.2.1 Correlation Analysis on NS-A (0.25 Hz Mode)

In this subsection, correlation analysis results are discussed for NS-A to identify trends with respect to the changes observed in solar generation, wind generation, system load, and COI flow.

5.2.1.1.1 Case I. Impact of Solar Renewable Generation

Case I focuses on the impact of solar generation on NS-A. To reduce the impacts from other factors, we selected data when the wind generation and load vary within a very small range.

Correlation Analysis on Mode DR

The responses of models corresponding to quantile levels (τ) of 95%, 50%, and 5% are summarized in Figure 5-4 for mode DR. The corresponding coefficients of QR and their confidence intervals are summarized in Table 5-1. Also, Table 5-1 summarizes the correlation analysis results from LSR. For the models with $\tau = 5\%, 50\%, 95\%$, the slope is negative within the confidence intervals, which indicates the DR decreases with the increase of solar generation. Similar to the QR model at $\tau = 5\%, 50\%, 95\%$, the LSR model gives a negative slope, which indicates the negative impact of increasing solar generation on the DR. In summary, the correlation analysis indicates that the increase of solar generation can be correlated to lower DR of the oscillation mode on average.

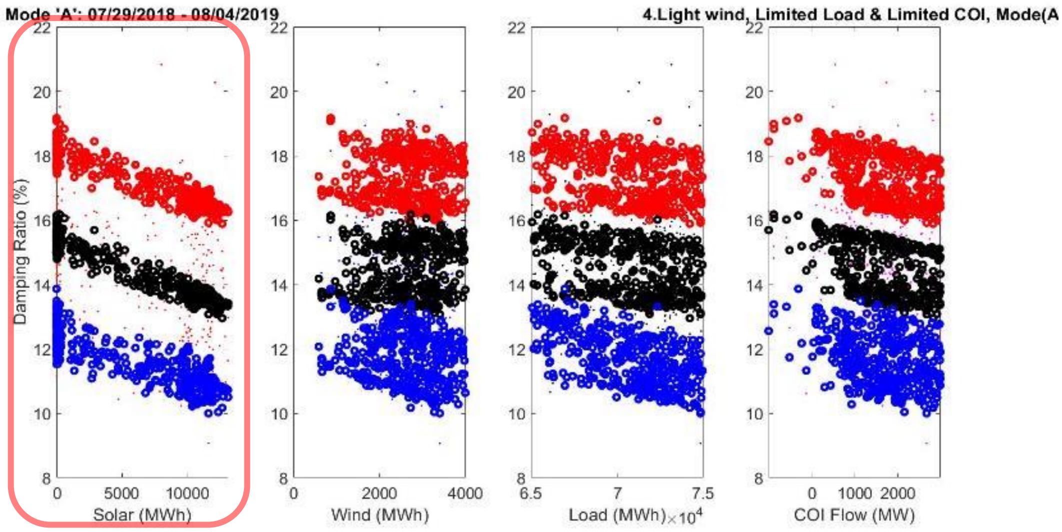

Figure 5-4. Responses of the QR model for mode DR of NS-A (red = 95%; black = 50%; blue = 5%).

Table 5-1. Identified QR/LSR models for mode DR and confidence intervals of their coefficients.

Quantile regression on damping ratio

95%) DampingRatio(%)=(Solar)*(-0.000135)+(Wind)*(-0.000203)+(load)*(-3.26e-05)+(COI)*(-0.000304)+(0.0214)*1000

Solar coefficients = -0.000135	**[-0.000175 -9.57e-05]**
Wind coefficients =-0.000203	**[-0.000428 2.23e-05]**
Load coefficients =-3.26e-05	**[-7.52e-05 1e-05]**
COI coefficients =-0.000304	**[-0.000554 -5.45e-05]**

50%) DampingRatio(%)=(Solar)*(-0.000147)+(Wind)*(-8.13e-05)+(load)*(-3.79e-05)+(COI)*(-0.000286)+(0.0187)*1000

Solar coefficients = -0.000147	**[-0.000167 -0.000127]**
Wind coefficients =-8.13e-05	**[-0.000195 3.21e-05]**
Load coefficients =-3.79e-05	**[-7.13e-05 -4.45e-06]**
COI coefficients =-0.000286	**[-0.000397 -0.000174]**

5%) DampingRatio(%)=(Solar)*(-0.000127)+(Wind)*(-0.00039)+(load)*(-0.000112)+(COI)*(-0.000173)+(0.0216)*1000

Solar coefficients = -0.000127	**[-0.00016 -9.39e-05]**
Wind coefficients =-0.00039	**[-0.000605 -0.000175]**
Load coefficients =-0.000112	**[-0.000162 -6.24e-05]**
COI coefficients =-0.000173	**[-0.000338 -8.04e-06]**

%%%%%%%%%%%%%%%%%%%%%%%%%%%%%%%%%%%% %%%%%%%%%%%%%%%%%%%%%%%%%%%%%%%%%%

Linear regression on damping ratio

DampingRatio(%)=(Solar)*(-0.000135)+(Wind)*(-0.000194)+(load)*(-3.99e-05)+(COI)*(-0.000274)+(0.019)*1000

Solar coefficients = -0.000135	**[-0.000173 -9.69e-05]**
Wind coefficients =-0.000194	**[-0.000425 3.75e-05]**
Load coefficients =-3.99e-05	**[-0.000109 2.91e-05]**
COI coefficients =-0.000274	**[-0.000492 -5.65e-05]**

Correlation Analysis on Mode Frequency

Model responses corresponding to quantile levels (τ) of 95%, 50%, and 5% are summarized in Figure 5-5 for mode frequency. The corresponding coefficients of QR and their confidence intervals are summarized in Table 5-2. The correlation analysis results from LSR are also summarized in Table 5-2. For models with $\tau = 5\%, 50\%, 95\%$, the slope is negative within the confidence intervals, which indicates the mode frequency decreases with the increase of solar generation. Similar to the QR model, LSR also gives a negative slope, which indicates a decreasing oscillation frequency in response to increasing solar generation. This observation is inconsistent with the intuition that solar PV generation will replace some conventional generation, thus resulting in lower inertia and higher oscillation frequency. In summary, the correlation analysis indicates the increase of solar generation can be correlated to the lower oscillation frequency of the inter-area mode.

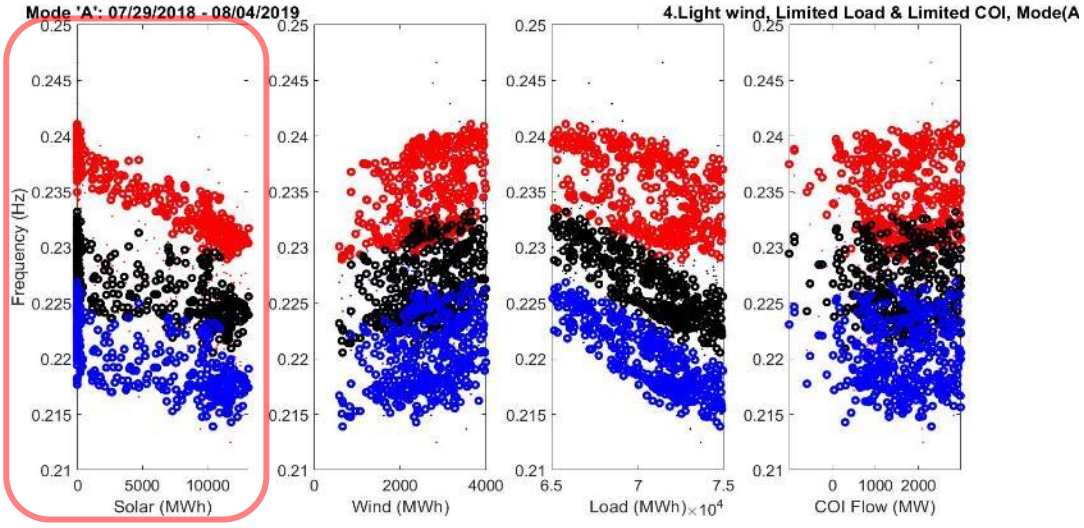

Figure 5-5. Responses of QR model for frequency of NS-A (red = 95%; black = 50%; blue = 5%).

Table 5-2. Identified QR/LSR models for mode frequency and confidence intervals of their coefficients.

Quantile regression on Frequency		
95%) Frequency(Hz)=(Solar)*(-5.68e-07)+(Wind)*(1.02e-06)+(load)*(-3.17e-07)+(COI)*(3.53e-07)+(0.000257)*1000		
Solar coefficients =-5.68e-07	**[-6.72e-07**	**-4.64e-07]**
Wind coefficients =1.02e-06	**[5.44e-07**	**1.49e-06]**
Load coefficients =-3.17e-07	**[-3.67e-07**	**-2.66e-07]**
COI coefficients =3.53e-07	**[1.01e-07**	**6.04e-07]**
50%) Frequency(Hz)=(Solar)*(-2.88e-07)+(Wind)*(8.99e-07)+(load)*(-7.52e-07)+(COI)*(4.49e-07)+(0.000278)*1000		
Solar coefficients =-2.88e-07	**[-3.35e-07**	**-2.41e-07]**
Wind coefficients =8.99e-07	**[6.13e-07**	**1.19e-06]**
Load coefficients =-7.52e-07	**[-7.94e-07**	**-7.1e-07]**

	COI coefficients =4.49e-07	[2.65e-07	6.34e-07]
5%) Frequency(Hz)=(Solar)*(-2.89e-07)+(Wind)*(8.88e-07)+(load)*(-7.86e-07)+(COI)*(4.43e-07)+(0.000274)*1000			
	Solar coefficients =-2.89e-07	[-3.56e-07	-2.23e-07]
	Wind coefficients =8.88e-07	[5.79e-07	1.2e-06]
	Load coefficients =-7.86e-07	[-8.33e-07	-7.39e-07]
	COI coefficients =4.43e-07	[2.27e-07	6.59e-07]
%%			
Linear regression on Frequency			
-) Frequency(Hz)=(Solar)*(-2.81e-07)+(Wind)*(9.14e-07)+(load)*(-7.5e-07)+(COI)*(4.44e-07)+(0.000278)*1000			
	Solar coefficients =-2.81e-07	[-3.77e-07	-1.84e-07]
	Wind coefficients =9.14e-07	[3.26e-07	1.5e-06]
	Load coefficients =-7.5e-07	[-9.25e-07	-5.74e-07]
	COI coefficients =4.44e-07	[-1.1e-07	9.98e-07]

5.2.1.1.2 Case II. Impact of Wind Renewable Generation

Correlation Analysis on Mode DR

Apply QR on the DR of the oscillation mode when there is light solar generation and a limited range of load and COI flow. Model responses corresponding to quantile levels (τ) of 95%, 50%, and 5% are summarized in Figure 5-6 for mode DR. The corresponding coefficients of QR and their confidence intervals are summarized in Table 5-3. The correlation analysis results from LSR are also summarized in Table 5-3. For models with $\tau = 5\%, 50\%, 95\%$, the slope is negative within the confidence intervals, which indicates that the DR decreases with the increase of wind generation. Similar to the QR model at $\tau = 5\%, 50\%, 95\%$, the LSR model gives a negative slope, which indicates the negative impact of increasing wind generation on the DR. In summary, the correlation analysis indicates that the increase of wind generation can be correlated to lower DR of the oscillation mode on average.

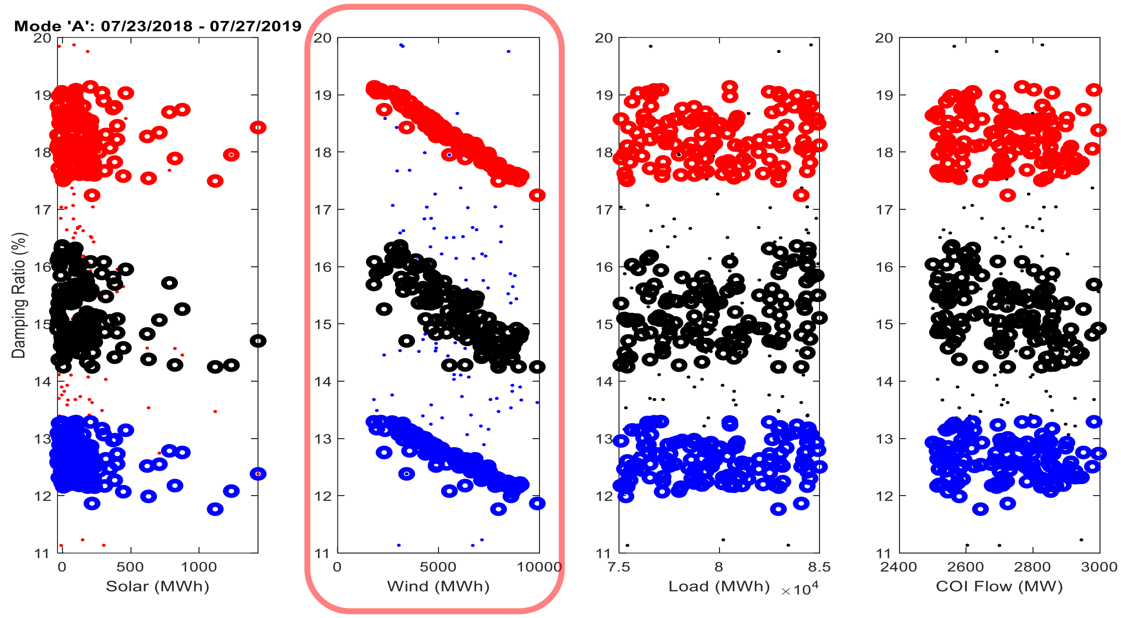

Figure 5-6. Responses of QR model for mode DR of NS-A (red = 95%; black = 50%; blue = 5%).

Table 5-3. Identified QR/LSR models for mode DR and confidence intervals of their coefficients.

Quantile regression on damping ratio		
95%) DampingRatio(%)=(Solar)*(0.000421)+(Wind)*(-0.000146)+(load)*(-7.95e-06)+(COI)*(-0.000236)+(0.0192)*1000		
	Solar coefficients =0.000421	**[-0.000401 0.00124]**
	Wind coefficients =-0.000235	**[-0.000384 -8.55e-05]**
	Load coefficients =-7.95e-06	**[-3.97e-05 2.38e-05]**
	COI coefficients =-0.000236	**[-0.000583 0.000112]**
50%) DampingRatio(%)=(Solar)*(0.000417)+(Wind)*(-0.000137)+(load)*(-2.95e-05)+(COI)*(-0.000355)+(0.0178)*1000		
	Solar coefficients =0.000417	**[2.32e-05 0.00081]**
	Wind coefficients =-0.000245	**[-0.000341 -0.000149]**
	Load coefficients =-2.95e-05	**[-6.02e-05 1.16e-06]**
	COI coefficients =-0.000355	**[-0.000496 -0.000213]**
5%) DampingRatio(%)=(Solar)*(-0.000331)+(Wind)*(-0.000141)+(load)*(-1.07e-05)+(COI)*(-0.000605)+(0.0142)*1000		
	Solar coefficients =-0.000331	**[-0.000861 0.000199]**
	Wind coefficients =-0.000174	**[-0.000326 -2.27e-05]**
	Load coefficients =-1.07e-05	**[-4.01e-05 1.87e-05]**
	COI coefficients =-0.000605	**[-0.0008 0.00041]**
%%		
Linear regression on damping ratio		
-) DampingRatio(%)=(Solar)*(0.000401)+(Wind)*(-0.000139)+(load)*(-1.04e-05)+(COI)*(-0.000317)+(0.0166)*1000		
	Solar coefficients =0.000401	**[-0.000265 0.00107]**
	Wind coefficients =-0.000151	**[-0.000318 -1.63e-05]**
	Load coefficients =-1.04e-05	**[-7.87e-05 5.79e-05]**
	COI coefficients = -0.000433	**[-0.00284 0.00197]**

Correlation Analysis on Mode Frequency

Model responses corresponding to quantile levels (τ) of 95%, 50%, and 5% are summarized in Figure 5-7 for mode frequency. The corresponding coefficients of QR and their confidence intervals are summarized in Table 5-4. The correlation analysis results from LSR are also summarized in Table 5-4. For the models with $\tau = 5\%, 50\%, 95\%$, the slope is positive within the confidence intervals, which indicates the mode frequency increases with the increase of wind generation. Similar to the QR model, the LSR model also gives a positive slope, which indicates the increasing oscillation frequency with increasing wind generation. This observation is consistent with the intuition that wind generation will replace some conventional generation resulting in lower inertia and thus higher oscillation frequency. In summary, the correlation analysis indicates that the increase of wind generation can be correlated to the higher oscillation frequency of the inter-area mode.

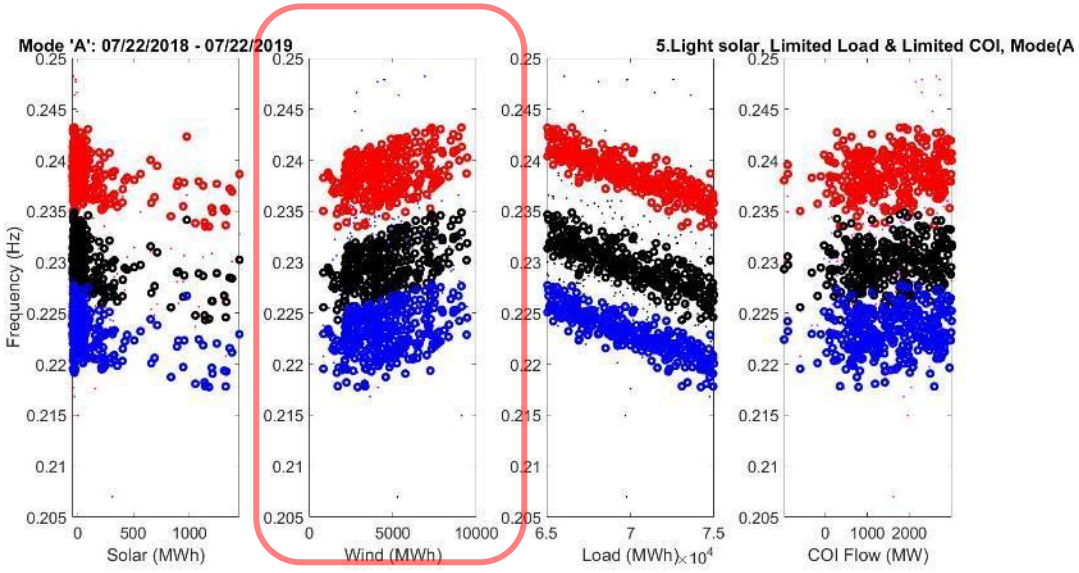

Figure 5-7. Responses of QR model for frequency of NS-A (red = 95%; black = 50%; blue = 5%).

Table 5-4. Identified QR/LSR models for mode frequency and confidence intervals of their coefficients.

Quantile regression on Frequency			
95%) Frequency(Hz)=(Solar)*(-1.51e-06)+(Wind)*(4.85e-07)+(load)*(-5.9e-07)+(COI)*(3.16e-07)+(0.000277)*1000			
	Solar coefficients =-1.51e-06	**[-3.25e-06**	**2.2e-07]**
	Wind coefficients =4.85e-07	**[1.59e-07**	**8.11e-07]**
	Load coefficients =-5.9e-07	**[-7.27e-07**	**-4.54e-07]**
	COI coefficients =3.16e-07	**[5e-08**	**5.82e-07]**
50%) Frequency(Hz)=(Solar)*(-1.36e-06)+(Wind)*(6.05e-07)+(load)*(-6.13e-07)+(COI)*(3.02e-07)+(0.00027)*1000			
	Solar coefficients =-1.36e-06	**[-2.16e-06**	**-5.53e-07]**
	Wind coefficients =6.05e-07	**[4.64e-07**	**7.46e-07]**
	Load coefficients =-6.13e-07	**[-6.5e-07**	**-5.76e-07]**
	COI coefficients =3.02e-07	**[1.03e-07**	**5.01e-07]**
5%) Frequency(Hz)=(Solar)*(-1.64e-06)+(Wind)*(4.56e-07)+(load)*(-6.2e-07)+(COI)*(3.08e-07)+(0.000264)*1000			

Solar coefficients =-1.64e-06	**[-2.58e-06**	**-6.94e-07]**
Wind coefficients =4.56e-07	**[2.36e-07**	**6.76e-07]**
Load coefficients =-6.2e-07	**[-7.03e-07**	**-5.37e-07]**
COI coefficients =3.08e-07	**[1.23e-07**	**4.93e-07]**
%%%		
Linear regression on Frequency		
-) Frequency(Hz)=(Solar)*(-1.55e-06)+(Wind)*(4.71e-07)+(load)*(-6.02e-07)+(COI)*(3.08e-07)+(0.00027)*1000		
Solar coefficients =-1.55e-06	**[-3.52e-06**	**4.17e-07]**
Wind coefficients =4.71e-07	**[1.71e-07**	**7.71e-07]**
Load coefficients =-6.02e-07	**[-8.04e-07**	**-4e-07]**
COI coefficients =3.08e-07	**[-3.57e-07**	**9.73e-07]**

5.2.1.1.3 Case III. Impact of Total Load

Correlation Analysis on Mode DR

The analysis applies QR on the DR of the oscillation mode when there is light wind and solar, and limited COI flow. Model responses corresponding to quantile levels (τ) of 95%, 50%, and 5% are summarized in Figure 5-8 for mode DR. The corresponding coefficients of QR and their confidence intervals are summarized in Table 5-5. The correlation analysis results from LSR are also summarized in Table 5-5. For models with $\tau = 50\%$, the slope is negative within the confidence intervals, which indicates that the DR decreases with the increase of load. For $\tau = 5\%, 95\%$, the slope is positive and negative, respectively, but the confidence intervals are ambiguous. Therefore, it is difficult to reach a conclusion whether they are positive, negative, or zero. A similar behavior is observed for the LSR model. In summary, the correlation analysis indicates that DR decreases with the increase in load when the DR is medium. And for high and low DR, it is difficult to comment on the correlation between load and the DR.

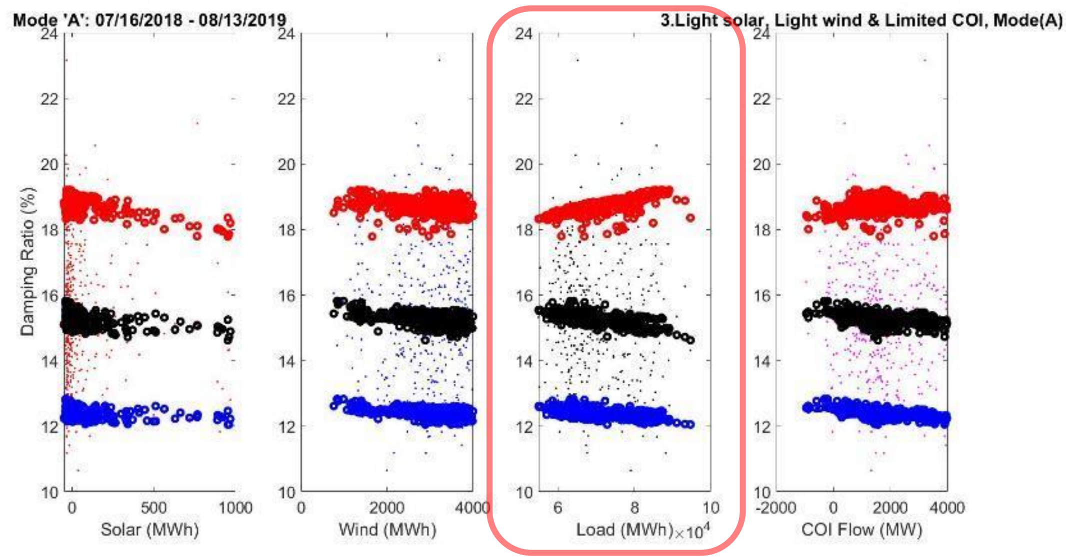

Figure 5-8. Responses of QR model for mode DR of NS-A (red = 95%; black = 50%; blue = 5%).

Table 5-5. Identified QR/LSR models for mode DR and confidence intervals of their coefficients.

Quantile regression on damping ratio

95%) DampingRatio(%)=(Solar)*(-0.000987)+(Wind)*(-6e-05)+(load)*(2.32e-05)+(COI)*(2.43e-05)+(0.0172)*1000

Solar coefficients =-0.000987	[-0.00227	0.000295]
Wind coefficients =-6e-05 [-0.000255	0.000135]	
Load coefficients =2.32e-05	[-3.53e-06	5e-05]
COI coefficients =2.43e-05 [-8.74e-05	0.000136]	

50%) DampingRatio(%)=(Solar)*(-0.000294)+(Wind)*(-0.000151)+(load)*(-1.6e-05)+(COI)*(-6.34e-05)+(0.0169)*1000

Solar coefficients =-0.000294	[-0.000824	0.000237]
Wind coefficients =-0.000151	[-0.000276	-2.7e-05]
Load coefficients =-1.6e-05 [-2.72e-05	-4.81e-06]	
COI coefficients =-6.34e-05	[-0.000158	3.12e-05]

5%) DampingRatio(%)=(Solar)*(-0.000124)+(Wind)*(-0.000112)+(load)*(-1.02e-05)+(COI)*(-6.54e-05)+(0.0136)*1000

Solar coefficients =-0.000124	[-0.000674	0.000426]
Wind coefficients =-0.000112	[-0.000298	7.46e-05]
Load coefficients =-1.02e-05	[-2.67e-05	6.21e-06]
COI coefficients =-6.54e-05	[-0.000182	5.15e-05]

%%

Linear regression on damping ratio

-) DampingRatio(%)=(Solar)*(-0.00012)+(Wind)*(-0.000105)+(load)*(-9.49e-06)+(COI)*(-6.16e-05)+(0.0164)*1000

Solar coefficients =-0.00012	[-0.00119	0.00095]
Wind coefficients =-0.000105	[-0.000356	0.000145]
Load coefficients =-9.49e-06	[-3.3e-05	1.41e-05]
COI coefficients =-6.16e-05	[-0.000233	0.00011]

Correlation Analysis on Mode Frequency

We apply QR on the frequency of the oscillation mode when there is light wind and solar, and limited COI flow. Model responses corresponding to quantile levels (τ) of 95%, 50%, and 5% are summarized in

Figure 5-9 for mode frequency. The corresponding coefficients of QR and their confidence intervals, as well as the correlation analysis results from LSR, are summarized in Table 5-6. For $\tau = 5\%, 50\%, 95\%$, the slope is negative within the confidence intervals, which agrees with the correlation analysis results from LSR. We can conclude that the mode frequency decreases with the increase in the load.

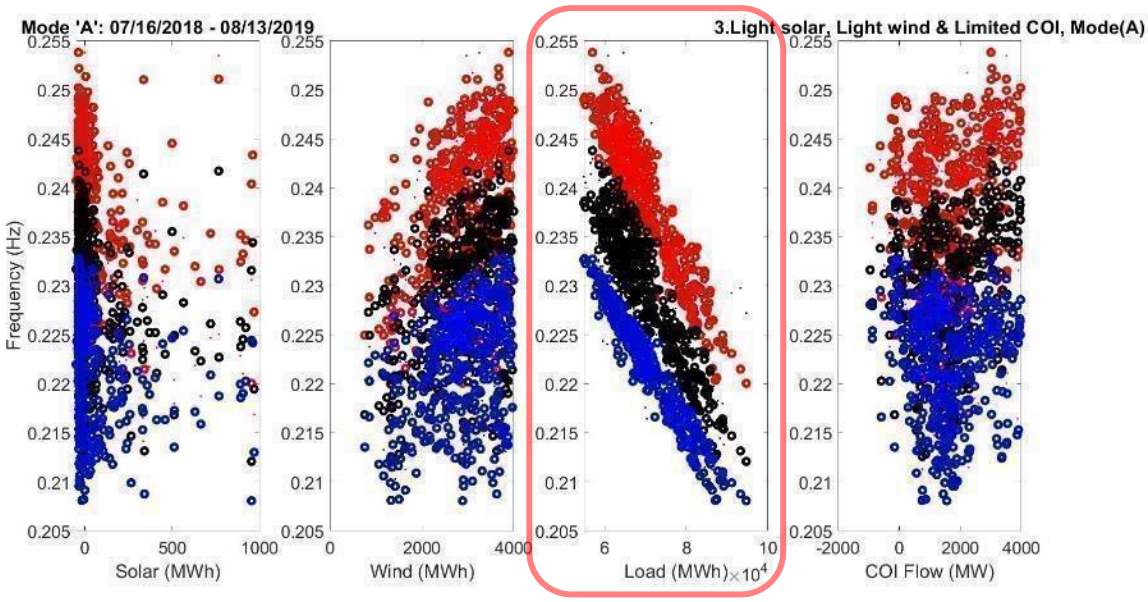

Figure 5-9. Responses of QR model for frequency of NS-A (red = 95%; black = 50%; blue = 5%).

Table 5-6. Identified QR/LSR models for mode frequency and confidence intervals of their coefficients.

Quantile regression on Frequency		
95%) Frequency(Hz)=(Solar)*(1.41e-06)+(Wind)*(1.87e-06)+(load)*(-8.11e-07)+(COI)*(1.94e-06)+(0.000287)*1000		
Solar coefficients =1.41e-06	**[1.36e-07**	**2.68e-06]**
Wind coefficients =1.87e-06	**[1.16e-06**	**2.58e-06]**
Load coefficients =-8.11e-07	**[-8.6e-07**	**-7.63e-07]**
COI coefficients =1.94e-06	**[1.36e-06**	**2.52e-06]**
50%) Frequency(Hz)=(Solar)*(1.37e-06)+(Wind)*(1.44e-06)+(load)*(-7.6e-07)+(COI)*(2.11e-06)+(0.000275)*1000		
Solar coefficients =1.37e-06	**[5.21e-07**	**2.21e-06]**
Wind coefficients =1.44e-06	**[1.08e-06**	**1.8e-06]**
Load coefficients =-7.6e-07	**[-7.93e-07**	**-7.27e-07]**
COI coefficients =2.11e-06	**[1.82e-06**	**2.39e-06]**
5%) Frequency(Hz)=(Solar)*(2.27e-06)+(Wind)*(1.6e-06)+(load)*(-6.6e-07)+(COI)*(3.34e-07)+(0.000263)*1000		
Solar coefficients =2.27e-06	**[1.29e-06**	**3.24e-06]**
Wind coefficients =1.6e-06	**[1.21e-06**	**1.99e-06]**
Load coefficients =-6.6e-07	**[-6.91e-07**	**-6.3e-07]**
COI coefficients =3.34e-07	**[2e-07**	**4.68e-07]**
%%%		
Linear regression on Frequency		
-) Frequency(Hz)=(Solar)*(1.51e-06)+(Wind)*(1.61e-06)+(load)*(-7.62e-07)+(COI)*(1.82e-06)+(0.000276)*1000		
Solar coefficients =1.51e-06	**[-1.58e-06**	**4.6e-06]**
Wind coefficients =1.61e-06	**[8.83e-07**	**2.33e-06]**
Load coefficients =-7.62e-07	**[-8.3e-07**	**-6.94e-07]**
COI coefficients =1.82e-06	**[1.32e-06**	**2.31e-06]**

5.2.1.1.4 Case IV: Impact of COI Flow

Correlation Analysis on Mode DR

QR is applied on the DR of the oscillation mode to study the correlation between DR and COI flow. Model responses corresponding to quantile levels (τ) of 95%, 50%, and 5% are summarized in Figure 5-10 for the mode DR. The corresponding coefficients of QR and their confidence intervals, as well as the correlation analysis results from LSR, are summarized in Table 5-7. For all τ values, the slope is negative and within the confidence intervals. LSR results indicate the same conclusion as the QR results. In summary, the correlation analysis indicates that the increase of COI flow can be correlated to lower DR of the oscillation mode on average.

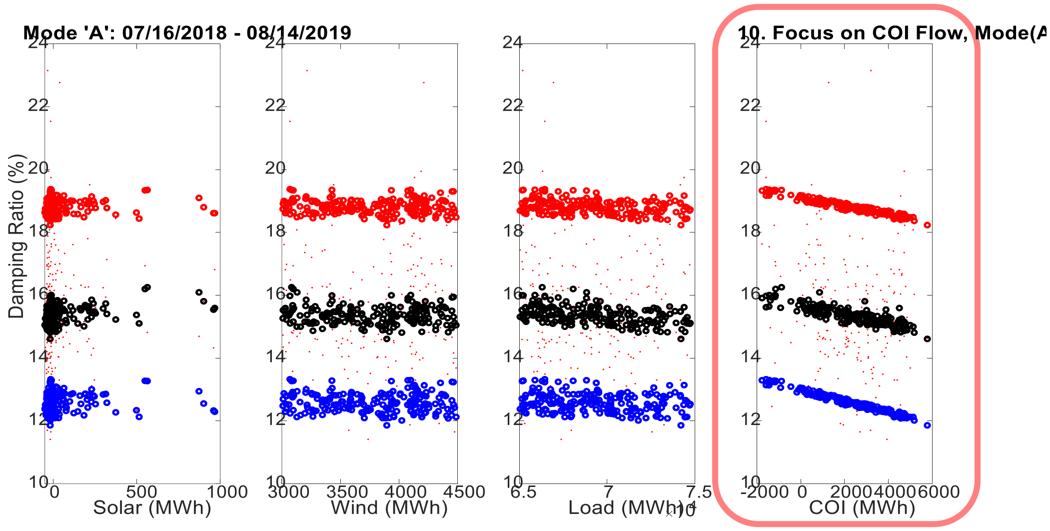

Figure 5-10. Responses of QR model for mode DR of NS-A (red = 95%; black = 50%; blue = 5%).

Table 5-7. Identified QR/LSR models for mode DR and confidence intervals of their coefficients.

Quantile regression on damping ratio			
95%) DampingRatio(%)=(Solar)*(0.000105)+(Wind)*(-1.38e-05)+(load)*(-2.41e-05)+(COI)*(-0.000129) +(0.0208)*1000			
	Solar coefficients =0.000105	**[-0.000972**	**0.00118]**
	Wind coefficients =-1.38e-05	**[-0.000157**	**0.000129]**
	Load coefficients =-2.41e-05	**[-0.000124**	**7.61e-05]**
	COI coefficients =-0.000129	**[-0.000325**	**6.76e-05]**
50%) DampingRatio(%)=(Solar)*(0.000633)+(Wind)*(1.74e-05)+(load)*(-4.79e-05)+(COI)*(-0.000137) +(0.0189)*1000			
	Solar coefficients =0.000633	**[-0.000278**	**0.00154]**
	Wind coefficients =1.74e-05	**[-0.000133**	**0.000168]**
	Load coefficients =-4.79e-05	**[-9.5e-05**	**-7.22e-07]**
	COI coefficients =-0.000137	**[-0.000227**	**-4.79e-05]**
5%) DampingRatio(%)=(Solar)*(0.00011)+(Wind)*(-1.41e-05)+(load)*(-2.15e-05)+(COI)*(-0.000175) +(0.0145)*1000			
	Solar coefficients =0.00011 [-0.000743	**0.000962]**	
	Wind coefficients =-1.41e-05	**[-0.000129**	**0.000101]**
	Load coefficients =-2.15e-05	**[-0.000103**	**6.02e-05]**
	COI coefficients =-0.000175	**[-0.00035**	**-5.79e-07]**
%%%			
Linear regression on damping ratio			
-) DampingRatio(%)=(Solar)*(0.000101)+(Wind)*(-1.39e-05)+(load)*(-2.63e-05)+(COI)*(-0.000132) +(0.0177)*1000			
	Solar coefficients =0.000101	**[-0.00156**	**0.00176]**
	Wind coefficients =-1.39e-05	**[-0.000662**	**0.000634]**
	Load coefficients =-2.63e-05	**[-0.000127**	**7.47e-05]**
	COI coefficients =-0.000132	**[-0.000292**	**2.88e-05]**

Correlation Analysis on Mode Frequency

QR is applied on the frequency of the oscillation mode to study the correlation with the COI flow. Model responses corresponding to quantile levels (τ) of 95%, 50%, and 5% are summarized in Figure 5-11 for the mode frequency. The corresponding coefficients of QR and their confidence intervals, as well as the

correlation analysis results from LSR, are summarized in Table 5-8. For $\tau = 5\%, 50\%, 95\%$, the slope is positive within the confidence intervals. Similar to the results from QR, LSR gives a positive slope, which indicates an increase in the mode frequency with the increase in the COI flow. We can conclude that the mode frequency increases with the increase in the COI flow.

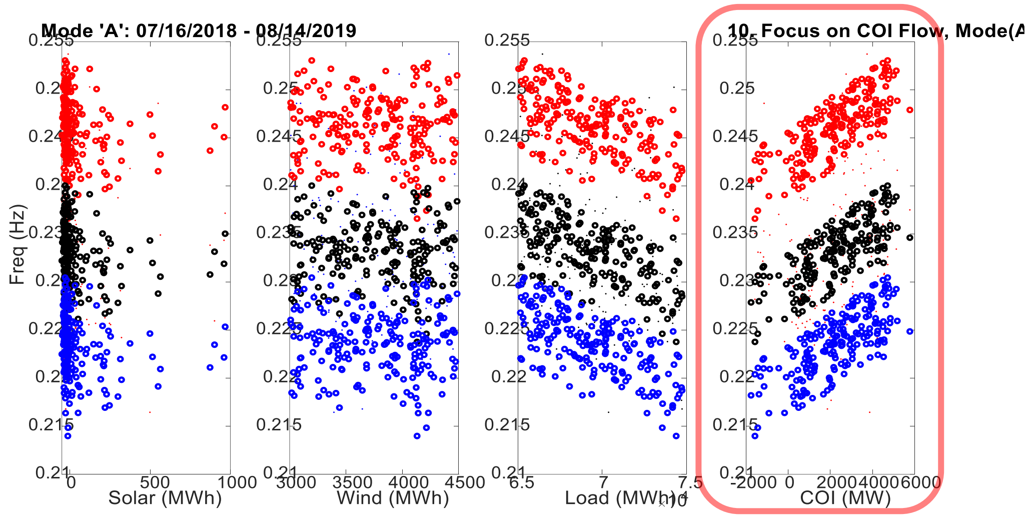

Figure 5-11. Responses of QR model for the mode frequency of NS-A (red = 95%; black = 50%; blue = 5%).

Table 5-8. Identified QR/LSR models for mode frequency and confidence intervals of their coefficients.

Quantile regression on frequency

95%) Frequency(Hz)=(Solar)*(-9.77e-07)+(Wind)*(1.33e-08)+(load)*(-7.64e-07)+(COI)*(1.52e-06) +(0.000296)*1000

Solar coefficients =-9.77e-07 [-1.25e-06 -7.02e-07]

Wind coefficients =1.33e-08 [9.42e-09 1.73e-08]

Load coefficients =-7.64e-07 [-9.14e-07 -6.15e-07]

COI coefficients =1.52e-06 [1.03e-06 2.01e-06]

50%) Frequency(Hz)=(Solar)*(-1.02e-06)+(Wind)*(1.3e-08)+(load)*(-7.87e-07)+(COI)*(1.45e-06) +(0.000285)*1000

Solar coefficients =-1.02e-06 [-2.16e-06 1.26e-07]

Wind coefficients =1.3e-08 [6.81e-09 1.92e-08]

Load coefficients =-7.87e-07 [-8.92e-07 -6.81e-07]

COI coefficients =1.45e-06 [1.13e-06 1.78e-06]

5%) Frequency(Hz)=(Solar)*(-1.03e-06)+(Wind)*(1.3e-08)+(load)*(-8.09e-07)+(COI)*(1.46e-06) +(0.000276)*1000

Solar coefficients =-1.03e-06 [-1.77e-06 -2.86e-07]

Wind coefficients =1.3e-08 [4.57e-09 2.13e-08]

Load coefficients =-8.09e-07 [-8.81e-07 -7.36e-07]

COI coefficients =1.46e-06 [1.03e-06 1.88e-06]

%%%

Linear regression on frequency

Linear) frequency (Hz)=(Solar)*(-9.89e-07)+(Wind)*(1.3e-08)+(load)*(-7.82e-07)+(COI)*(1.48e-06) +(0.000285)*1000

Solar coefficients =-9.89e-07 [-7.07e-06 5.09e-06]

Wind coefficients =1.3e-08 [-2.36e-06 2.39e-06]

Load coefficients =-7.82e-07 [-1.15e-06 -4.12e-07]

COI coefficients =1.48e-06 [8.88e-07 2.06e-06]

5.2.2 Correlation Analysis on NS-B (0.40 Hz Mode)

In this subsection, correlation analysis results are discussed for NS-B to identify trends with respect to the changes observed in solar generation, wind generation, system load, and COI flow.

5.2.2.1.1 Case I. Impact of Solar Generation

Correlation Analysis on Mode DR

QR is applied on the DR of the oscillation mode to study the correlation between DR and solar generation. Model responses corresponding to quantile levels (τ) of 95%, 50%, and 5% are summarized in Figure 5-12 for mode DR. The corresponding coefficients of QR and their confidence intervals, as well as the correlation analysis results from LSR, are summarized in Table 5-9. For $\tau = 95\%$ & 50%, the slope is negative within the confidence intervals, which indicates the DR decreases with the increase in solar generation. For $\tau = 5\%$, the slope is negative but not within the confidence intervals. Hence, for low DR, it is difficult to comment on the correlation between the DR and solar generation.

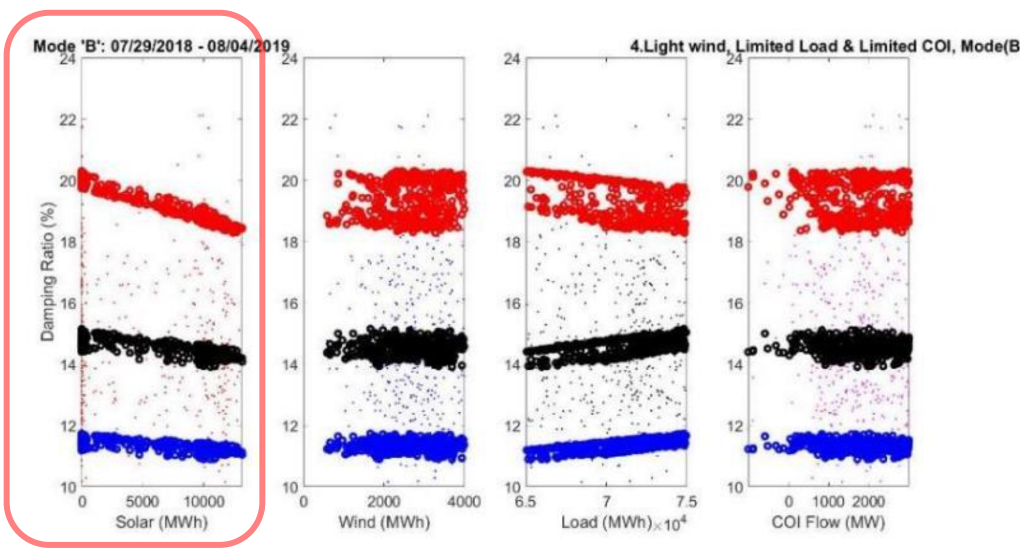

Figure 5-12. Responses of QR model for mode DR of NS-B (red = 95%; black = 50%; blue = 5%).

Table 5-9. Identified QR/LSR models for mode DR and confidence intervals of their coefficients.

%%%%%%%%%%%%%%%%%%%%%%%%%%%%%%

Quantile regression on damping ratio

95%) DampingRatio(%)=(Solar)*(-0.000118)+(Wind)*(-2.25e-05)+(load)*(-5.67e-05)+(COI)*(1.42e-05)+(0.024)*1000

Solar coefficients =-0.000118 [-0.000181 -5.38e-05]

Wind coefficients =-2.25e-05 [-0.000257 0.000212]

Load coefficients =-5.67e-05	**[-0.000168 5.49e-05]**
COI coefficients =1.42e-05	**[-0.000181 0.000209]**

50%) DampingRatio(%)=(Solar)*(-5e-05)+(Wind)*(-3.32e-05)+(load)*(7.3e-05)+(COI)*(-1.11e-06)+(0.00974)*1000

Solar coefficients =-5e-05	**[-7.64e-05 -2.35e-05]**
Wind coefficients =-3.32e-05	**[-0.000193 0.000127]**
Load coefficients =7.3e-05	**[2.42e-05 0.000122]**
COI coefficients =-1.11e-06	**[-6.57e-06 4.36e-06]**

5%) DampingRatio(%)=(Solar)*(-2.96e-05)+(Wind)*(-1.94e-05)+(load)*(5.57e-05)+(COI)*(-1.12e-05)+(0.00762)*1000

Solar coefficients =-2.96e-05	**[-6.73e-05 8.19e-06]**
Wind coefficients =-1.94e-05	**[-0.000136 9.71e-05]**
Load coefficients =5.57e-05	**[-6.38e-06 0.000118]**
COI coefficients =-1.12e-05	**[-0.000109 8.63e-05]**

%%

Linear regression on damping ratio

-) DampingRatio(%)=(Solar)*(-3.7e-05)+(Wind)*(-2.23e-05)+(load)*(3.53e-05)+(COI)*(-1.68e-05)+(0.0126)*1000

Solar coefficients =-3.7e-05	**[-8.79e-05 1.38e-05]**
Wind coefficients =-2.23e-05	**[-0.000333 0.000288]**
Load coefficients =3.53e-05	**[-5.68e-05 0.000127]**
COI coefficients =-1.68e-05	**[-0.000307 0.000273]**

Correlation Analysis on Mode Frequency

QR is applied on the frequency of oscillation mode to study the correlation with solar generation. Model responses corresponding to quantile levels (τ) of 95%, 50%, and 5% are summarized in Figure 5-13 for the mode frequency. The corresponding coefficients of QR and their confidence intervals, as well as the correlation analysis results from LSR, are summarized in Table 5-10. For $\tau = 5\%, 50\%, 95\%$, we can see the slope is negative within the confidence intervals, that is, the Solar-coefficients are negative with consistent ranging of negative values for the targeted confidence intervals. Similarly, LSR gives a negative slope, which indicates the mode frequency decreases with the increase in solar generation.

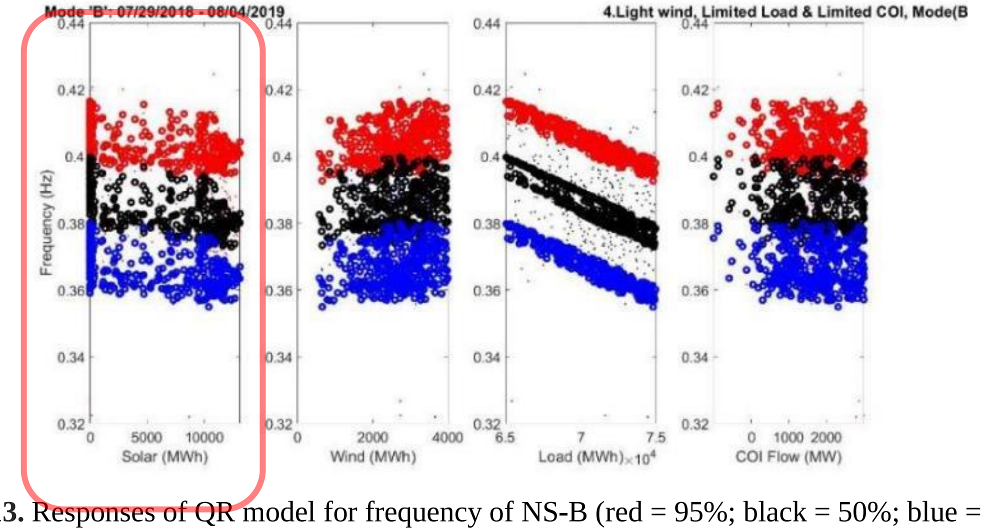

Figure 5-13. Responses of QR model for frequency of NS-B (red = 95%; black = 50%; blue = 5%).

Table 5-10. Identified QR/LSR models for mode frequency and confidence intervals of their coefficients.

Quantile regression on Frequency

95%) Frequency(Hz)=(Solar)*(-2.87e-07)+(Wind)*(1.12e-06)+(load)*(-1.86e-06)+(COI)*(-1.32e-07)+(0.000534)*1000

Solar coefficients =-2.87e-07	**[-4.58e-07**	**-1.16e-07]**
Wind coefficients =1.12e-06	**[2.1e-07**	**2.04e-06]**
Load coefficients =-1.86e-06	**[-1.94e-06**	**-1.79e-06]**
COI coefficients =-1.32e-07	**[-2.37e-07**	**-2.67e-08]**

50%) Frequency(Hz)=(Solar)*(-5.19e-07)+(Wind)*(2.46e-07)+(load)*(-2.08e-06)+(COI)*(-9.41e-08)+(0.000535)*1000

Solar coefficients =-5.19e-07	**[-6.64e-07**	**-3.75e-07]**
Wind coefficients =2.46e-07	**[-4.42e-08**	**5.36e-07]**
Load coefficients =-2.08e-06	**[-2.26e-06**	**-1.9e-06]**
COI coefficients =-9.41e-08	**[-1.86e-07**	**-2.14e-09]**

5%) Frequency(Hz)=(Solar)*(-2.98e-07)+(Wind)*(1.06e-06)+(load)*(-1.98e-06)+(COI)*(-1.34e-07)+(0.000506)*1000

Solar coefficients =-2.98e-07	**[-5.05e-07**	**-9.19e-08]**
Wind coefficients =1.06e-06	**[9.07e-08**	**2.02e-06]**
Load coefficients =-1.98e-06	**[-2.14e-06**	**-1.82e-06]**
COI coefficients =-1.34e-07	**[-3.23e-07**	**5.52e-08]**

%%%

Linear regression on Frequency

-) Frequency(Hz)=(Solar)*(-2.9e-07)+(Wind)*(1.09e-06)+(load)*(-1.91e-06)+(COI)*(-1.31e-07)+(0.000519)*1000

Solar coefficients =-2.9e-07	**[-5.61e-07**	**-1.82e-08]**
Wind coefficients =1.09e-06	**[-5.62e-07**	**2.75e-06]**
Load coefficients =-1.91e-06	**[-2.4e-06**	**-1.42e-06]**
COI coefficients =-1.31e-07	**[-1.68e-06**	**1.42e-06]**

5.2.2.1.2 Case II. Impact of Wind Generation

Correlation Analysis on Mode DR

QR is applied on the DR of the oscillation mode to study the correlation with wind generation. Model responses corresponding to quantile levels (τ) of 95%, 50%, and 5% are summarized in Figure 5-14 for mode DR. The corresponding coefficients of QR and their confidence intervals, as well as the correlation analysis results from LSR, are summarized in Table 5-11. For $\tau = 5\%, 50\%, 95\%$, the slope is negative but not within the confidence intervals. LSR results are similar to the QR results; hence, it is difficult to draw any conclusion on the correlation between DR of the 0.4 Hz mode and wind generation.

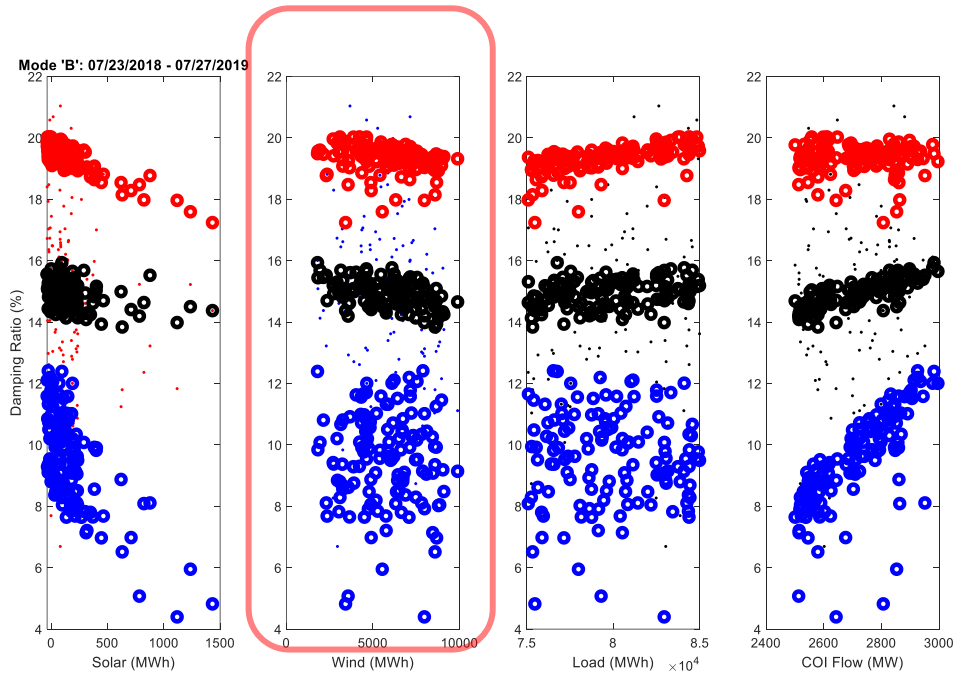

Figure 5-14. Responses of QR model for mode DR of NS- B (red = 95%; black = 50%; blue = 5%).

Table 5-11. Identified QR/LSR models for mode DR and confidence intervals of their coefficients.

Quantile regression on damping ratio		
95%) DampingRatio(%)=(Solar)*(-0.00153)+(Wind)*(-5.85e-05)+(load)*(6.94e-05)+ (COI)* (5.14e-05) +(0.0252)*1000		
Solar coefficients =-0.00153	**[-0.0032**	**0.00013]**
Wind coefficients =-5.85e-05	**[-0.000218**	**0.000101]**
Load coefficients =6.94e-05	**[-3.48e-05**	**0.000174]**
COI coefficients =5.14e-05	**[-0.000367**	**0.00047]**
50%) (Solar)*(-0.000684)+(Wind)*(-9.81e-05)+(load)*(3.4e-05)+ (COI)* (0.00252)+(0.0082)*1000		
Solar coefficients =-0.000684	**[-0.00164**	**0.00027]**
Wind coefficients =-9.81e-05	**[-0.000239**	**4.24e-05]**
Load coefficients =3.4e-05	**[-3.02e-05**	**9.82e-05]**
COI coefficients =0.00252	**[0.000475**	**0.00456]**
5%) DampingRatio(%)=Solar)*(-0.00458)+(Wind)*(-9.85e-06)+(load)*(-5.64e-05)+ (COI)* (0.00852)+(0.00529)*1000		
Solar coefficients =-0.00458	**[-0.00632**	**-0.00284]**
Wind coefficients =-9.85e-06	**[-7.19e-05**	**5.22e-05]**
Load coefficients =-5.64e-05	**[-0.000145**	**3.26e-05]**

	COI coefficients =0.00852	[0.00564	0.0114]
%%			
Linear regression on damping ratio			
-) DampingRatio(%)= (Solar)*(-0.00132)+(Wind)*(-7.62e-05)+(load)*(3.08e-05)+ (COI)* (0.00262)+(0.0123)*1000			
	Solar coefficients =-0.00132	[-0.00341	0.000761]
	Wind coefficients =-7.62e-05	[-0.000338	0.000185]
	Load coefficients =3.08e-05	[-0.000142	0.000203]
	COI coefficients =0.00262	[-0.00115	0.00638]

Correlation Analysis on Mode Frequency

QR is applied on the mode frequency to study the correlation with wind generation. Model responses corresponding to quantile levels (τ) of 95%, 50%, and 5% are summarized in Figure 5-15 for the mode frequency. The corresponding coefficients of QR and their confidence intervals, as well as the correlation analysis results from LSR, are summarized in Table 5-12. For $\tau = 5\%, 50\%, 95\%$, the slope is positive and within the confidence intervals. LSR results are similar to the QR results. We can conclude that the mode frequency increases with the increase in wind generation.

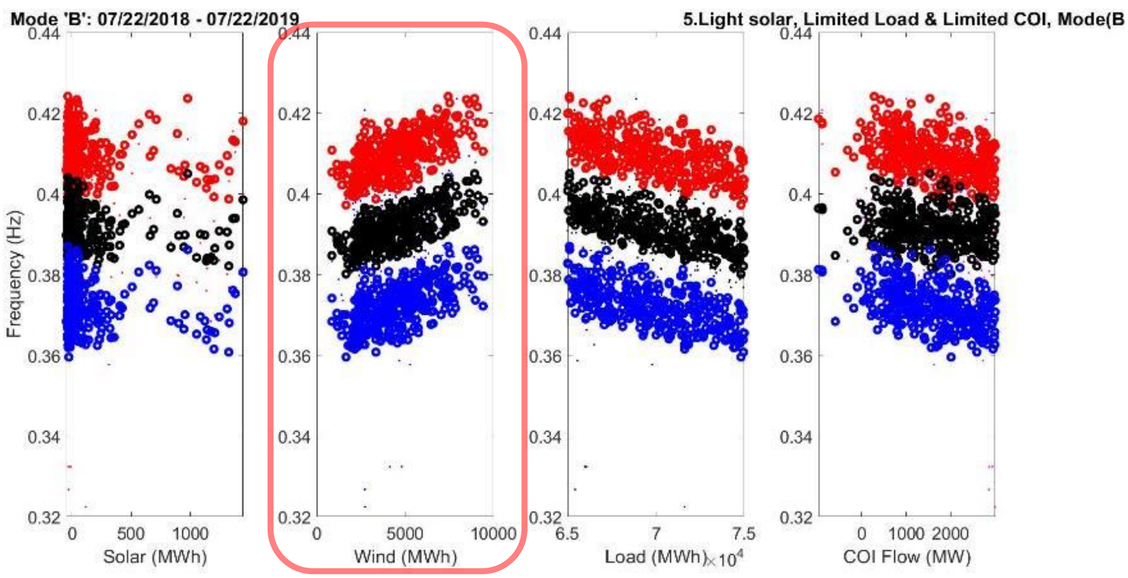

Figure 5-15. Responses of QR model for the mode frequency of NS-B (red = 95%; black = 50%; blue = 5%).

Table 5-12. Identified QR/LSR models mode frequency and confidence intervals of their coefficients.

Quantile regression on Frequency			
95%) Frequency(Hz)=(Solar)*(-8.98e-08)+(Wind)*(1.95e-06)+(load)*(-1.14e-06)+(COI)*(-2.66e-06)+(0.000485)*1000			
	Solar coefficients =-8.98e-08	[-1.52e-07	-2.71e-08]
	Wind coefficients =1.95e-06	[1.39e-06	2.51e-06]
	Load coefficients =-1.14e-06	[-1.32e-06	-9.62e-07]

COI coefficients =-2.66e-06 [-3.83e-06 -1.49e-06]

50%) Frequency(Hz)=(Solar)*(-1.43e-07)+(Wind)*(1.78e-06)+(load)*(-1.19e-06)+(COI)*(-1.18e-06)+(0.000469)*1000

Solar coefficients =-1.43e-07 [-2.36e-07 -5.14e-08]

Wind coefficients =1.78e-06 [1.48e-06 2.08e-06]

Load coefficients =-1.19e-06 [-1.33e-06 -1.05e-06]

COI coefficients =-1.18e-06 [-1.78e-06 -5.79e-07]

5%) Frequency(Hz)=(Solar)*(-9.05e-08)+(Wind)*(1.88e-06)+(load)*(-1.21e-06)+(COI)*(-2.84e-06)+(0.000453)*1000

Solar coefficients =-9.05e-08 [-1.67e-07 -1.37e-08]

Wind coefficients =1.88e-06 [1.18e-06 2.57e-06]

Load coefficients =-1.21e-06 [-1.47e-06 -9.54e-07]

COI coefficients =-2.84e-06 [-4.26e-06 -1.43e-06]

%%

Linear regression on Frequency

-) Frequency(Hz)=(Solar)*(-8.89e-08)+(Wind)*(1.9e-06)+(load)*(-1.17e-06)+(COI)*(-2.73e-06)+(0.000468)*1000

Solar coefficients =-8.89e-08 [-4.85e-06 4.67e-06]

Wind coefficients =1.9e-06 [1.18e-06 2.62e-06]

Load coefficients =-1.17e-06 [-1.65e-06 -6.92e-07]

COI coefficients =-2.73e-06 [-4.29e-06 -1.16e-06]

5.2.2.1.3 Case III. Impact of Total Load

Correlation Analysis on Mode DR

QR is applied on the mode DR to study the correlation with the load. Model responses corresponding to quantile levels (τ) of 95%, 50%, and 5% are summarized in Figure 5-16 for mode DR. The corresponding coefficients of QR and their confidence intervals, as well as the correlation analysis results from LSR, are summarized in Table 5-13. For $\tau = 5\%, 50\%, 95\%$, the slope is positive and within the confidence intervals. The correlation analysis results obtained from LSR are similar to the QR results. In general, the mode DR increases when the total load increases.

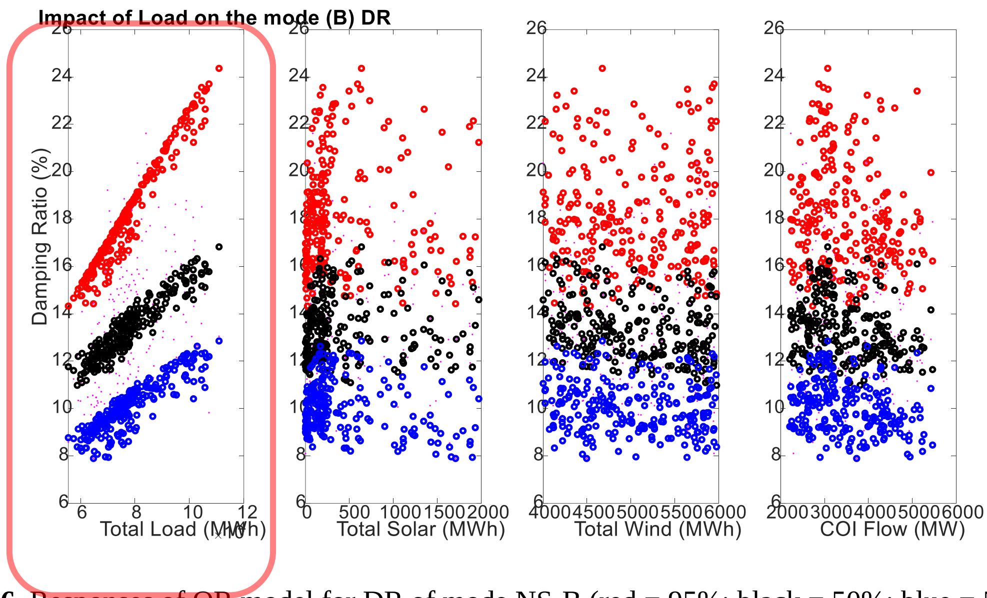

Figure 5-16. Responses of QR model for DR of mode NS-B (red = 95%; black = 50%; blue = 5%).

Table 5-13. Identified QR/LSR models for mode DR and confidence intervals of their coefficients.

Quantile regression on damping ratio		
95%) DampingRatio(%)=(Solar)*(-0.00462)+(Wind)*(-0.000691)+(load)*(0.000294)+(COI)*(-0.000231)+(0.00138)*1000		
	Solar coefficients =-0.00462	**[-0.00613 -0.00312]**
	Wind coefficients =-0.000691	**[-0.000994 -0.000387]**
	Load coefficients =0.000294	**[0.000271 0.000316]**
	COI coefficients =-0.000231	**[-0.000435 -2.75e-05]**
50%) DampingRatio(%)=(Solar)*(-0.00152)+(Wind)*(-1.86e-05)+(load)*(0.000178)+(COI)*(-0.000295)+(0.00259)*1000		
	Solar coefficients =-0.00152	**[-0.00229 -0.000759]**
	Wind coefficients =-1.86e-05	**[-0.000114 7.69e-05]**
	Load coefficients =0.000178	**[0.000162 0.000195]**
	COI coefficients =-0.000295	**[-0.00042 -0.00017]**
5%) DampingRatio(%)=(Solar)*(-0.00121)+(Wind)*(-0.000217)+(load)*(8.97e-05)+(COI)*(-0.000723)+(0.00663)*1000		
	Solar coefficients =-0.00121	**[-0.00214 -0.000293]**
	Wind coefficients =-0.000217	**[-0.00042 -1.34e-05]**
	Load coefficients =8.97e-05	**[6.99e-05 0.000109]**
	COI coefficients =-0.000723	**[-0.000888 -0.000559]**
%%		
Linear regression on damping ratio		
-) DampingRatio(%)=(Solar)*(-0.00216)+(Wind)*(-0.00023)+(load)*(0.000174)+(COI)*(-0.000417)+(0.00405)*1000		
	Solar coefficients =-0.00216	**[-0.00365 -0.00067]**
	Wind coefficients =-0.00023	**[-0.000589 0.000129]**
	Load coefficients =0.000174	**[0.00014 0.000208]**
	COI coefficients =-0.000417	**[-0.000659 -0.000176]**

This observation is not consistent with the model-based study observations (described in the next section) that the DR shall decrease with the increase of system loads. Thus, we carry out further studies to see

whether there are any other factors such as generation mixes in different control areas that could explain the observation. Following the intuition developed from model-based simulation studies, the conventional generations from different control areas are selected to explain the observed damping increase using the same dataset as above. First, conventional generations including hydro, coal, and natural gas are summed together from each area because they share similar electromechanical dynamics. Then, the contributions of the conventional generations from each area are correlated to the DR. Those areas whose generations can be positively correlated to the DR are identified as 1. CISO, 2. LDWP, 7. PACW, 9. WACM, and grouped together to reduce the number of the explanatory variables. Those areas whose generations can be negatively correlated to the DR are identified as 3. IPCO, 4. NEVP, 6. PACE, 11. PNM, and grouped together to reduce the number of the explanatory variables. Their geographic distributions are summarized in Figure 5-17.

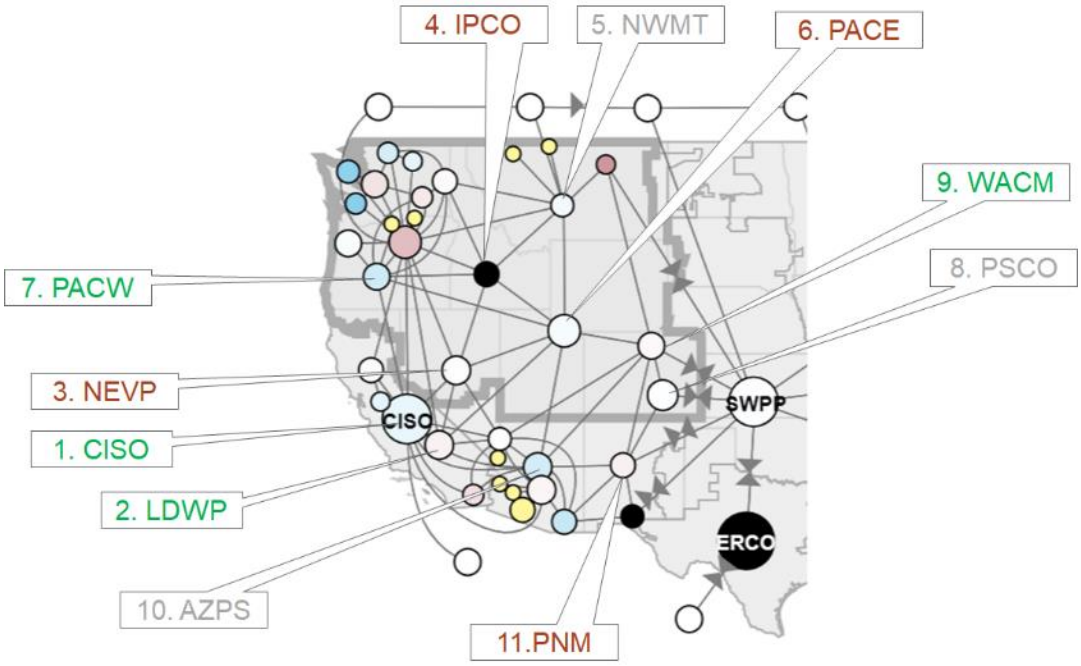

Figure 5-17. Geographic distribution of the control areas whose generations can be **positively** and **negatively** correlated to the DR of NS-B.

QR is applied to study the correlation between the DR of NS-B, positively correlated generation, negatively correlated generations, total solar generation, total wind generation, and COI flow. The results are summarized in Figure 5-18. The figure suggests that increasing DR may also be explained by the increasing generation in the areas of CISO, LDWP, PACW, WACM, et al. To study whether the explanation is sufficient, residuals for the linear model corresponding to $\tau = 50\%$ are estimated and correlated to the total load. The correlation studies are summarized in Figure 5-19 and Table 5-14. There are no significant correlations between the residuals of the DR and the total load. This observation

suggests that the generation mix from identified generation areas can fully explain the increasing DR without resorting to the total load.

Another interesting observation can be made on the relationship between the total load and the positively and negatively correlated generations. Their relationships are summarized in Figure 5-20. The correlation is positive for the positively correlated generations (i.e., 1. CISO, 2. LDWP, 7. PACW, 9. WACM), while the correlation is negative for the negatively correlated generations (3. IPCO, 4. NEVP, 6. PACE, 11. PNM). This observation explains why the correlation between the generation mixes and the DR can be established without resorting to the total load.

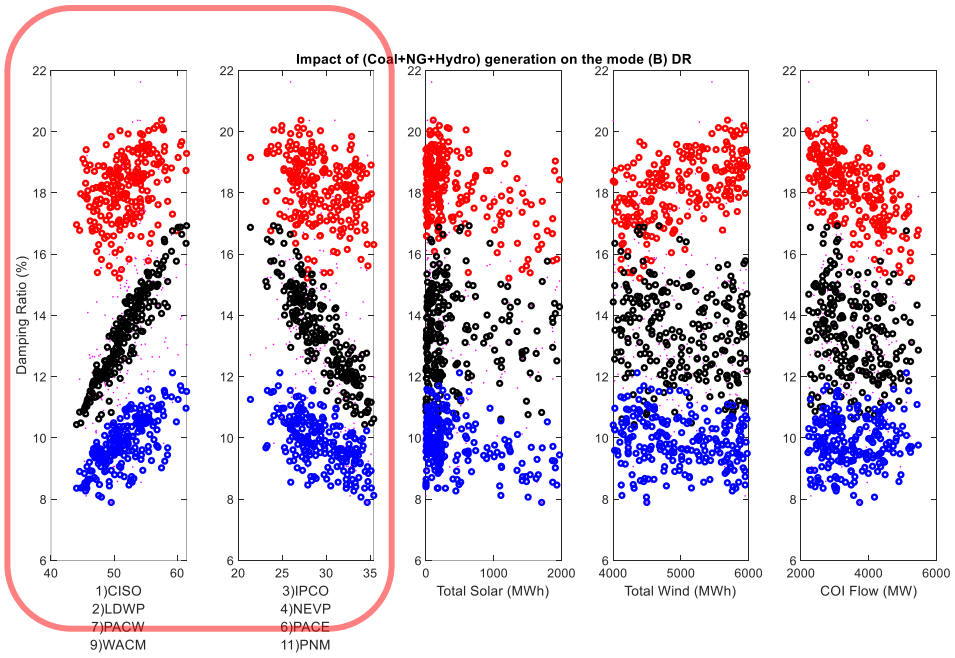

Figure 5-18. Responses of QR model for the DR of NS-B with generation replacing total load (red = 95%; black = 50%; blue = 5%).

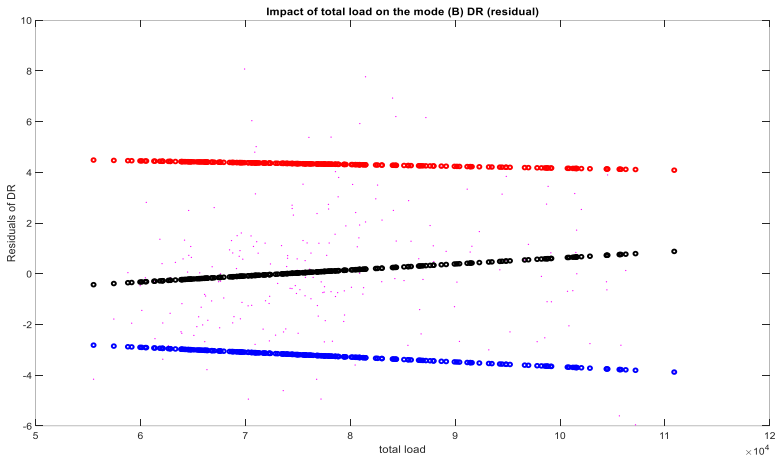

Figure 5-19. Correlation between DR residuals and total load (red = 95%; black = 50%; blue = 5%).

Table 5-14. Identified QR models for residuals of the mode DR and total load.

%%%%%%%%%%%%%%%%%%%%%%%%%%%%%
================ Quantile regression on the residual ==============
95%) DampingRatio(%)=(total load)*(-7.22e-06)+1000*(0.00489)
total load coefficients =-7.22e-06 [-4.35e-05 0.194]
50%) DampingRatio(%)=(total load)*(2.37e-05)+1000*(-0.00175)
total load coefficients =2.37e-05 [9.78e-06 0.3]
5%) DampingRatio(%)=(total load)*(-1.92e-05)+1000*(-0.00175)
total load coefficients =-1.92e-05 [-4.72e-05 0.177]

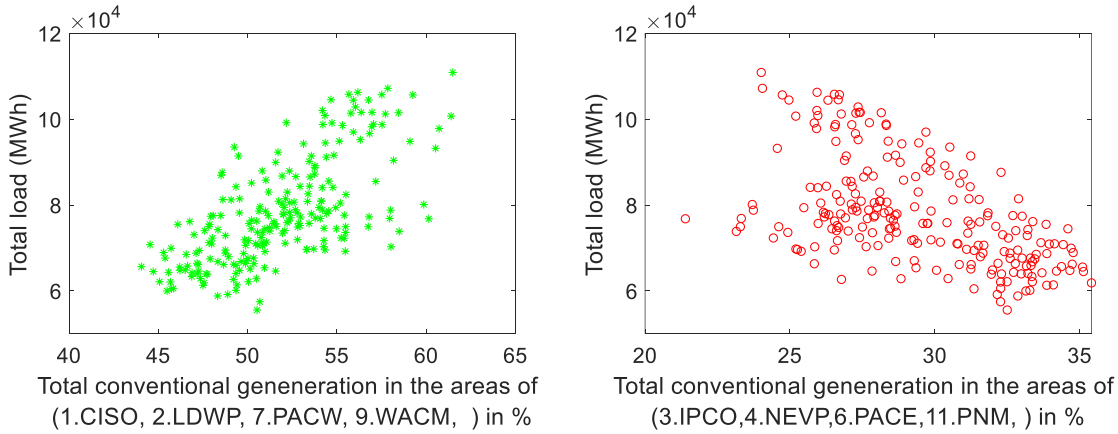

Figure 5-20. Relationship between total load and positively and negatively correlated generations.

Correlation Analysis on Mode Frequency

QR is applied on the frequency of the 0.4 Hz oscillation mode. Model responses corresponding to quantile levels (τ) of 95%, 50%, and 5% are summarized in Figure 5-21 for the mode frequency. The corresponding coefficients of QR and their confidence intervals, as well as the correlation analysis results

from LSR, are summarized in Table 5-15. For $\tau = 5\%, 50\%, 95\%$, the slope is negative within the confidence intervals. LSR results are similar to the QR results. Hence, it is evident that the increase in load can be correlated to the lower oscillation frequency of the 0.4 Hz inter-area mode.

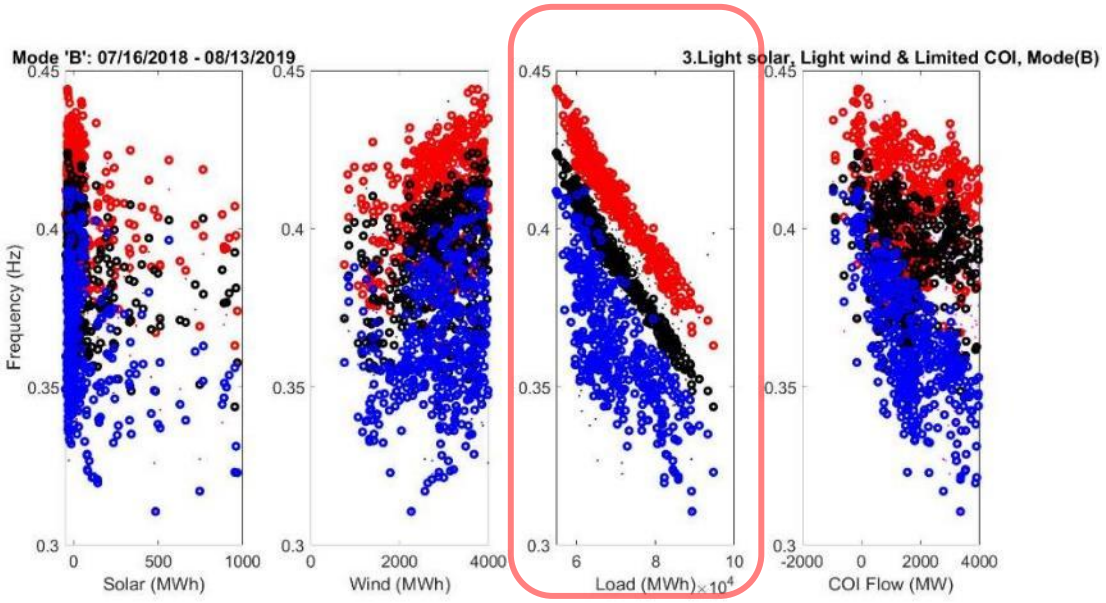

Figure 5-21. Responses of QR model for the frequency of NS-B (red = 95%; black = 50%; blue = 5%).

Table 5-15. Identified QR/LSR models for mode frequency and confidence intervals of their coefficients.

Quantile regression on Frequency		
95%) Frequency(Hz)=(Solar)*(-3.54e-06)+(Wind)*(3.94e-06)+(load)*(-1.77e-06)+(COI)*(-2.59e-06)+(0.000527)*1000		
	Solar coefficients =-3.54e-06	**[-5.96e-06 -1.13e-06]**
	Wind coefficients =3.94e-06	**[2.88e-06 5e-06]**
	Load coefficients =-1.77e-06	**[-1.85e-06 -1.69e-06]**
	COI coefficients =-2.59e-06	**[-3.26e-06 -1.93e-06]**
50%) Frequency(Hz)=(Solar)*(-2.88e-07)+(Wind)*(2.58e-06)+(load)*(-1.88e-06)+(COI)*(-2.1e-06)+(0.000518)*1000		
	Solar coefficients =-2.88e-07	**[-4.28e-07 -1.48e-07]**
	Wind coefficients =2.58e-06	**[1.71e-06 3.45e-06]**
	Load coefficients =-1.88e-06	**[-1.96e-06 -1.8e-06]**
	COI coefficients =-2.1e-06	**[-2.71e-06 -1.48e-06]**
5%) Frequency(Hz)=(Solar)*(-7.64e-06)+(Wind)*(5.36e-06)+(load)*(-1.46e-06)+(COI)*(-1.15e-05)+(0.000471)*1000		
	Solar coefficients =-7.64e-06	**[-1.44e-05 -8.89e-07]**
	Wind coefficients =5.36e-06	**[3.54e-06 7.19e-06]**
	Load coefficients =-1.46e-06	**[-1.62e-06 -1.31e-06]**
	COI coefficients =-1.15e-05	**[-1.3e-05 -9.95e-06]**
%%		
Linear regression on Frequency		
-) Frequency(Hz)=(Solar)*(-3.64e-06)+(Wind)*(3.24e-06)+(load)*(-1.73e-06)+(COI)*(-4.45e-06)+(0.000508)*1000		
	Solar coefficients =-3.64e-06	**[-1.2e-05 4.69e-06]**
	Wind coefficients =3.24e-06	**[1.24e-06 5.25e-06]**
	Load coefficients =-1.73e-06	**[-1.92e-06 -1.54e-06]**
	COI coefficients =-4.45e-06	**[-5.8e-06 -3.1e-06]**

5.2.2.1.4 Case IV: Impact of COI Flow

Correlation Analysis on Mode DR

QR is applied on the mode DR to study the correlation with COI flow. Model responses corresponding to quantile levels (τ) of 95%, 50%, and 5% are summarized in Figure 5-22 for mode DR. The corresponding coefficients of QR and their confidence intervals, as well as the correlation analysis results from LSR, are summarized in Table 5-16. For $\tau = 5\%, 50\%\ and\ 95\%$, the slope is negative within the confidence intervals. LSR results show negative correlation and within the confidence intervals. In general, the DR drops down with the increase in COI flow.

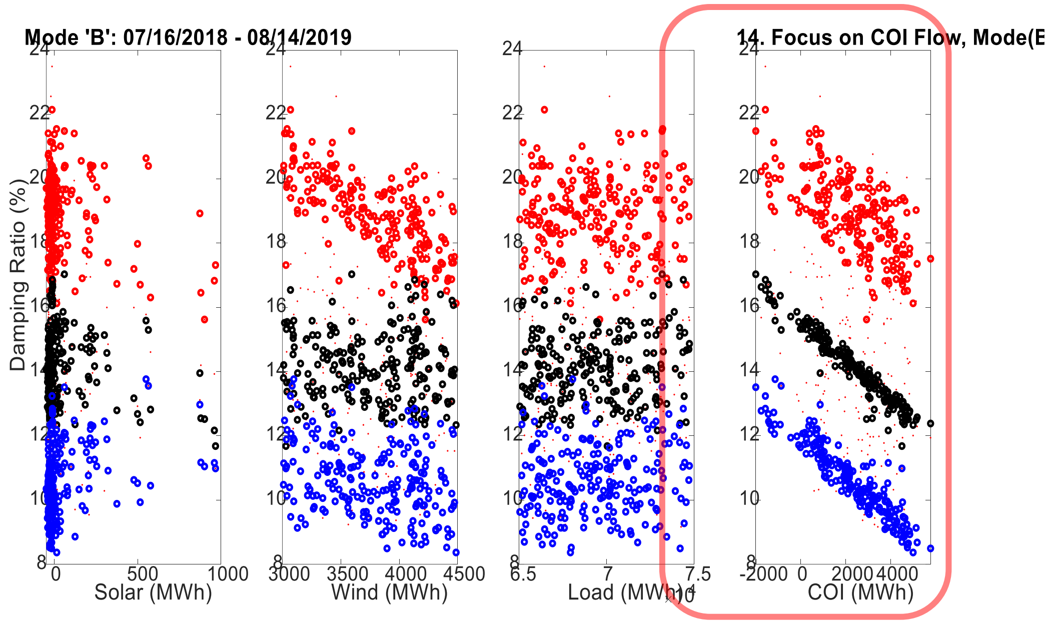

Figure 5-22. Responses of QR model for DR of NS-B (red = 95%; black = 50%; blue = 5%).

Table 5-16. Identified QR/LSR models for mode DR and confidence intervals of their coefficients.

Quantile regression on damping ratio			
95%) DampingRatio(%)=(Solar)*(-0.0024)+(Wind)*(-0.00214)+(load)*(6.5e-05)+(COI)*(-0.000461) +(0.0236)*1000			
	Solar coefficients =-0.0024	**[-0.00458**	**-0.000218]**
	Wind coefficients =-0.00214	**[-0.00292**	**-0.00136]**
	Load coefficients =6.5e-05	**[-7e-06**	**0.000137]**
	COI coefficients =-0.000461	**[-0.000677**	**-0.000244]**
50%) DampingRatio(%)=(Solar)*(-0.00139)+(Wind)*(-0.00016)+(load)*(6.15e-05)+(COI)*(-0.000613) +(0.012)*1000			
	Solar coefficients =-0.00139	**[-0.0026**	**-0.000179]**
	Wind coefficients =-0.00016	**[-0.000524**	**0.000204]**
	Load coefficients =6.15e-05	**[-3.99e-06**	**0.000127]**
	COI coefficients =-0.000613	**[-0.000727**	**-0.000499]**
5%) DampingRatio(%)=(Solar)*(0.00132)+(Wind)*(-0.000668)+(load)*(3.95e-05)+(COI)*(-0.000611) +(0.0117)*1000			
	Solar coefficients =0.00132	**[0.00014**	**0.0025]**
	Wind coefficients =-0.000668	**[-0.00114**	**-0.000194]**
	Load coefficients =3.95e-05	**[-1.15e-05**	**9.05e-05]**
	COI coefficients =-0.000611	**[-0.00076**	**-0.000463]**
%%			
Linear regression on damping ratio			
-) DampingRatio(%)=(Solar)*(-0.0014)+(Wind)*(-0.00041)+(load)*(5.82e-05)+(COI)*(-0.000542) +(0.0132)*1000			
	Solar coefficients =-0.0014	**[-0.00345**	**0.000642]**
	Wind coefficients =-0.00041	**[-0.00128**	**0.000458]**
	Load coefficients =5.82e-05	**[-7.74e-05**	**0.000194]**
	COI coefficients =-0.000542	**[-0.000756**	**-0.000328]**

Correlation Analysis on Mode Frequency

QR is applied on mode frequency to study the correlation with COI flow. Model responses corresponding to quantile levels (τ) of 95%, 50%, and 5% are summarized in Figure 5-23 for the mode frequency. The corresponding coefficients of QR and their confidence intervals, as well as the correlation analysis results from LSR, are summarized in Table 5-17. For $\tau = 5\%, 50\%, 95\%$, the slope can be positive, zeros, or negative. LSR results are similar to the QR results. In summary, it is difficult to judge how the mode frequency of the 0.4 Hz mode is related to COI flow.

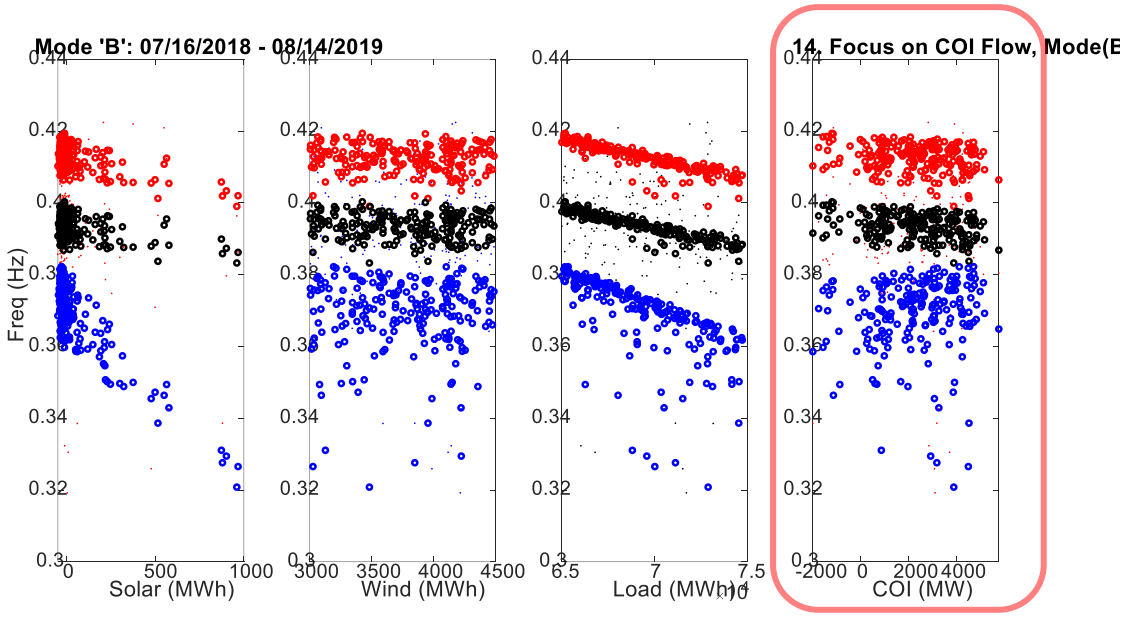

Figure 5-23. Responses of QR model for the frequency of NS-B (red = 95%; black = 50%; blue = 5%).

Table 5-17. Identified QR/LSR models for mode frequency and confidence intervals of their coefficients.

Quantile regression on frequency		
95%) Frequency(Hz)=(Solar)*(-1e-05)+(Wind)*(-3.93e-07)+(load)*(-1.09e-06)+(COI)*(-4.4e-07) +(0.000491)*1000		
Solar coefficients =-1e-05	**[-1.9e-05**	**-9.98e-07]**
Wind coefficients =-3.93e-07	**[-9.07e-07**	**1.22e-07]**
Load coefficients =-1.09e-06	**[-1.42e-06**	**-7.58e-07]**
COI coefficients =-4.4e-07	**[-1.11e-06**	**2.29e-07]**
50%) Frequency(Hz)=(Solar)*(-6.29e-06)+(Wind)*(-4.56e-07)+(load)*(-1.08e-06)+(COI)*(-5.1e-07) +(0.000472)*1000		
Solar coefficients =-6.29e-06	**[-1.17e-05**	**-9.11e-07]**
Wind coefficients =-4.56e-07	**[-1.25e-06**	**3.37e-07]**
Load coefficients =-1.08e-06	**[-1.4e-06**	**-7.66e-07]**
COI coefficients =-5.1e-07	**[-1.05e-06**	**2.68e-08]**
5%) Frequency(Hz)=(Solar)*(-4.65e-05)+(Wind)*(-3.67e-08)+(load)*(-1.98e-06)+(COI)*(6.11e-07) +(0.000507)*1000		
Solar coefficients =-4.65e-05	**[-6.75e-05**	**-2.56e-05]**
Wind coefficients =-3.67e-08	**[-8.23e-08**	**9e-09]**

Load coefficients =-1.98e-06 [-2.62e-06 -1.33e-06]

COI coefficients =6.11e-07 [-3.93e-07 1.62e-06]

%%

Linear regression on frequency

Linear) frequency (Hz)=(Solar)*(-9.63e-06)+(Wind)*(-4.03e-07)+(load)*(-1.13e-06)+(COI)*(-4.45e-07) +(0.000474)*1000

Solar coefficients =-9.63e-06 [-2.22e-05 2.95e-06]

Wind coefficients =-4.03e-07 [-5.74e-06 4.93e-06]

Load coefficients =-1.13e-06 [-1.96e-06 -2.95e-07]

COI coefficients =-4.45e-07 [-1.76e-06 8.7e-07]

5.3 Summary

The correlation analysis results are summarized in Table 5-18. The data-based analysis shows that:

- The DR of NS-A will decrease with the increase of the penetration level of solar and wind generation.
- The DR of both NS-A and NS-B will decrease with the increase of the COI power flow (from north to south).
- Impact from the increase of the penetration level of solar and wind generation on the DR of NS-B is not clear, in other words the data-based correlation analysis does not show a strong correlation between the DR of NS-B and solar and wind generation penetration levels.

In many cases conclusions are difficult to draw because of noise and limited amounts of data. The data-based correlation analysis can only identify the phenomena that happened at the same time during the observed duration. The results do not indicate the causality.

Table 5-18. Summary on the impact of mixed Generation on the inter-area oscillation modes.

Increased Variables	Damping Ratio (%)		Frequency (Hz)	
	NS-A	**NS-B**	**NS-A**	**NS-B**
Solar	Decrease	Not clear	Decrease	Decrease
Wind	Decrease	Not clear	Increase	Increase
Load	Not clear	Increase (alternative explanation)	Decrease	Decrease
COI Flow	Decrease	Decrease	Increase	Not clear

6.0 Model-Based Oscillation Assessment

Several states throughout the United States have established RPS to promote clean and sustainable energy sources. Achieving these mandates set by RPS will require replacing traditional synchronous machines with inverter-based RES generation. This shift in the generation mix will have a significant impact on system behavior including natural oscillations. Oscillations are inherent in power systems because of their electro-mechanical nature. These oscillations can either involve generators in close area oscillating against each other (local oscillations resulting from local modes) or generators in different areas oscillating against each other (inter-area oscillations resulting from inter-area modes). The system oscillatory behavior is largely determined by the system topology and stress. A system having large power transfer through weakly connected transmission lines is more likely to be vulnerable to system events and prone to unstable oscillations. Synchronous machines replaced by inverter-based generation sources will result in changes to the system topology and other grid properties, such as system inertia which are usually associated with the synchronous machines. These changes in topology and inertia will further result in changes to the system oscillatory behavior. It is of critical significance to fully understand the impact of these changes to maintain reliable power systems operations.

In this section, a thorough model-based assessment of the changes in the system oscillatory behavior caused by a change in the generation mix is discussed. This change in the generation-mix represents a future scenario where many of the existing synchronous generators will be replaced by fully converter-based RES generation sources. Therefore, for this analysis traditional synchronous machines were replaced by fully converter-based generation, representing inverter-based wind and solar generation sources, in various proportions to analyze the impact on system oscillations. Several scenarios were considered including area-specific increase in RES penetration, systemwide increase in RES penetration, and changes of flows across major inter-ties. Details of the model, methodology, and results are discussed next.

6.1 Description of the WECC model

The model-based wide-area oscillation assessment was carried out using 2018 heavy summer (HS) operating WECC model as a base case to identify trends associated with increased RES penetration on system modes for different scenarios, which will be discussed later. The 2018 HS case has a RES penetration level of ~8.5% with a total system inertia of 919 GW-s and total system load of 173 GW. The area-wise generation mix and inertia for the base case is provided in Figure 6-1.

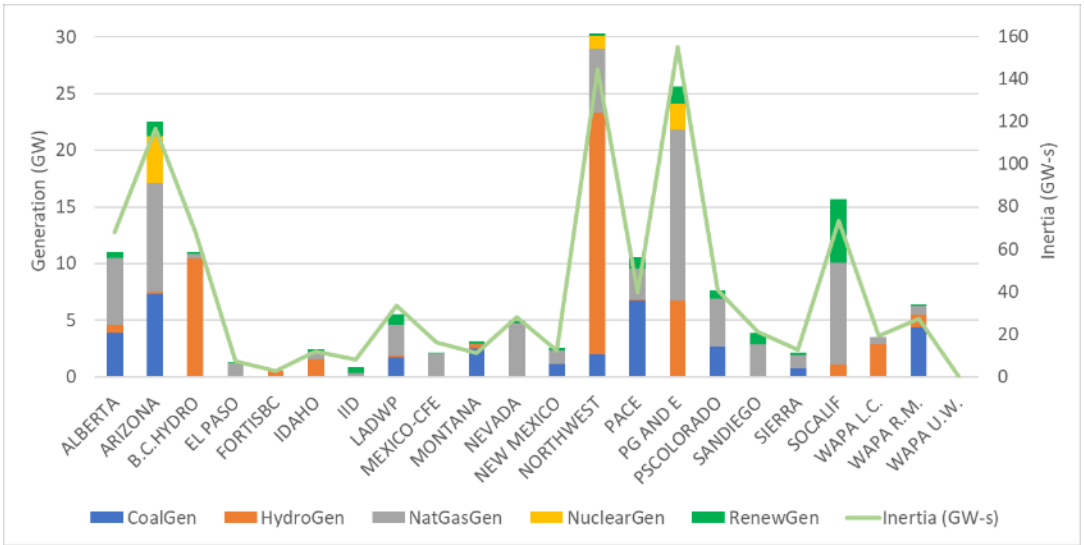

Figure 6-1. Area-wise generation mix and inertia for 2018 HS operating case.

Comparative Analysis of RES Generation between Model and Actual Data

A comparative analysis was carried out between the actual RES generation, which includes both solar and wind, recorded between July 2018 and August 2019 for the WECC system and RES generation in the 2018 HS operating case. The result of the comparison is summarized in Table 6-1, where "Max. Renewable" for model refers to the total capacity of online wind and solar generation sources and "Max. Renewable" for data refers to the sum of the maximum RES generation observed in each area between July 2018 and August 2019. The renewable generation was also compared between the HS case and the actual data corresponding to the instant of peak load. As seen in Table 6-1, both values matched quite well, but there was some discrepancy in the peak load observed in the actual data as compared to the model. This might have been the case as the WECC model does not include distributed energy resource generation. The comparison was also done for the estimates of NS-A and NS-B systems calculated using the model-based and actual measurements corresponding to the instant of peak load. Table 6-1 also shows that estimates obtained using actual and model-based measurements have a good match.

Table 6-1. A comparative analysis of the actual RES generation and model-based RES generation in the WECC system.

	Data (July 2018 to August 2019)	**Model (HS 2018)**
Max. Renewable	26,135 MWh	29,397 MW
Peak Load	120,828 MWh @ 6 pm July 24, 2018	172,908 MW (Not considering DER generation)

Renewable @ Peak Load	14,585 MWh	15,077 MW
NS-A Freq @ Peak Load	0.2254 Hz	0.244 Hz
NS-A Damping @ Peak Load	14.70 %	14.9%
NS-B Freq @ Peak Load	0.3772 Hz	0.362 Hz
NS-B Damping @ Peak Load	7.75 %	7.8 %

6.2 Simulation Scenarios

In this study, several simulation scenarios were analyzed to identify trends associated with the impact of increased RES penetration level on system modes. A detailed description of each simulation scenario is discussed next. In each scenario, a group of generators in one or more areas was selected and replaced by fully converter-based generation sources representing inverter-based solar and wind generation sources.

6.2.1 Systemwide Increase in RES Penetration – Scenario S1

In this simulation, synchronous generators were replaced by RES simultaneously in all areas of the WECC system by a certain percentage based on the generation in each area. Here, coal-based generation was replaced first, followed by natural gas, nuclear, and others. Generation based on clean sources of energy such as hydro and geothermal were not replaced. Figure 6-2 provides information on area-wise and systemwide RES penetration levels for different cases, Figure 6-3 provides corresponding inertia. In Figure 6-2 and from here onward, unless otherwise specified, Case 0 refers to the 2018 HS operating base case having a systemwide RES penetration level of ~8.5%. As a major proportion of generation in the Northwest and B.C. comes from hydro sources, RES penetration level in these areas could be increased only up to 30% and 8%, respectively. The total systemwide RES penetration level was increased to 70% in Case 12. Power flow, system load, and generation dispatch remained the same for all cases. All other scenarios described in this section are derived from this scenario.

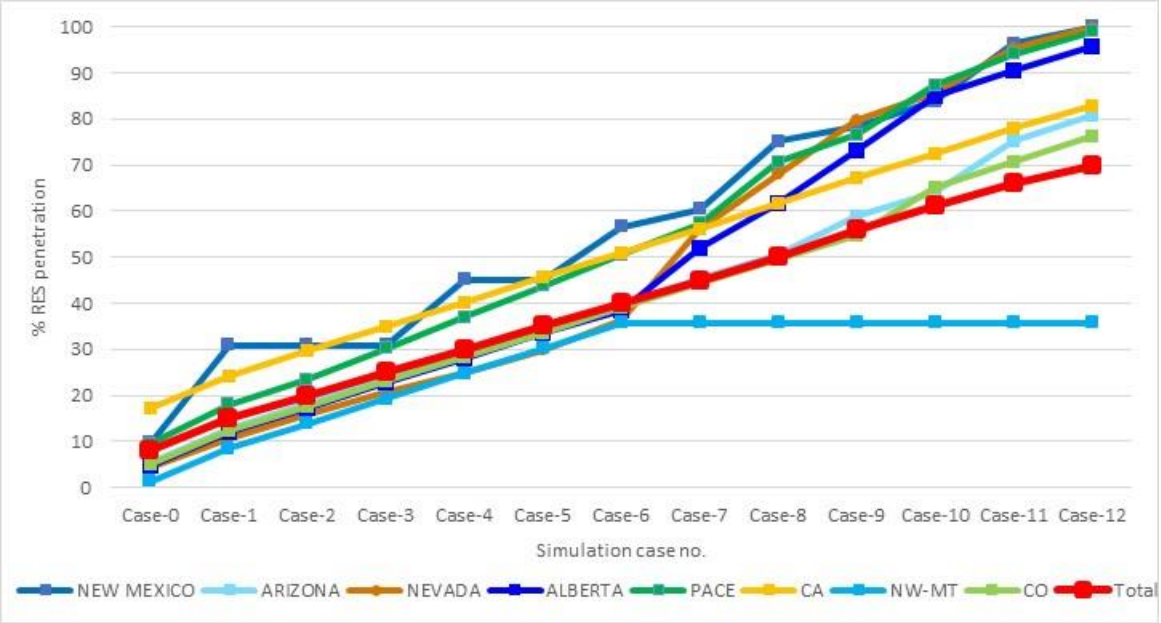

Figure 6-2. Percent RES penetration in several areas and total system penetration for different cases in Scenario S1.

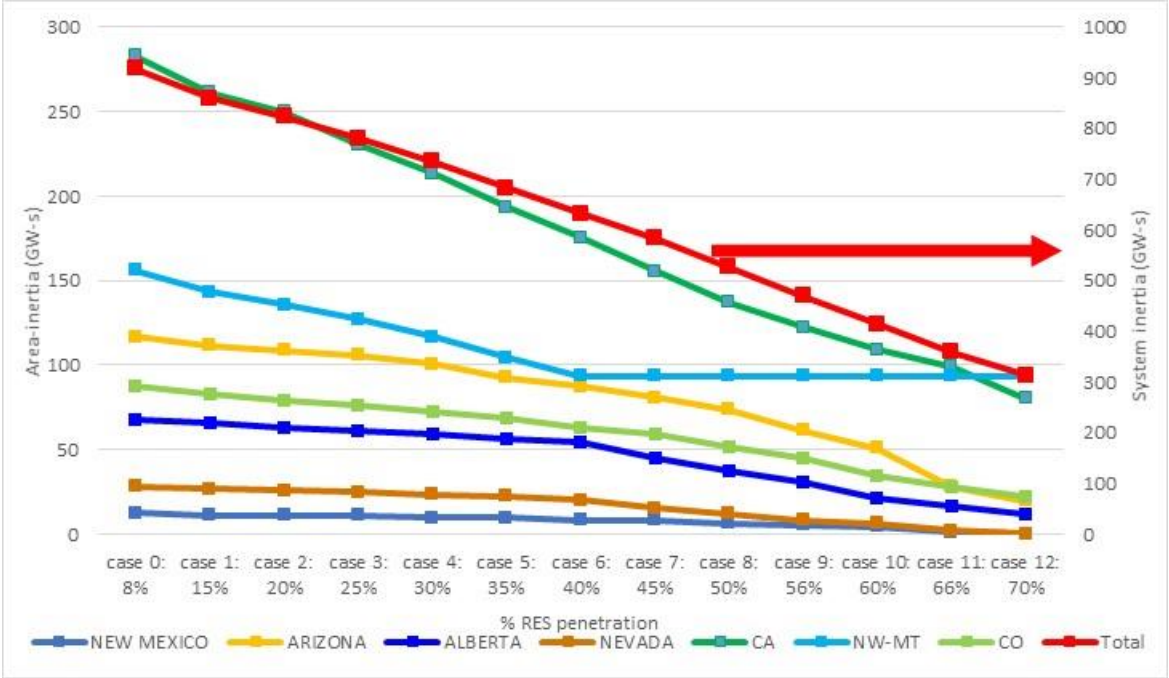

Figure 6-3. Area-wise and total system inertia as a function of percent RES penetration for different cases in Scenario S1.

.

6.2.2 Scenario-1 with the Order of Replaced Generators Reversed – Scenario S2

This is a modified version of Scenario S1. In this scenario, the order in which the group of generators was replaced to obtain an additional 12 cases in Scenario S1 was reversed. This means the generators replaced in Case-1 in Scenario S1 were replaced in case 12 in Scenario S2. Generators replaced in case 2 in Scenario S1 were replaced in case 11 in Scenario S2, and so on. This scenario examined if the trends observed in the system modes were a function of increased renewable penetration level or were determined by the group of generators replaced. Figure 6-4 provides information on area-wise and systemwide RES penetration levels for different cases. Figure 6-5 provides corresponding inertia, and Figure 6-6 shows the corresponding number of online synchronous generators in this scenario.

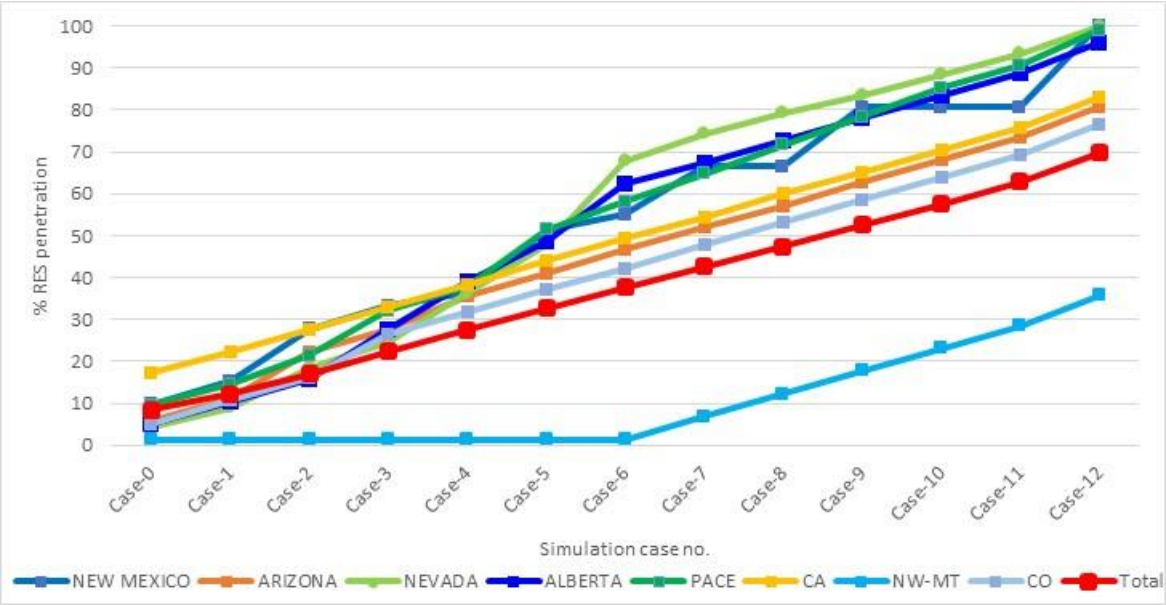

Figure 6-4. Percent RES penetration in several areas and total system penetration for different cases in Scenario S2.

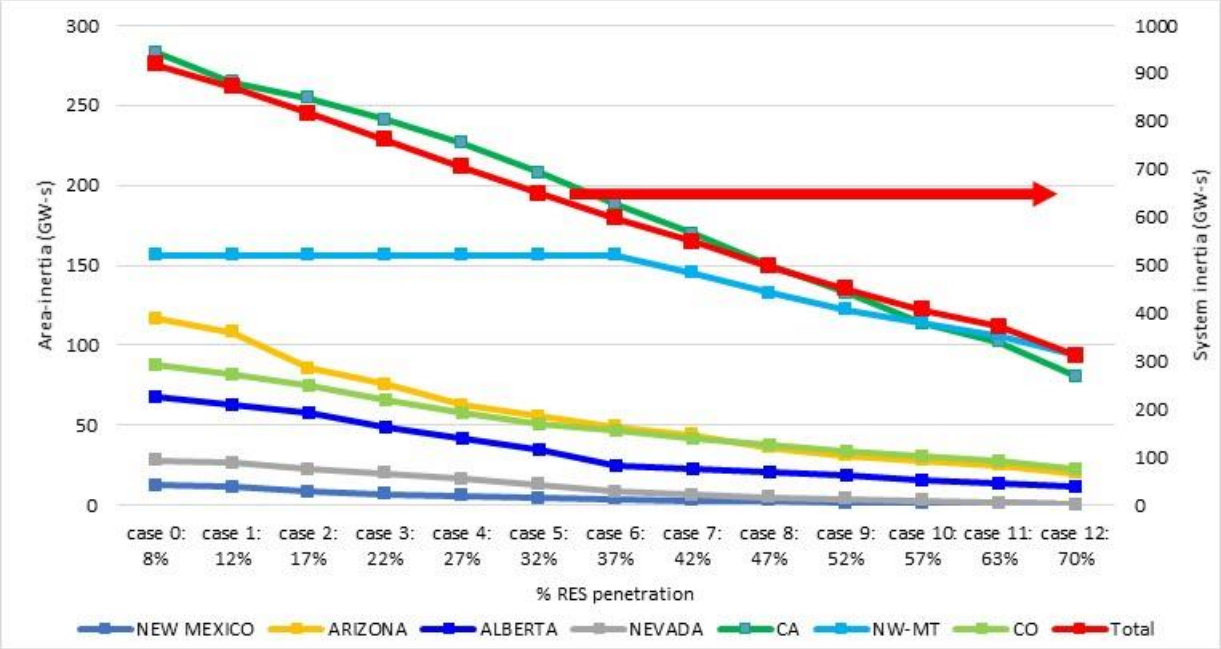

Figure 6-5. Area-wise and total system inertia as a function of percent RES penetration for the different cases in Scenario S2.

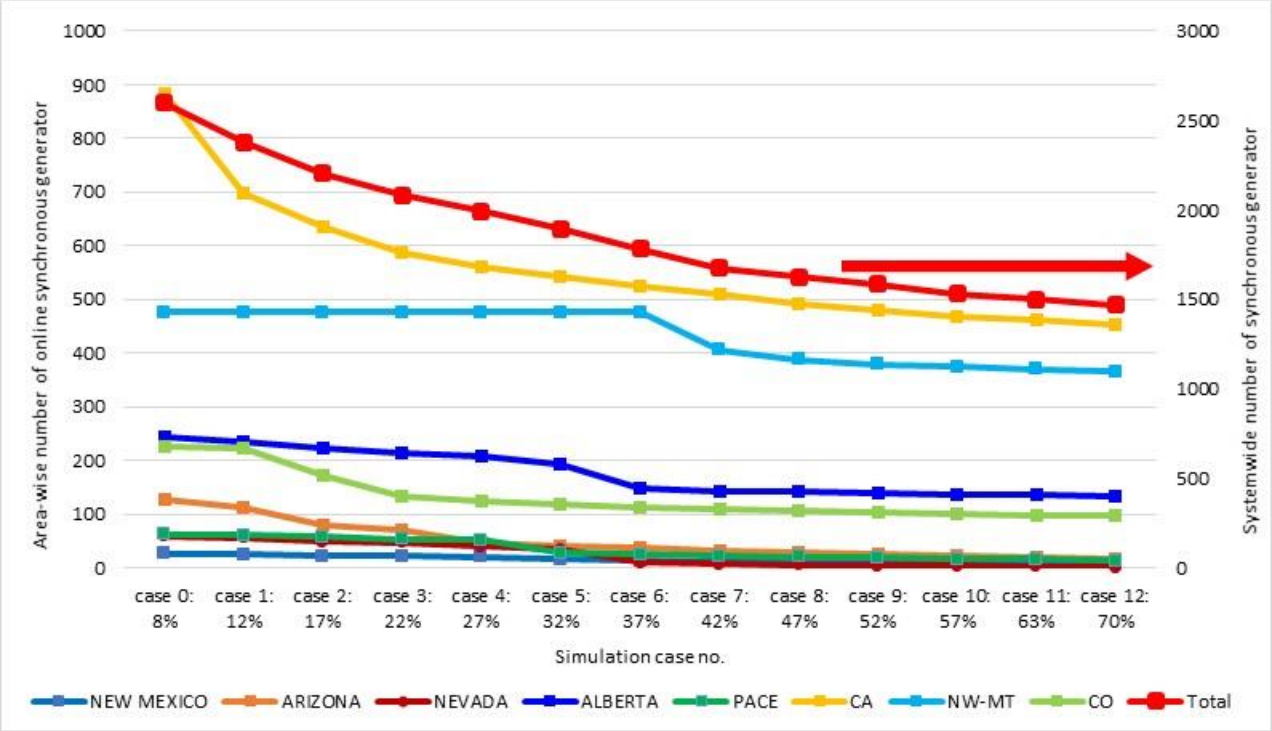

Figure 6-6. Number of online generators area-wise and system-wise for different cases in Scenario S2.

6.2.3 Increase in RES Penetration Level in Alberta Only – Scenario S3

In this scenario, RES penetration level was increased only in Alberta to assess the impact of increased penetration on system modes. Generators in Alberta have the highest participation factor in NS-A with the generators in all other areas having a small participation factor as shown in Figure 6-7; therefore, generators in Alberta play a significant role in determining oscillatory behavior of NS-A. For NS-B, participation factor of generators in Alberta is high along with generators in some other areas such as B.C. Hydro and Northwest as shown in Figure 6-7. Therefore, to analyze the impact of area-specific increase in the renewable penetration on system modes, the Alberta area was chosen.

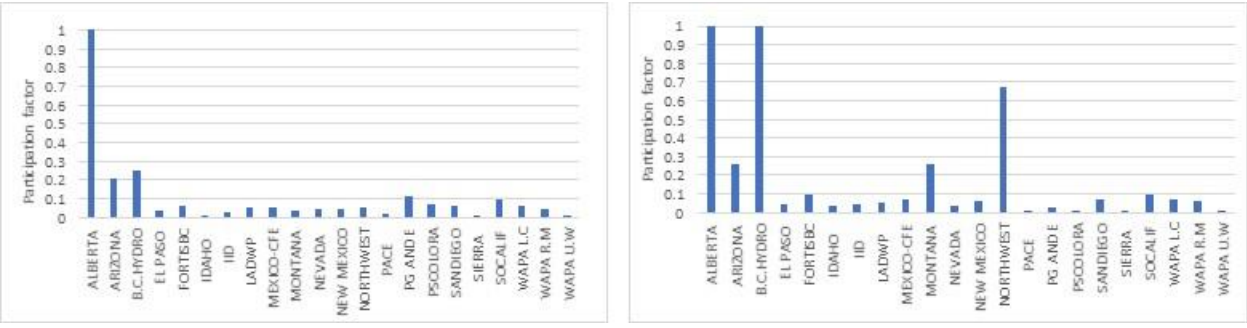

Figure 6-7. Maximum of the participation factor of generators in each area for NS-A (left) and NS-B (right) modes for the base case obtained by Small-signal Stability Analysis Tool (SSAT).

The group of generators replaced in Alberta in this scenario is the same as in Scenario S1 and in the same order for the additional 12 cases, the difference being the generators were not replaced in the other areas in this scenario. Figure 6-8 and Figure 6-9 provide the renewable penetration level and corresponding inertia in Alberta and the whole system for all cases by replacing generators in the Alberta area only. The systemwide renewable penetration level increased to 13% while renewable penetration level in Alberta increased to 96%. The total decrease in inertia was around 60 GW-s.

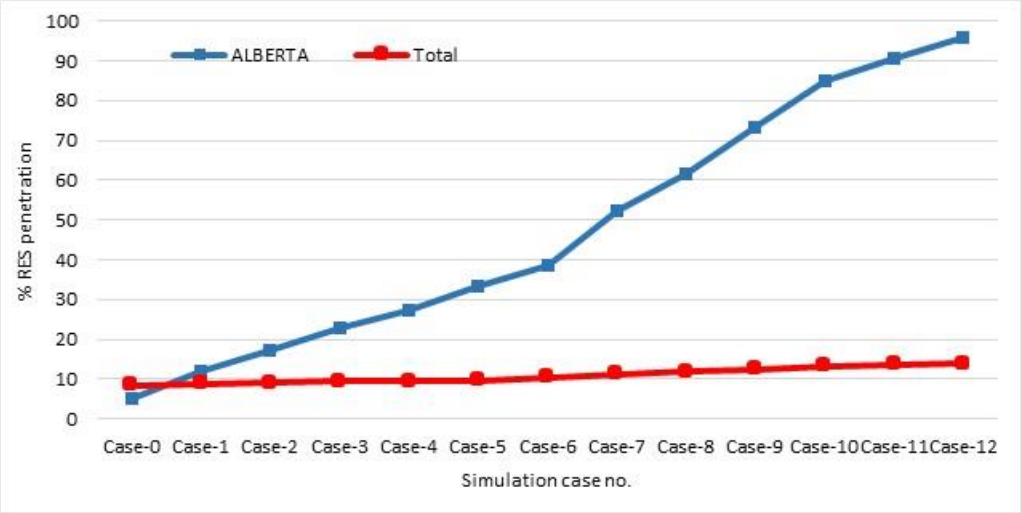

Figure 6-8. Percent renewable penetration level in Alberta and the whole system for different cases in Scenario S3.

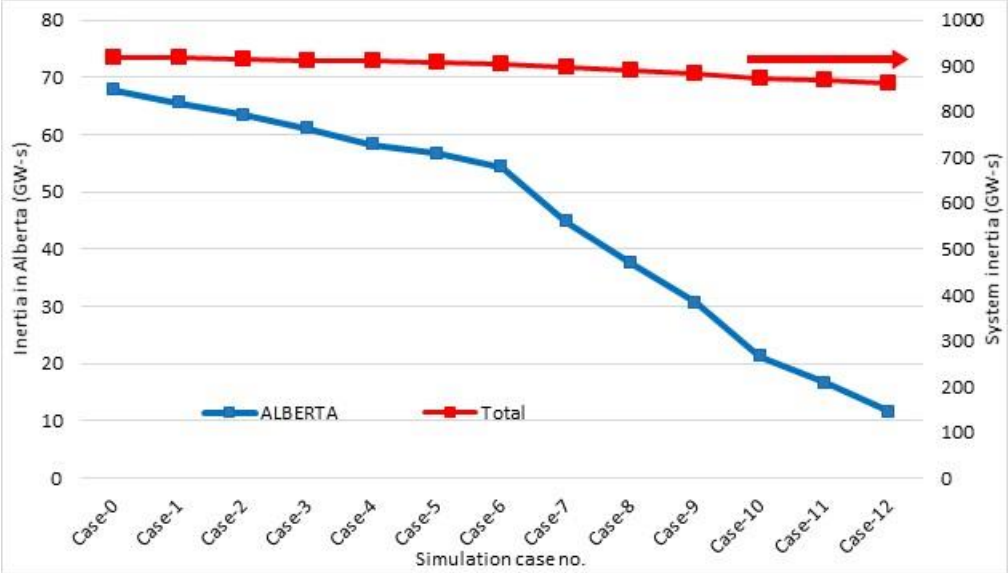

Figure 6-9. Inertia in Alberta area and throughout the system for different cases in Scenario S3.

6.2.4 Increase in RES Penetration Systemwide Except in Alberta – Scenario S4

In this scenario, RES penetration was increased systemwide across all areas except Alberta. This scenario was analyzed to understand how the system modes would be affected if the generators in all other areas are replaced except Alberta, which has generators with high participation factors for both NS-A and NS-B modes. The group of generators replaced in this scenario is the same as that in Scenario 1 and in the same order for the additional 12 cases, the difference being the generators were not replaced in Alberta in this scenario. Figure 6-10 and Figure 6-11 provide information on renewable penetration level and corresponding inertia in several areas and throughout the system for all cases. The systemwide renewable penetration level increased from 8% to 64% and inertia decreased from 919 GW-s to 369 GW-s in the final case (Case-12).

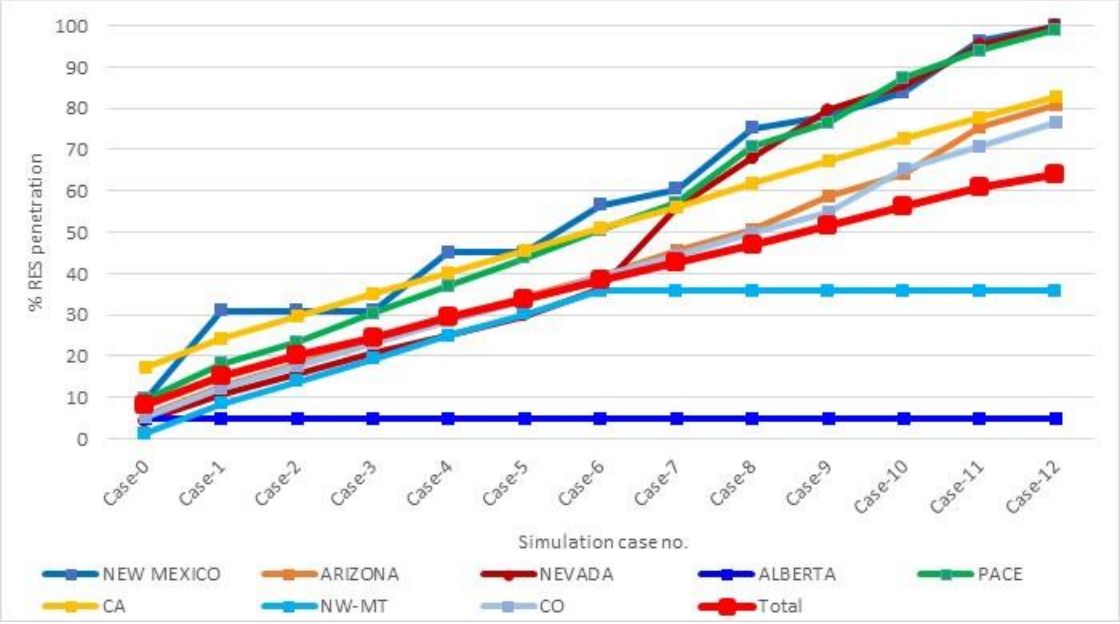

Figure 6-10. Percent RES penetration in several areas and throughout the system for the different cases in Scenario S4.

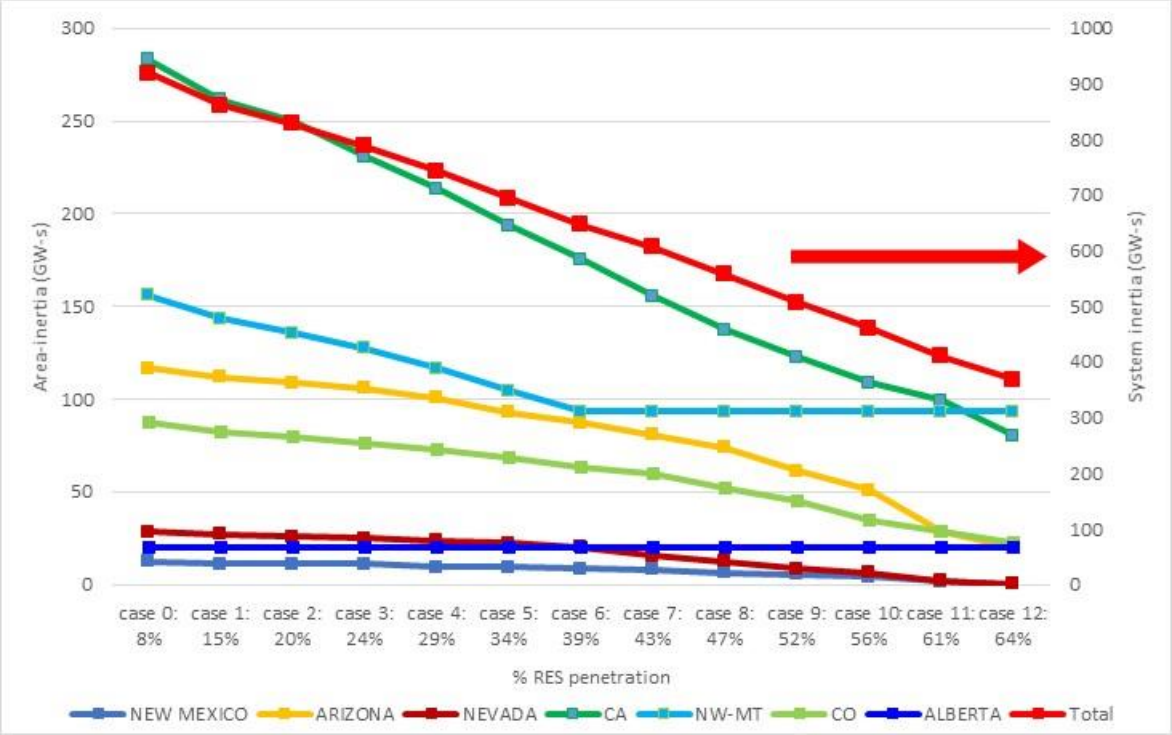

Figure 6-11. Area-wise and total system inertia as a function of percent RES penetration for the different cases in Scenario S4.

6.2.5 Change in the Power-flow from North to South – Scenario S5

Based on experience with historical data, power flow from north to south, which includes PDCI and COI, has a significant impact on north-south modes. As shown in Figure 6-12, flow from north to south changes significantly throughout the year. This can be more pronounced with increased RES penetration in the south. As the RES penetration level increases, especially in California, the system will see lower flow from north to south. The RES generation was increased by increasing power output of existing online generators to increase their capacity factor and further by bringing offline RES-based generation online in California. The corresponding increase in the system generation was then balanced by decreasing the generation in the Northwest, Alberta, and B.C., which was done by scaling down dispatch of each generator in these areas. In this scenario, system inertia remained constant for all cases as no synchronous generator was brought online or taken offline. Figure 6-13 shows the flow from north to south (sum of PDCI and COI flow) for different cases along with the corresponding increased RES generation in California. As seen in Figure 6-13, the flow from north to south in the base case was 6100 MW, which was reduced to -2115 MW (flow direction reversed) for Case-7.

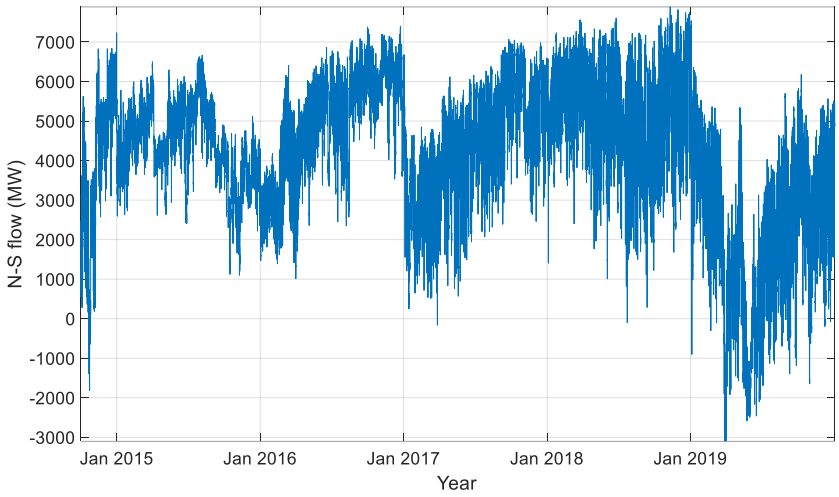

Figure 6-12. Historical power flow from north to south (data source: bpa.gov, available online at https://transmission.bpa.gov/Business/Operations/Paths/).

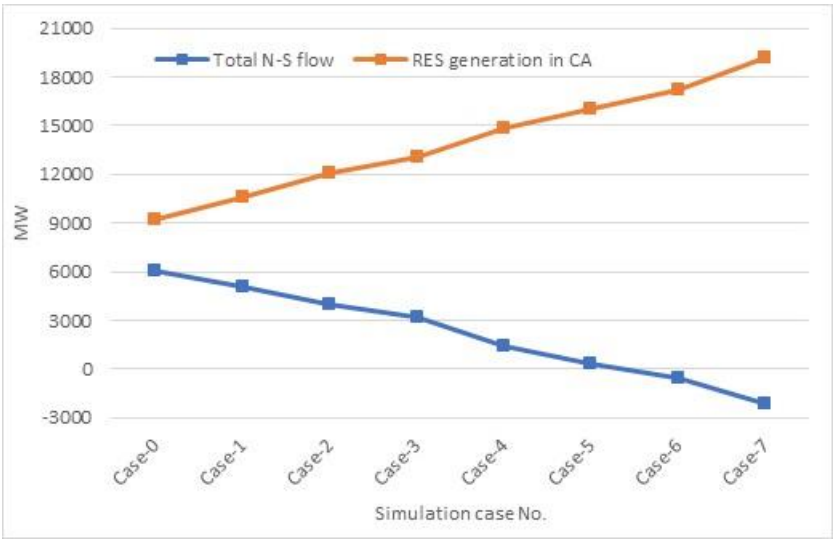

Figure 6-13. Decrease in power flow from north to south caused by increased RES generation in California in Scenario S5.

6.3 Methodology

For each scenario described in the previous subsection, oscillation assessment was carried out to identify the trends observed in the system modes for different renewable penetration levels. This subsection will provide a description of methodology used for this analysis.

6.3.1 Modal Analysis

System oscillatory behavior is determined by system modes, which are given by eigenvalues of system state matrix,

$$\lambda_i = \sigma_i + j\omega_i \tag{6-1}$$

where σ_i represents damping coefficient and ω_i denotes frequency (in rad/sec) of the i^{th} system mode. Damping ratio, ζ_i, given by

$$\zeta_i = \frac{-\sigma_i}{\sqrt{\sigma_i^2 + \omega_i^2}} \tag{6-2}$$

provides a measure of the small-signal stability margin of a system. These mode estimates can be obtained by using either a model-based or measurement-based approach. For a large system, a model-based approach can be computationally exhaustive; therefore, a measurement-based approach was used for this analysis to estimate system modes. Measurements required for modal analysis were obtained by running dynamic simulations with a transient event to excite system modes. Generator rotor-angle at several buses from all areas were selected to calculate deviations in frequency measurements (Hz) by taking time-difference of the rotor-angle measurements as follows:

$$\Delta f_i = \frac{\theta_{i+1} - \theta_i}{2\pi\Delta T} \tag{6-3}$$

where ΔT is the sampling rate of the measurements and θ_i is the generator rotor-angle measured at i^{th} time instant. These calculated frequency-deviation measurements were then used for modal analysis. Figure 6-14 shows one such example of frequency-deviation measurements represented by ringdown oscillations used for modal analysis.

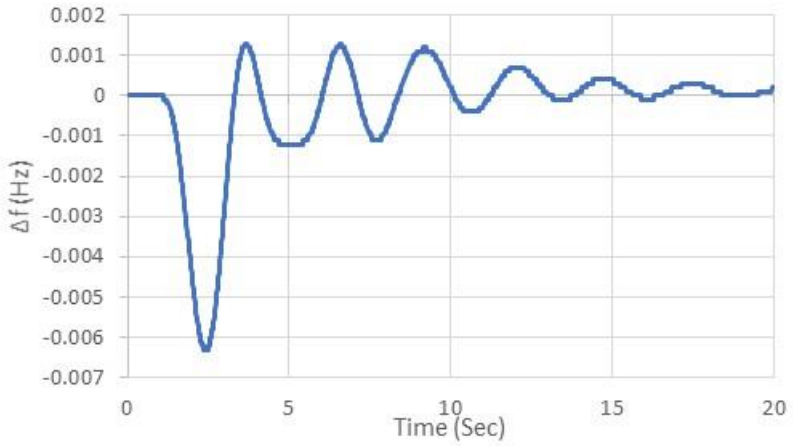

Figure 6-14. Frequency-deviation measurements represented by ringdown oscillation.

Signal Preprocessing

In power systems, the frequency of system modes lies between 0.1 to 2 Hz. Therefore, for modal analysis, the signals are preprocessed to extract signal content in this frequency range (Pierre, Trudnowski and Donnelly 1997). The signal is first filtered through a low-pass filter and then down-sampled to obtain a sampling rate of five samples per second. The decimated signal is then filtered through a high-pass filter to remove content at frequency ranges lower than 0.1 Hz. This preprocessed signal is then used for modal analysis.

Estimation of System Modes and Mode Shapes

In this report, system modes were estimated using the multichannel Prony method, the details of which can be found in (Trudnowski, Johnson and Hauer 1999). Frequency measurements from multiple channels were used simultaneously to obtain system mode estimates. Once system modes were estimated, the shapes of these modes were estimated to identify the set of generators oscillating against each other using the approach described in (Hauer, Demeure and Scharf 1990).

Validation of Mode Estimates and Selection of Model Order

As described in (Agrawal and Pierre 2019), estimating system modes is not enough until these estimates are also validated. The mode estimates obtained using the multichannel Prony method were validated by comparing the pre-processed signal with the signal reconstructed using mode estimates. Based on the validation of mode estimates, model order was selected for estimating system modes. An example of model order selection by validating mode estimates is shown in Figure 6-15. In this example, model order = 26 was selected for estimating system modes.

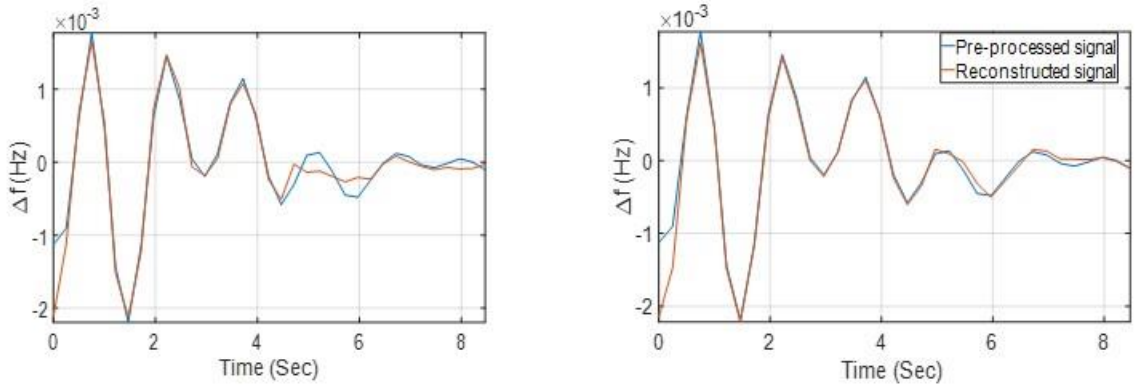

Figure 6-15. Validation of mode estimates by comparing pre-processed signal with reconstructed signal. Model order = 22 (left) and model order (selected) = 26 (right).

6.3.2 Event Selection for Dynamic Simulation

The WI has several well-studied system modes as discussed in previous sections. Each of these modes has their own unique characteristics of frequency and mode shapes as provided in Table 4-1. The other two features of significance to understanding these modes are controllability and excitability. Controllability provides information on generator/location, which has control over these modes. Excitability provides information on the contingencies that excite a mode. Excitability is related to controllability in a way that a transient event taking place at a location having high controllability of a mode will result in a higher degree of excitability of that specific mode. As the analysis performed in this report focusses on NS -A and NS-B, several location-based transient events were investigated to identify an event that adequately excited these two modes and resulted in high observability across the WI. The following location-based events were analyzed.

6.3.2.1 Chief-Joseph Brake Insertion

In this transient event, a 1400 MW resistor brake was inserted at the Chief-Joseph substation in the Northwest for 0.1 second. The estimates of NS-A and NS-B and their shapes are shown in Figure 6-16.

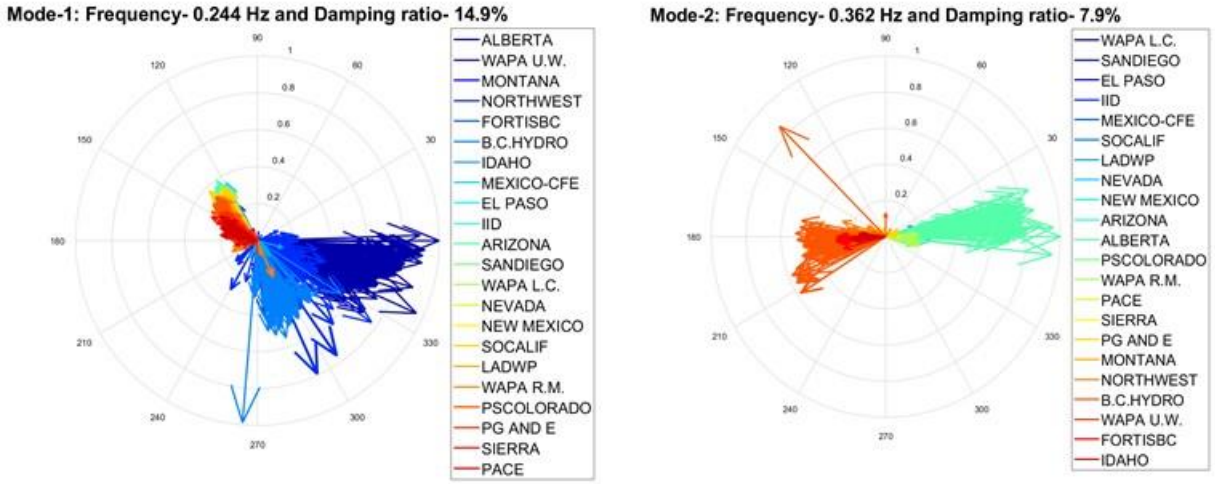

Figure 6-16. Estimates of NS-A and NS-B modes and their shapes for Chief Joseph brake insertion event.

6.3.2.2 Alberta Brake Insertion

In this transient event, like the Chief-Joe brake insertion, a fictitious 1400 MW resistor brake was inserted at the Genesee plant substation for 0.1 second. Figure 6-17 provides NS-A and NS-B estimates along with estimates of their shapes. In Figure 6-17, mode shapes for all generators in each area are plotted with the same color. This helped to analyze generators in different areas oscillating against each other. The legend

corresponds to the areas in the WECC use case and these entries are ordered according to the average of the estimated initial-phase angle of the mode for all generators in each area.

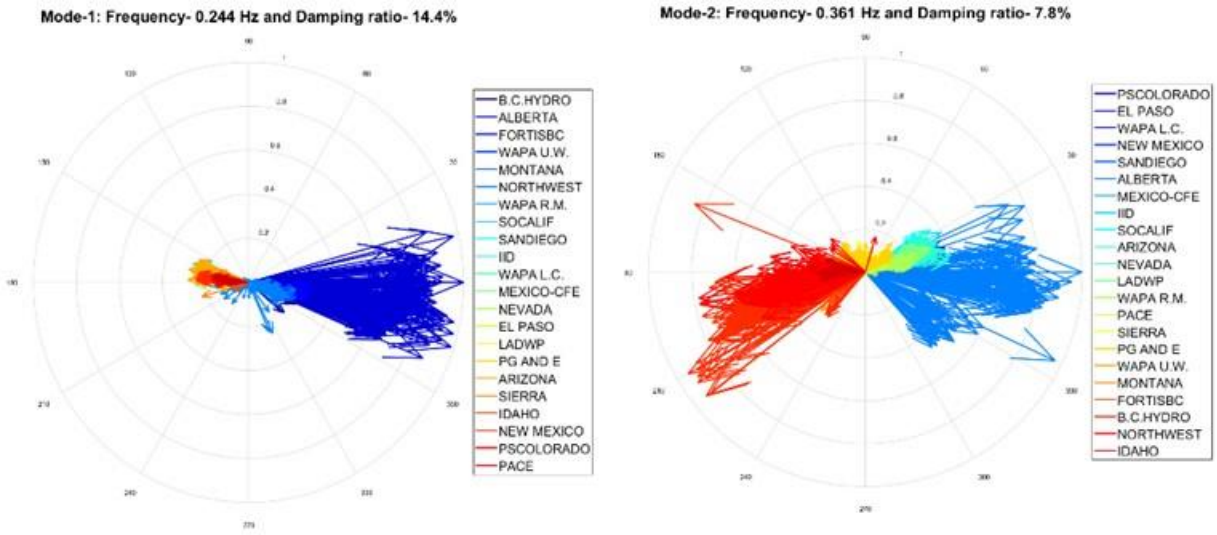

Figure 6-17. Estimates of NS-A and NS-B modes and their shapes for the Alberta brake insertion event.

6.3.2.3 Other events

The other two events that were investigated are fictitious 1400 MW resistor-brake insertion in the Pacific Corporation (PACE) and Los Angeles areas. The events in this location did not significantly excite NS-A and NS-B, and therefore mode shape plots are not included.

After analyzing NS-A and NS-B observability across the WI for these events using mode shape plots, the Chief-Joe brake insertion event was selected for further analysis.

6.4 Results and Discussion

The PowerWorld simulator was used to perform simulations for all scenarios (PowerWorld Simulator 2020). For each case in each simulation scenario, selected synchronous machines were replaced by type-4 machine, exciter, and governor model. The parameters of these models were chosen from the existing type-4 generator models in the 2018 HS WECC operating case. The Chief Joseph brake insertion event was used as a transient event to excite system modes. Frequency measurements calculated from rotor-angle measurements of generators from all areas were used for estimating system modes using the multichannel Prony method. The estimated modes were then validated by comparing the preprocessed signal with the signal reconstructed using mode estimates. Results obtained for several scenarios are discussed next for NS-A and NS-B modes.

6.4.1 Oscillation Assessment of NS-A for Scenarios S1–S4

Figure 6-18 and Figure **6-19** show and compare the results obtained for Scenarios S1–S4 for analyzing the impact of increased renewable penetration level on the frequency and damping ratio of NS-A.

Frequency of NS-A. As seen in Figure 6-18, the frequency of NS-A increased for all four scenarios with the increase in renewable penetration level and subsequent reduced system inertia. Comparing frequency estimates for Scenarios S1 and S2, it was observed that the trends observed in the frequency of the NS-A with respect to the increased renewable penetration level were affected by reversing the order of the group of generators that were replaced. Comparing results obtained for Scenarios S3 and S4, it can be seen that the increase in the frequency of NS-A was a little higher in Scenario S3 (mode frequency increased from 0.244 to 0.302 Hz) than Scenario S4 (mode frequency increased from 0.244 to 0.286 Hz), even with a much lower change in system inertia. Just to recall, in Scenario 3, generators were replaced only in Alberta and in Scenario S4 generators were replaced in all areas except Alberta.

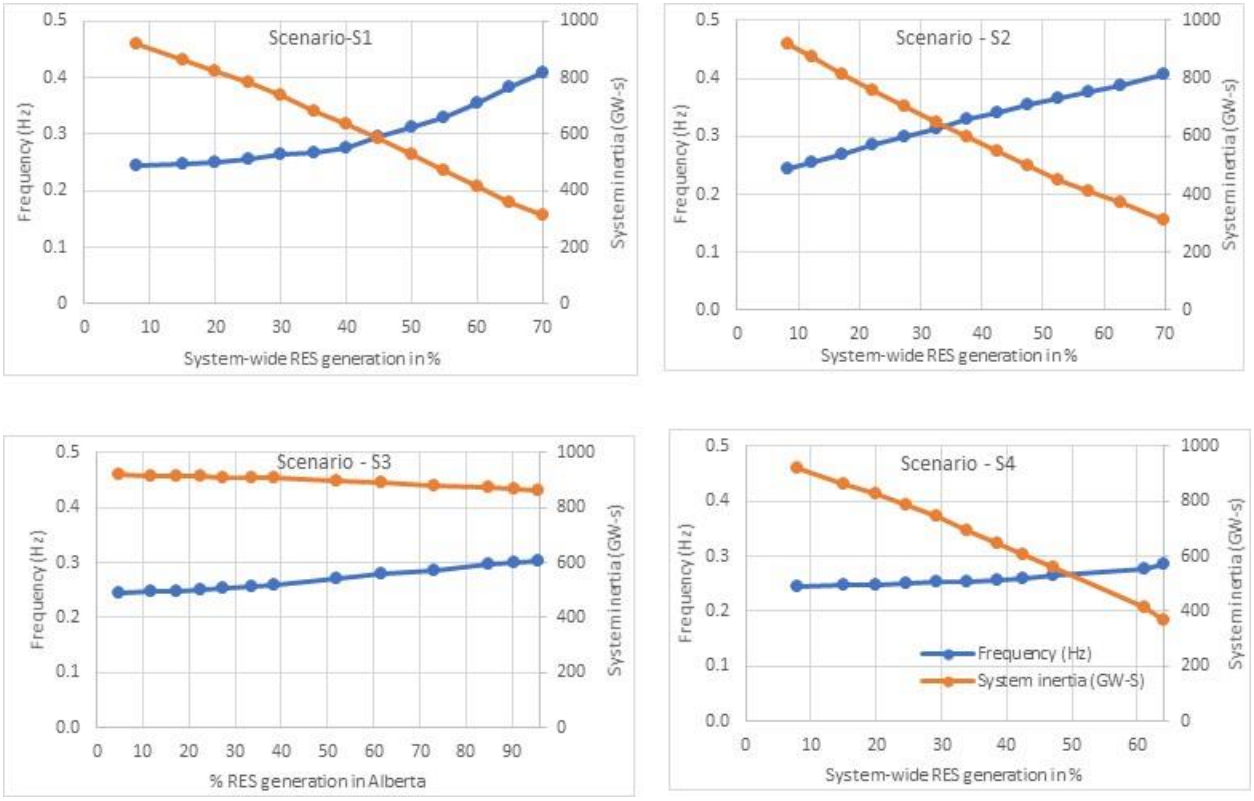

Figure 6-18. Assessment of the impact of increased renewable penetration on the frequency of NS-A for Scenarios S1 (top left), S2 (top right), S3 (bottom left), and S4 (bottom right).

Damping ratio of NS-A. Figure **6-19** shows the impact of increased renewable penetration on the damping ratio of NS-A for Scenarios S1–S4. In Scenario S1, the damping ratio of NS-A initially

increased slightly and, after the systemwide renewable penetration further increased beyond 40%, damping ratio declined sharply. From this result, it could be concluded that the increase of penetration level beyond a certain value can result in a significant decrease in the damping ratio of system modes. Therefore, analysis was carried out with Scenario 2 in which the order of generators replaced in Scenario S1 was reversed. Comparing results for Scenarios S1 and S2 shows that the trends observed in the damping ratio of the NS-A reversed when the order of generators replaced was reversed. This is strong evidence that the change in the damping ratio is not a function of increased renewable penetration level or reduced system inertia, but is determined by the generators that are replaced and how remaining synchronous generators interact among each other.

This conclusion was further substantiated by the results obtained for Scenarios S3 and S4. As mentioned earlier, generators in Alberta have the highest participation factors for NS-A, while generators in other areas have much lower participation factors. Therefore, analysis was done to assess the impact of increased renewable penetration level in Alberta only (Scenario S3) and increased renewable penetration level in all areas except Alberta (Scenario S4) to determine how the participation factor of replaced generators affects system modes, particularly damping ratio. Comparing results for Scenarios S1 and S3 shows that the trends observed in these two scenarios closely resemble each other, which indicates the trends in damping ratio of NS-A for Scenario S1 were highly influenced by replacing generators in Alberta. This is also further illustrated by results for Scenario S4, where it can be seen that replacing generators in all areas except Alberta resulted in a small increase of the damping ratio of NS-A and not a decrease.

From this set of results for NS-A, it can be concluded that the change in the frequency and damping ratio of modes cannot be directly related to the change in the system inertia or increased renewable penetration level. Other factors also need to be considered, such as participation factor of generators that are replaced, topology of the online synchronous generators, etc. A detailed eigenvalue analysis was carried out to have a better understanding of the trends observed in the NS-A with increased renewable penetration level.

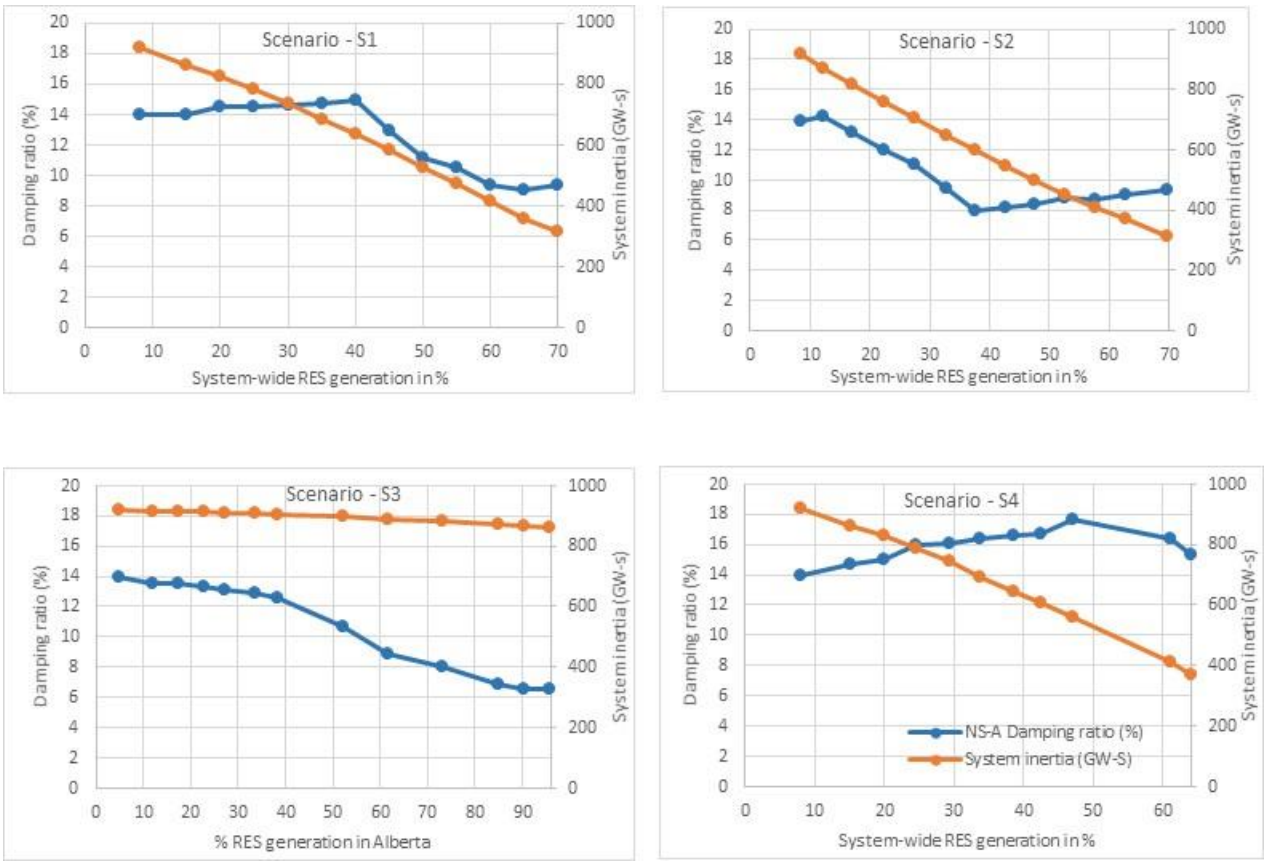

Figure 6-19**.** Assessment of the impact of increased renewable penetration on the damping ratio of NS-A for Scenarios S1 (top left), S2 (top right), S3 (bottom left), and S4 (bottom right).

6.4.2 Oscillation Assessment of NS-B for Scenarios S1–S4

Figure 6-20 and Figure 6-21 show the results obtained for simulation Scenarios S1 to S4 for analyzing the impact of increased renewable penetration level on the frequency and damping ratio of NS-B.

Frequency of NS-B. As seen in Figure 6-20, the trends observed in the frequency of NS-B with systemwide increase in renewable penetration level changed by reversing the order in which synchronous generators were replaced. Also, similar to the NS-A, changes observed in the frequency of NS-A were higher for Scenario S3 in which generators were replaced only in Alberta as compared to Scenario S4 in which generators were replaced in all areas except Alberta.

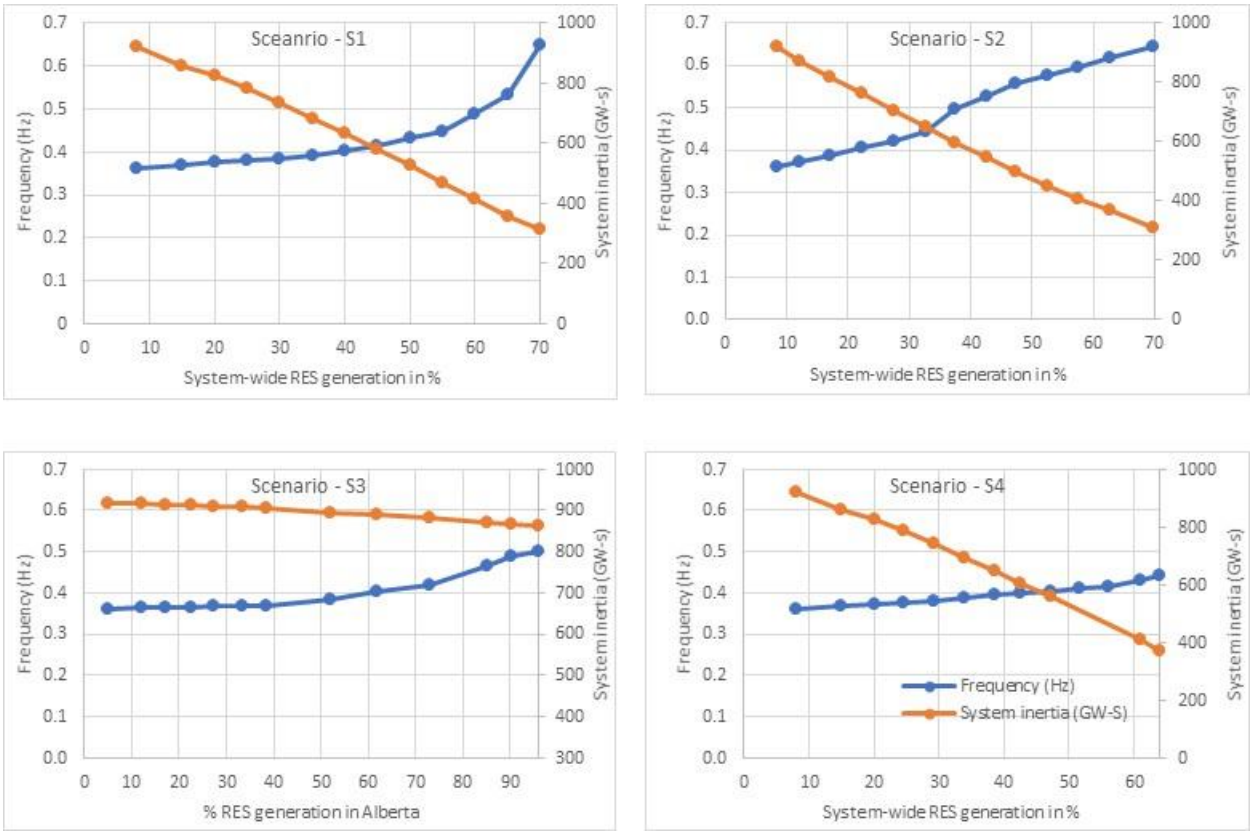

Figure 6-20. Assessment of the impact of increased renewable penetration on the frequency of NS-B for Scenarios S1 (top left), S2 (top right), S3 (bottom left), and S4 (bottom right).

Damping ratio of NS-B. As seen in Figure 6-21, the damping ratio of NS-B was not as affected by the increased renewable penetration level as NS-A for all four scenarios. Except some cases in Scenario 2 and Case-12 in Scenario S3, the damping ratio of NS-B in all other cases and scenarios were comparable to that in the base case. A detailed eigenvalue analysis was carried out to have a better understanding of the trends observed in NS-B with increased renewable penetration level.

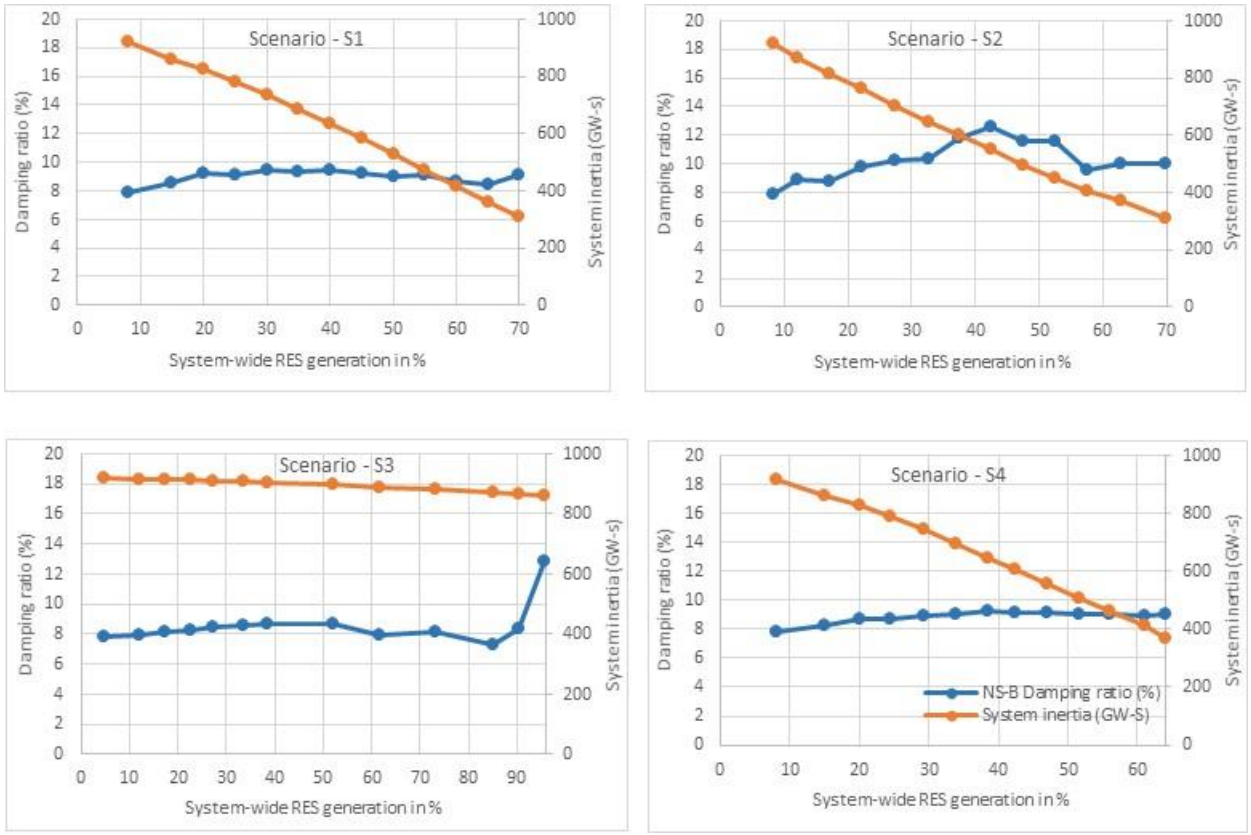

Figure 6-21. Assessment of the impact of increased renewable penetration on the damping ratio of NS-B for Scenarios S1 (top left), S2 (top right), S3 (bottom left), S4 (bottom right).

6.4.3 Oscillation Assessment for Scenario – S5

Figure 6-22 and Figure 6-23 provide results for the impact of changes in power flow from north to south through PDCI and COI lines on NS-A and NS-B. As seen in these figures, north-to-south flow had minimal impact on NS-B with respect to both frequency and damping ratio. However, a change in north-to-south flow have a significant impact on both frequency and damping ratio of NS-A as shown in Figure 6-22 and Figure 6-23. These results show that as the flow decreased from north to south, the damping ratio of NS-A increased significantly and became less dominant. The damping ratio of NS-A does not change much after the direction of flow was reversed from south to north. Also, the frequency of NS-A decreased with the decrease in the north-to-south flow and did not change much after the direction of flow

was reversed from south to north. The mode shape estimates of NS-A and NS-B obtained for Case-7 is shown in Figure 6-24.

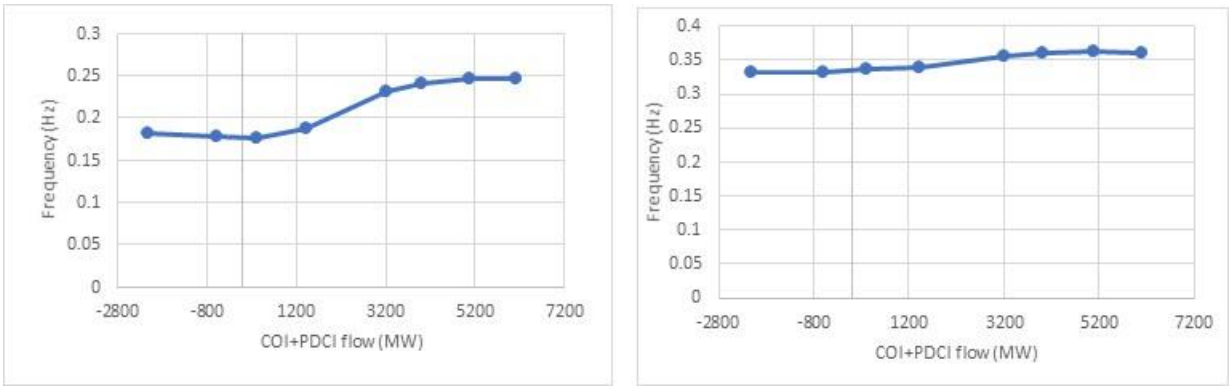

Figure 6-22. Impact of change in power flow from north to south (COI and PDCI combined) on frequency of NS-A (left) and NS-B (right).

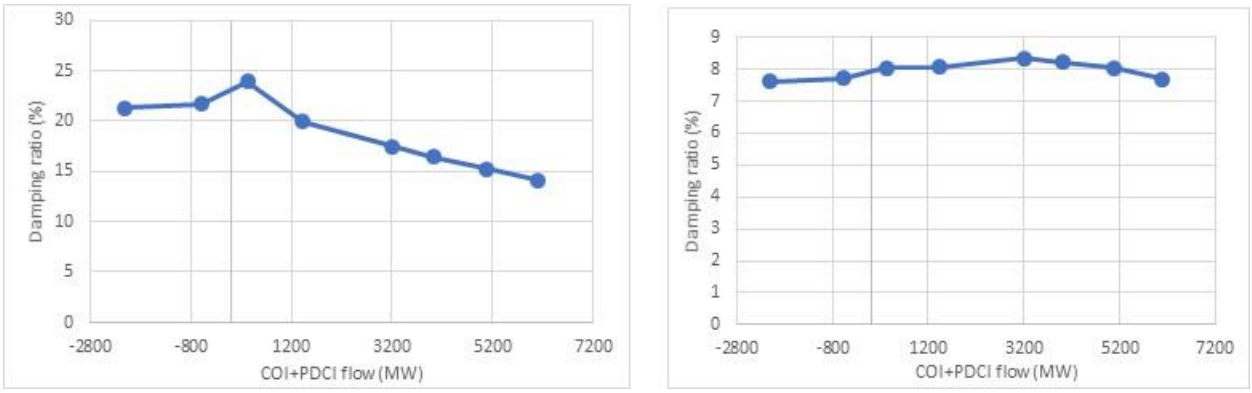

Figure 6-23. Impact of change in power flow from north to south (COI and PDCI combined) on DR of NS-A (left) and NS-B (right).

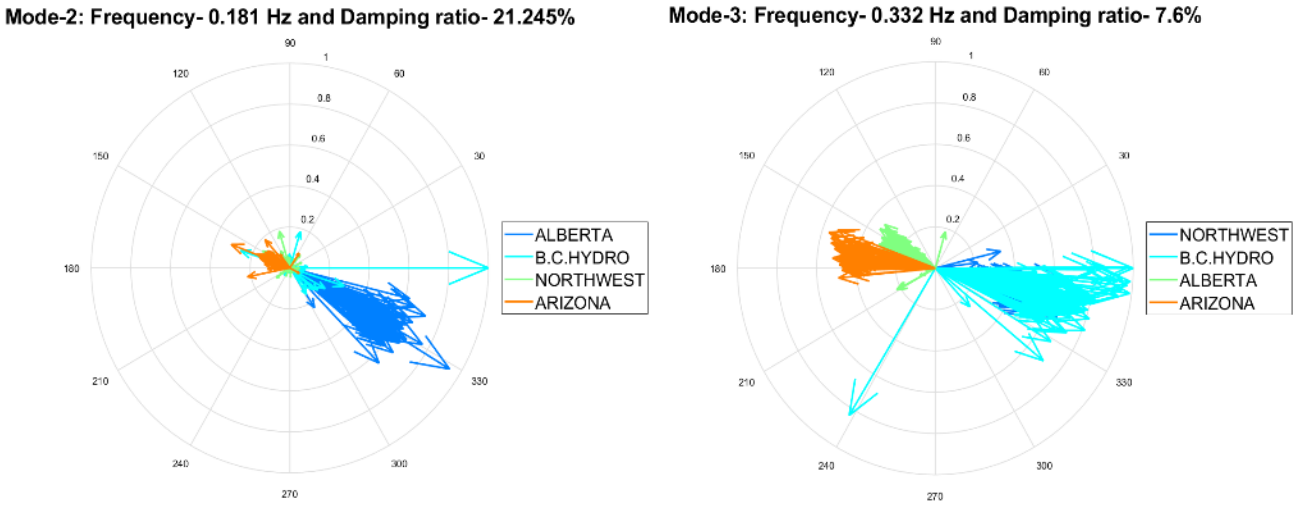

Figure 6-24. Estimates of mode shape of NS-A (left) and NS-B (right) for case 7.

6.5 Detailed Eigenvalue Analysis Using SSAT

As discussed in earlier sections, several scenarios were analyzed to assess the impact of increased renewable penetration on NS-A and NS-B. From this analysis, it was concluded that the trends observed in these modes were not directly related to the increased renewable penetration level or reduced system inertia but were highly influenced by the generators that were replaced. To have a better understanding of these trends, a detailed eigenvalue analysis was carried out for Scenarios S1–S4 using SSAT and shown in Figure 6-25. In this analysis, participation factor and mode shape of synchronous generators were compared for all cases.

6.5.1 Systemwide Increase of RES Penetration Level – Scenario S1

Figure 6-25 shows the actual frequency and damping ratio of NS-A and NS-B obtained using SSAT and compares these values with the corresponding estimates obtained using Prony method. The good match between these values validates our results discussed in Section 6.4. Using SSAT, participation factor and mode shapes of generators were obtained for all cases for NS-A and NS-B.

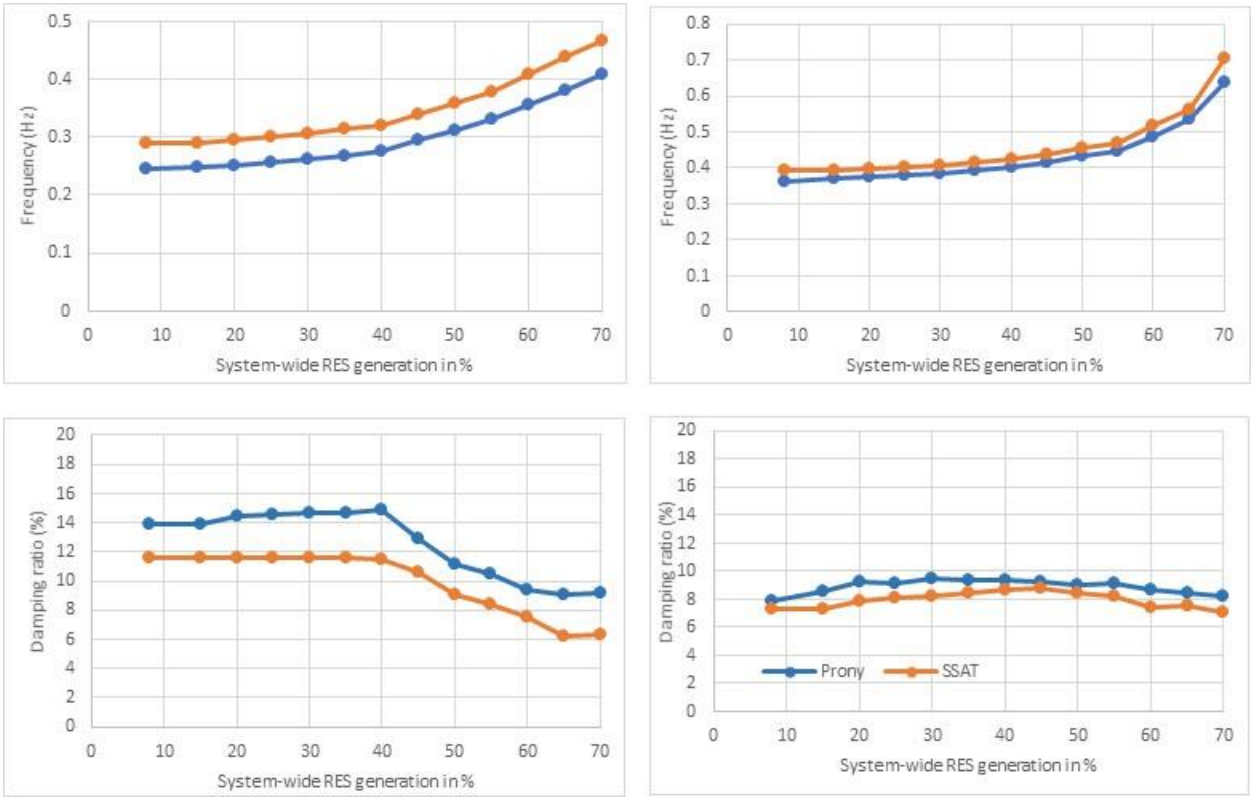

Figure 6-25. Comparison of the actual frequency and damping ratio of NS-A (left) and NS-B (right) obtained using SSAT and mode estimates obtained using the Prony method.

6.5.1.1 Eigenvalue Analysis of NS-A

Figure 6-26 and Figure 6-27 show the variations observed in the mode shape and participation factor of generators in several areas with increased renewable penetration. In Figure 6-27, the participation factor of only those generators is included that had a value of at least 0.05 in the base case. Also in this figure, the missing part of the line represents generators that were replaced in the earlier cases.

As seen in Figure 6-26, the mode shape for NS-A remained unchanged with increased renewable penetration level. By analyzing participation factor of generators for all cases in Figure 6-27, it was found that the trends observed in NS-A for Scenario S1 could be explained with respect to the participation factor of generators. As shown in Figure 6-28, the participation factor of generators for cases 0–6 did not change much even when the systemwide renewable penetration level increased to 40% in Case-6. The same trend was also observed in the damping ratio of NS-A, which did not change much for these cases. From Case-6 onward, the participation factor of generators changed significantly as shown in Figure 6-29, which is exactly what was observed in the damping ratio.

The participation factor of the remaining synchronous generators in Alberta increased up to Case-9, after which it started decreasing. In Case-12, the remaining synchronous generators in Alberta had low participation factor. The participation factor of generators in B.C. Hydro area increased up to Case-10 and then it started decreasing. It should be recalled here the renewable penetration level in this area could only be increased up to 8% and therefore generators were only replaced in cases 1 and 2. The participation factor of generators increased in all other area, including California, Arizona, and others with the increased renewable penetration level with Palo Verde units in Arizona becoming the ones with the highest participation factor from Case-10 onward. The participation factor of generators in Montana and the Northwest had low participation factor for all generators in all cases as shown in Figure 6-30. The participation factor of some Grand Coulee units increased slightly up to Case-10 and then decreased, while the Boundary gate unit increased for all cases.

One important thing to note in this analysis is that only qualitative inference can be made using eigenvalue analysis and not quantitative. The quantity by which the damping ratio of the mode changes will be determined by the overall interaction among generations in the system based on their participation factors.

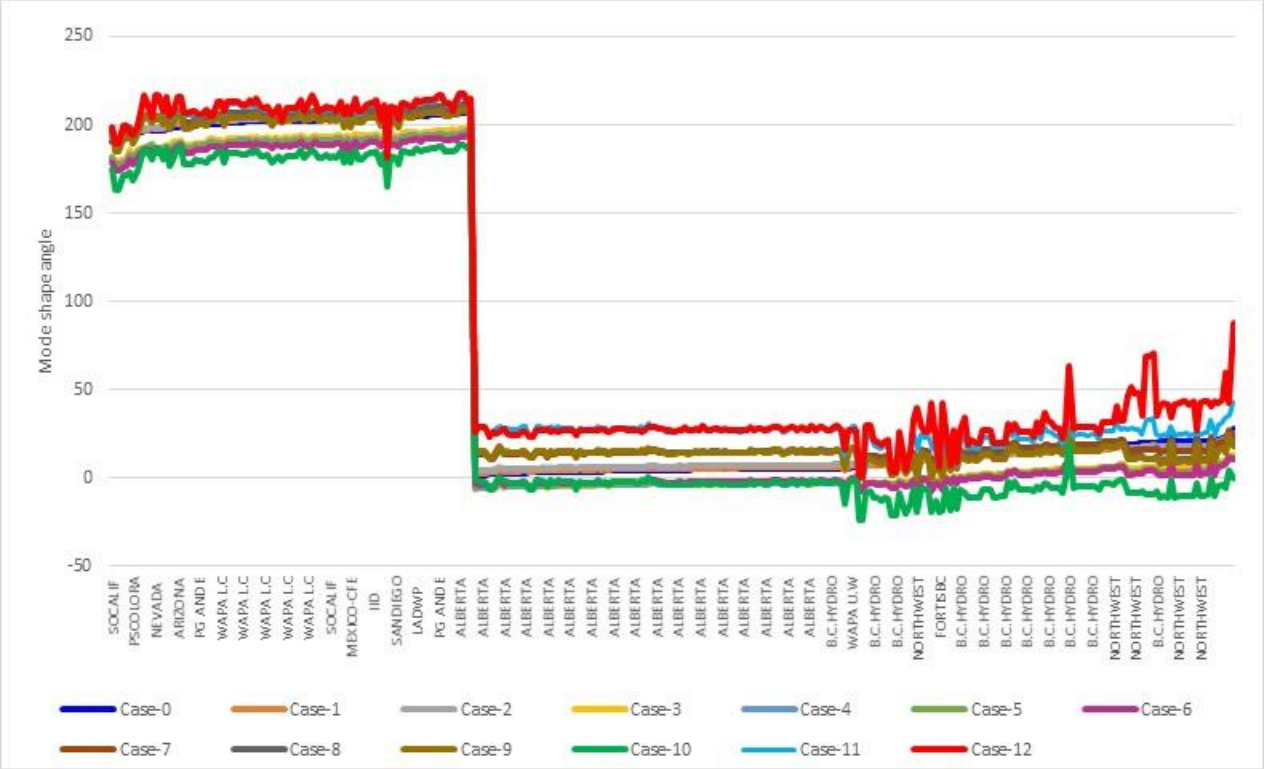

Figure 6-26. Comparison of mode shape of generators for all cases of Scenario S1 for NS-A.

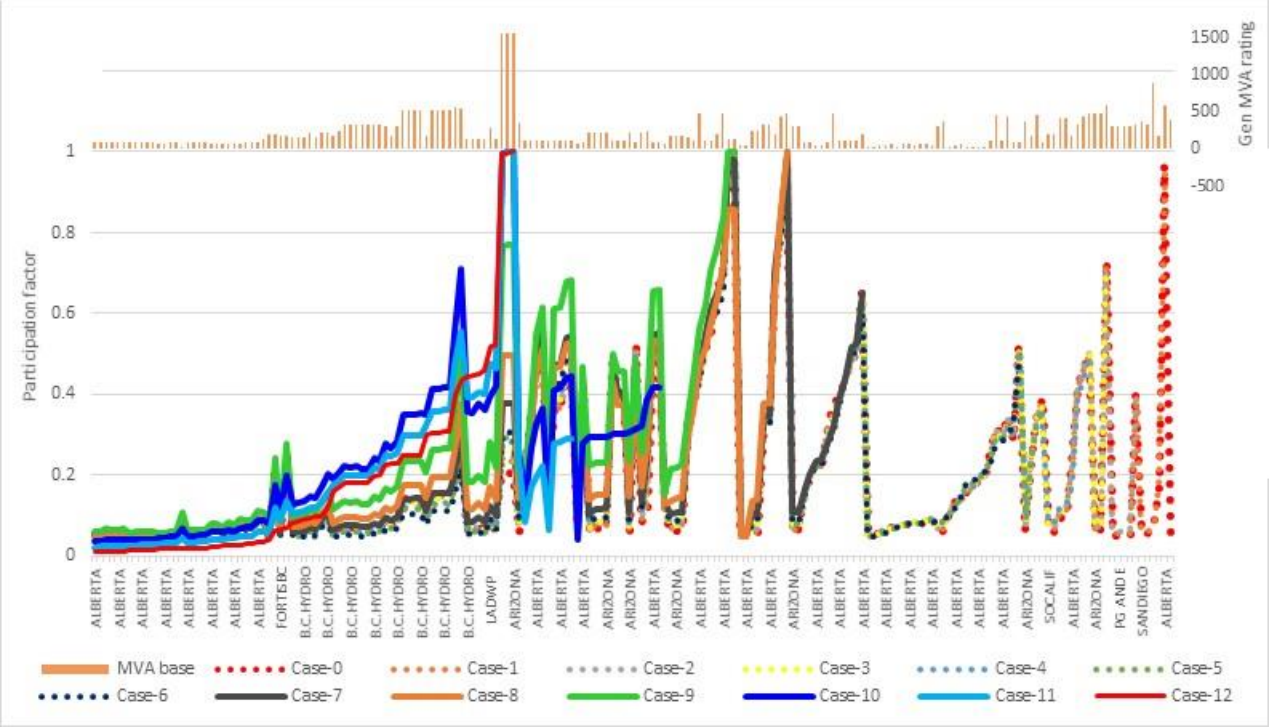

Figure 6-27. Participation factor of generators for all cases of Scenario S1 for NS-A.

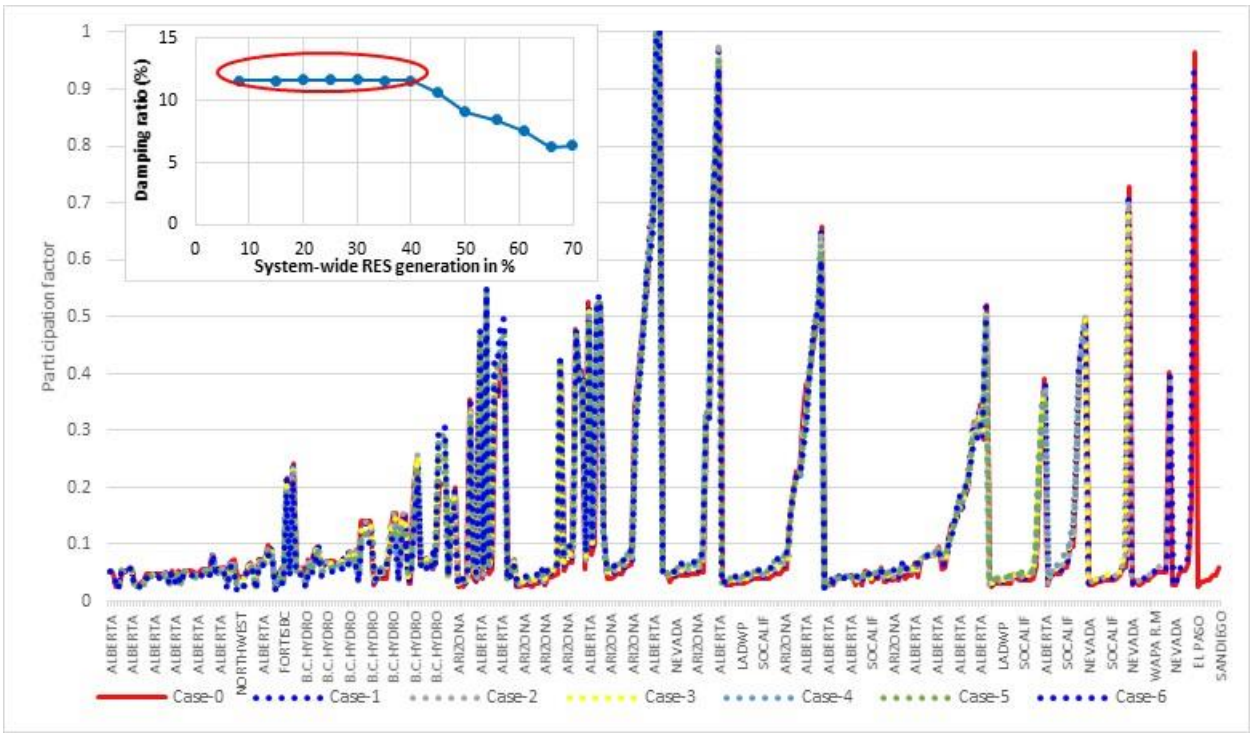

Figure 6-28. Participation factor of generators for cases 0–6 of Scenario S1 for NS-A.

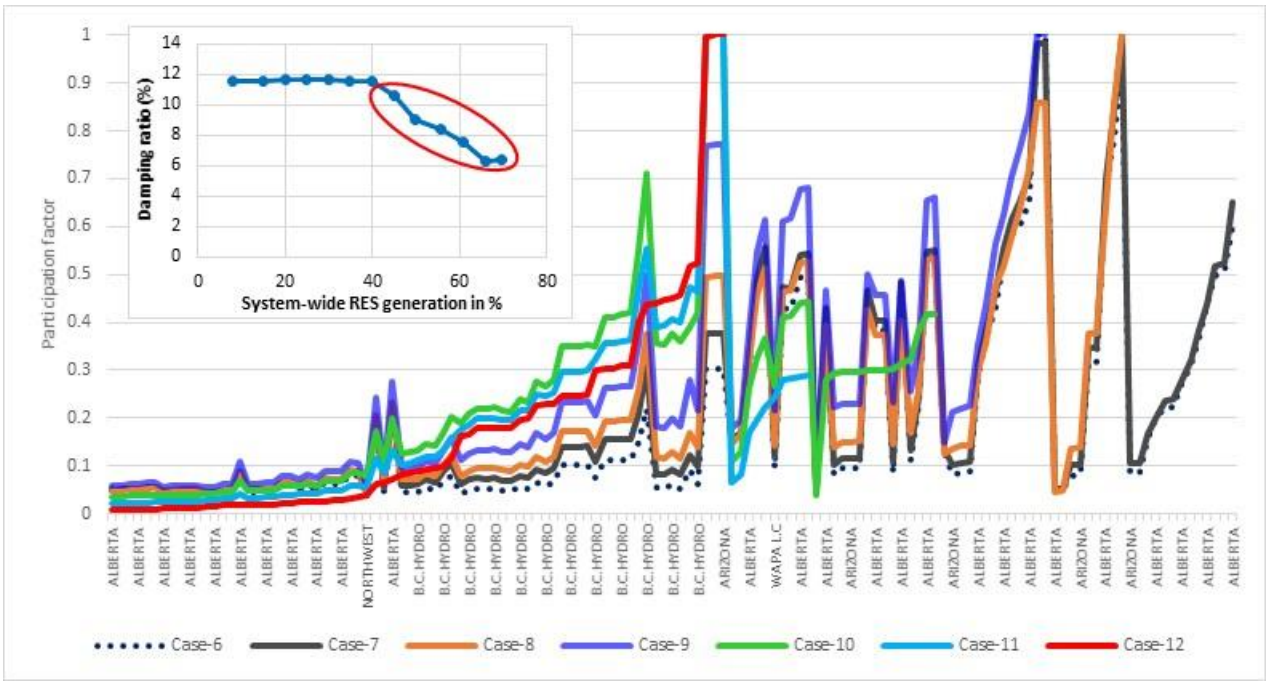

Figure 6-29. Participation factor of generators for cases 6–12 of Scenario S1 for NS-A.

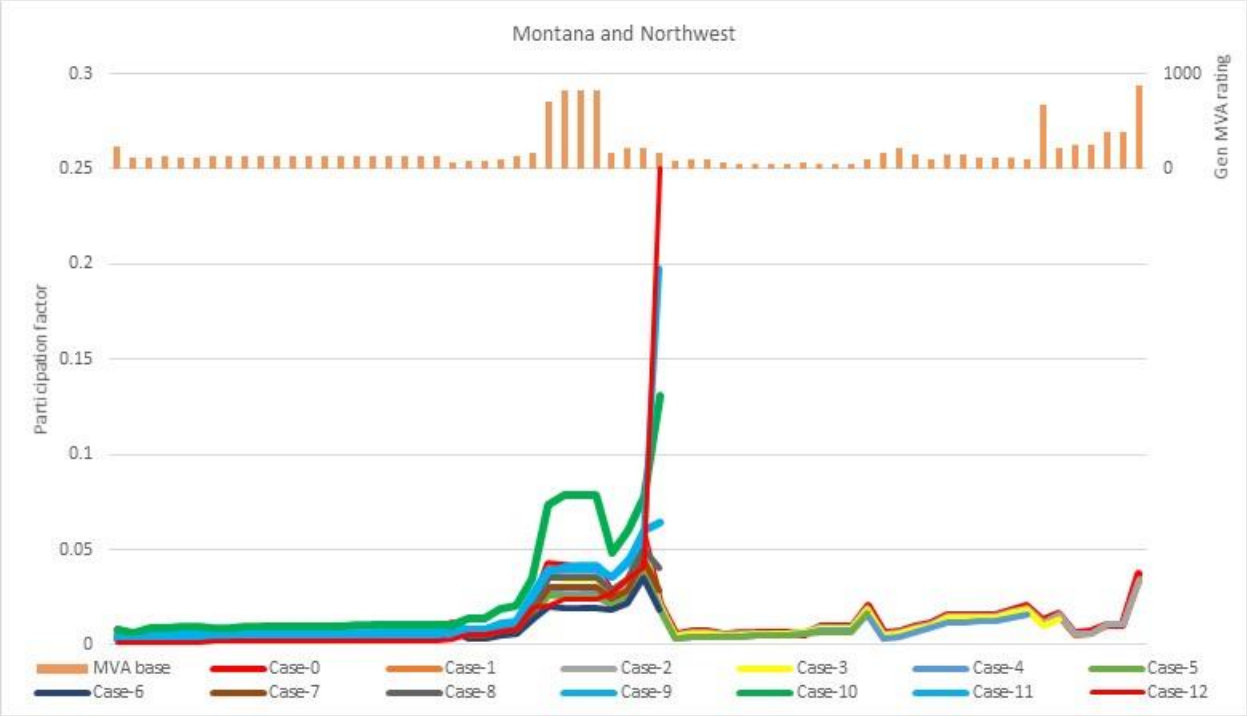

Figure 6-30. Participation factor of generators in Montana and the Northwest for all cases in Scenario S1 for NS-A.

6.5.1.2 Eigenvalue Analysis of NS-B

Figure 6-31 and Figure 6-32 show the variations observed in the mode shape and participation factor of generators with increased renewable penetration for NS-B. In Figure 6-32, participation factor of only those generators included that had a value of at least 0.1 in the base case.

As shown in Figure 6-31, the mode shape for NS-B remained unchanged with increased renewable penetration level until Case-10. From Case-11 onward, some of the generators in B.C. Hydro started to oscillate with Alberta and other generators in the South against generators in the North, which explains the change in the trend observed in the damping ratio of NS-B for cases 11 and 12. As shown in Figure 6-32, the participation factor of generators did not change much from cases 0–6 except some generators in B.C. Hydro and Alberta. The general trend observed was that the participation factor of generators increased slightly in B.C. Hydro while in Alberta it decreased. As shown in Figure 6-32, these trends reverse from Case-7 onward with participation factor of generators in B.C. Hydro decreasing significantly and that in Alberta increasing significantly until Case-12. This explains the change in trends observed in the damping ratio of NS-B from Case-7 onward. The damping ratio initially increases slightly from Case-0 until Case-6 and then starts decreasing from Case-8 onward. The participation factor of generators in

other areas decreased until Case-11 and then after the change in the mode shape of some generators in B.C. Hydro, the participation factor increased in Case-12.

With eigenvalue analysis, the trends observed in the damping ratio of NS-B could be explained to some extent by the variations observed in the mode shape and participation factor of synchronous generators in the system.

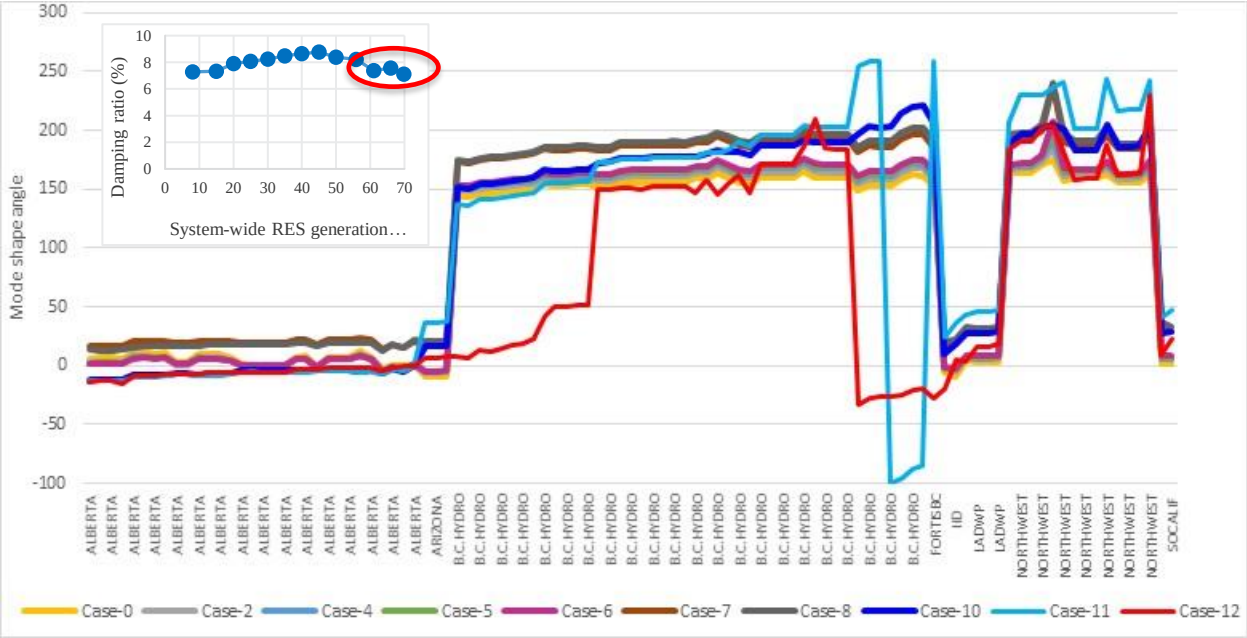

Figure 6-31. Comparison of mode shape of generators in several areas for selected cases of Scenario S1 for NS-B.

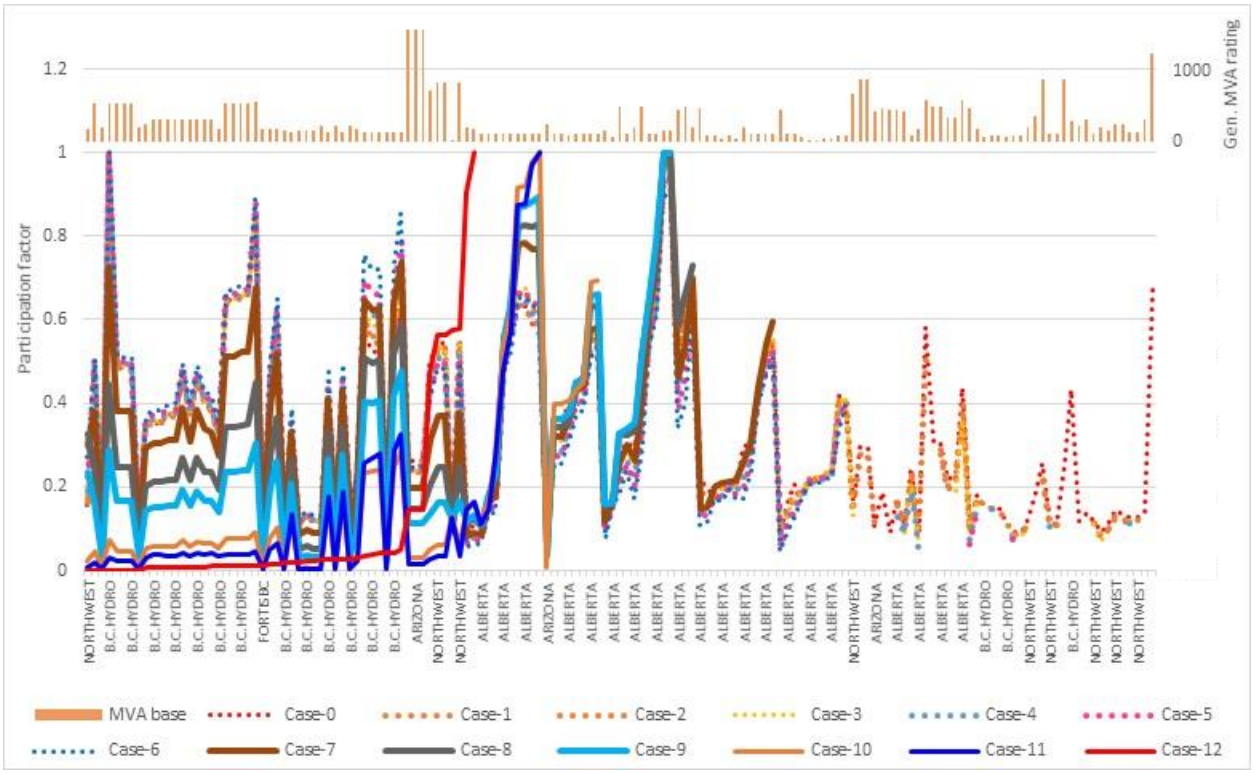

Figure 6-32. Participation factor of generators in several areas for all cases of Scenario S1 for NS-B.

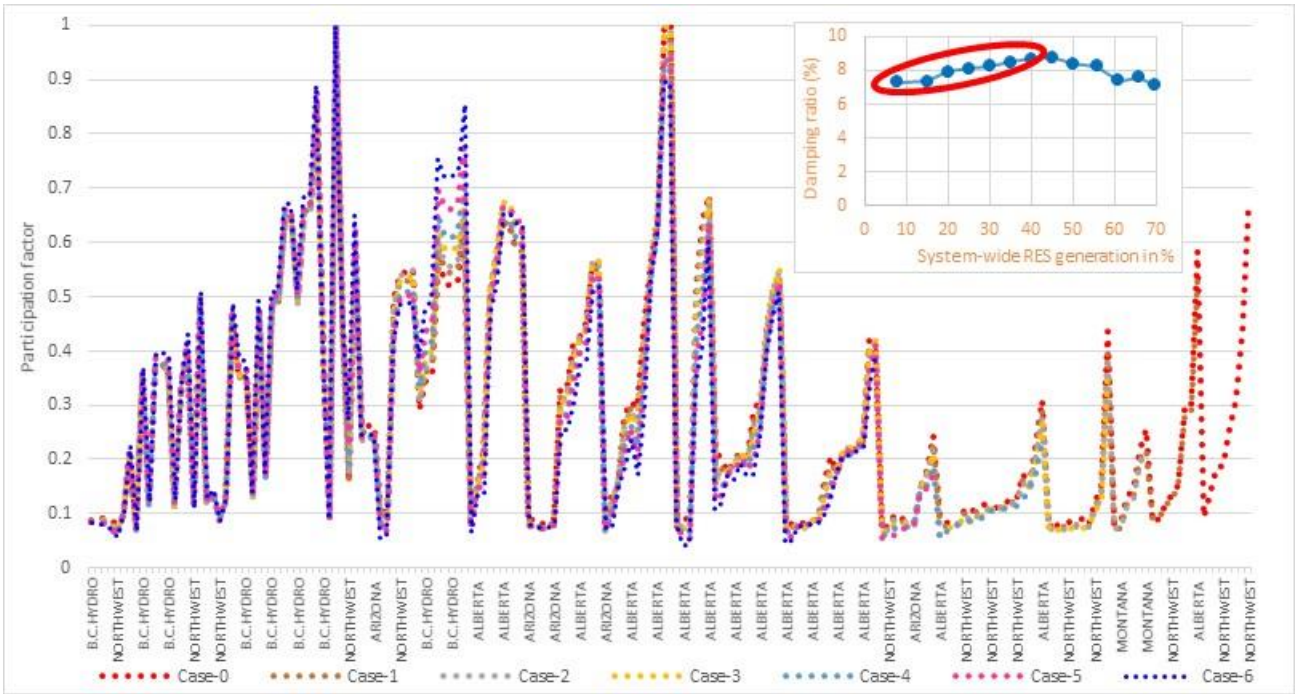

Figure 6-33. Participation factor of generators in several areas for cases 0–6 of Scenario S1 for NS-B.

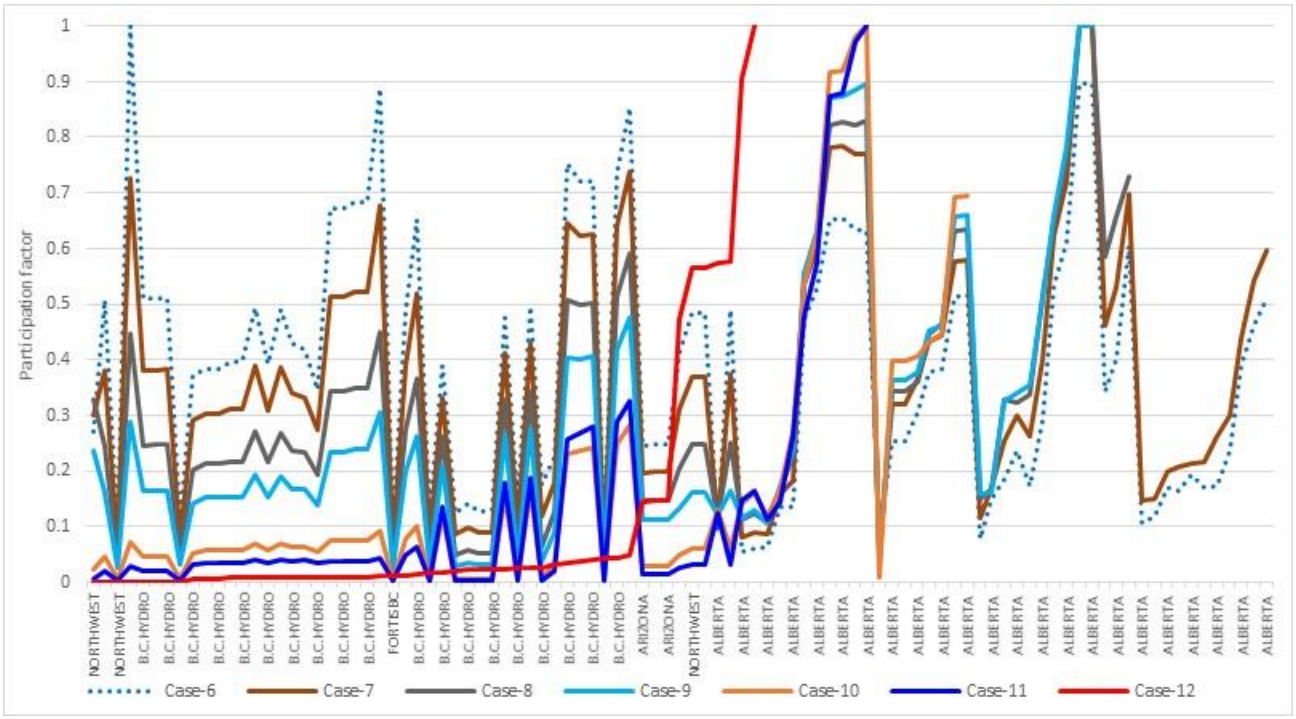

Figure 6-34. Participation factor of generators in several areas for cases 6–12 of Scenario S1 for NS-B.

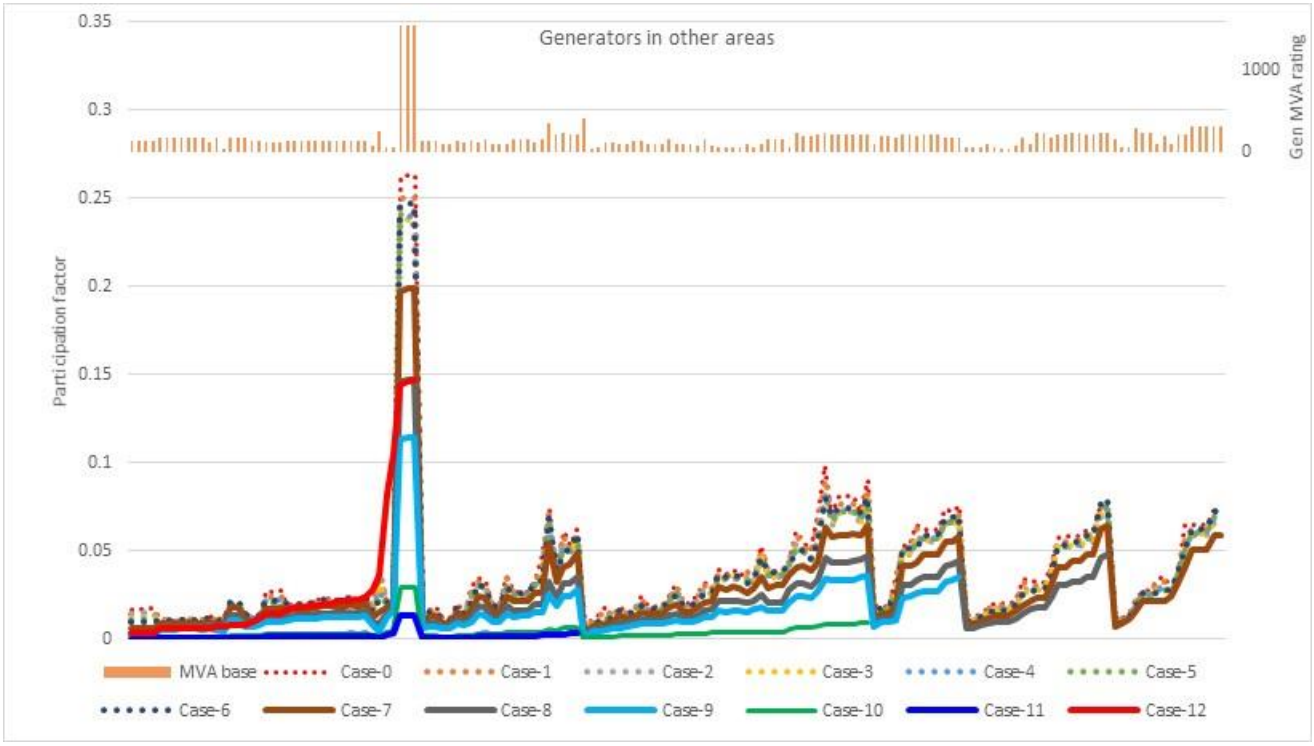

Figure 6-35. Participation factor of generators in all areas except Alberta, B.C. Hydro, Montana, and the Northwest for all cases in Scenario S1 for NS-B.

6.5.2 Scenario 1 with the Order of Replaced Generators Reversed – Scenario S2

Figure 6-36 shows the actual frequency and damping ratio of NS-A and NS-B obtained using SSAT which closely matched the estimates obtained using Prony method discussed previously.

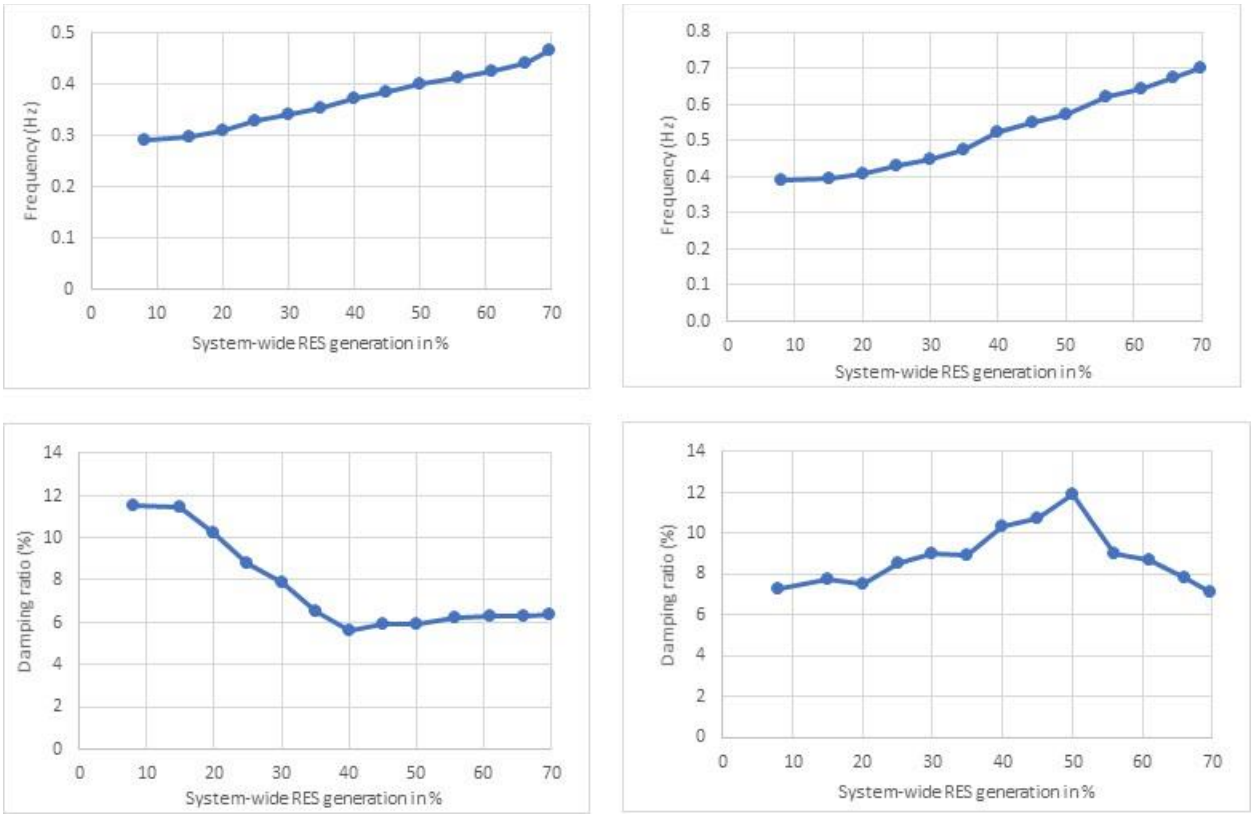

Figure 6-36. Frequency and damping ratio of NS-A (left) and NS-B (right) obtained for Scenario 2 using SSAT.

6.5.2.1 Eigenvalue Analysis of NS-A

Figure 6-37 and Figure 6-38 show the variations observed in the mode shape and participation factor of generators with increased renewable penetration. In Figure 6-38, only those generators that had a value of the participation factor at least 0.05 in the base case are included.

As shown in Figure 6-37, the mode shape for NS-A remained unchanged with increased renewable penetration level for all cases. Figure 6-38 through Figure 6-40 show that the participation factor of B.C. Hydro, Montana, and the Northwest first increased significantly until Case-6 and then it started decreasing. This variation in the participation factor of these generators explain the change in the trends observed in the damping ratio of NS-A, which first decreases and then increases. The participation factor of the remaining synchronous generators in Alberta decreased slightly as generators having high-

participation factors were replaced. The participation factor of generators in other areas increased from cases 0–12 with Palo Verde units becoming the generators having the highest participation factor in Case-12 as shown in Figure 6-41.

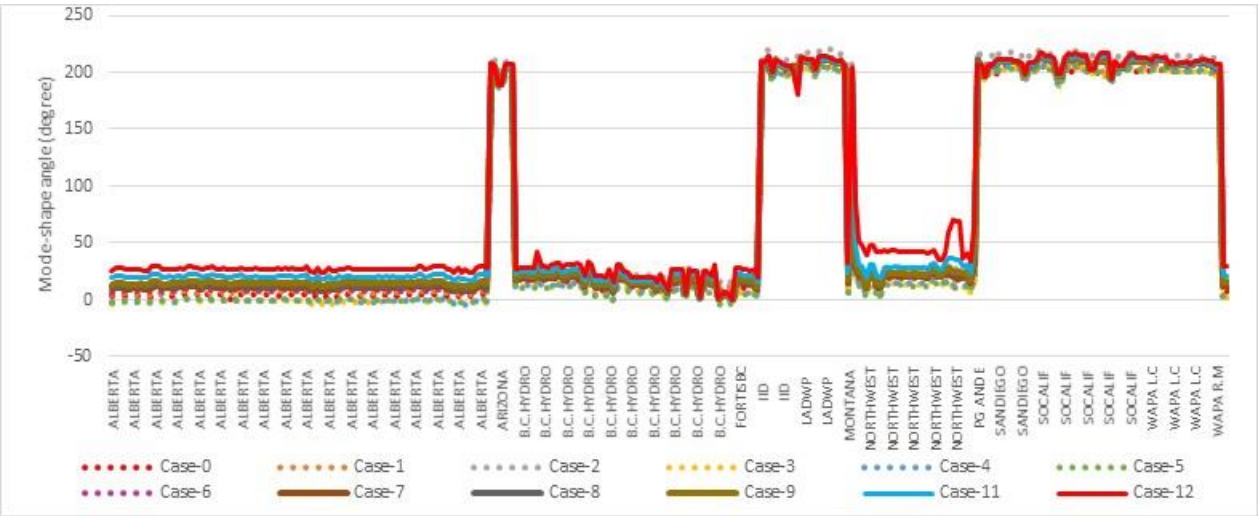

Figure 6-37. Comparison of mode shape of generators for all cases in Scenario S2 for NS-A.

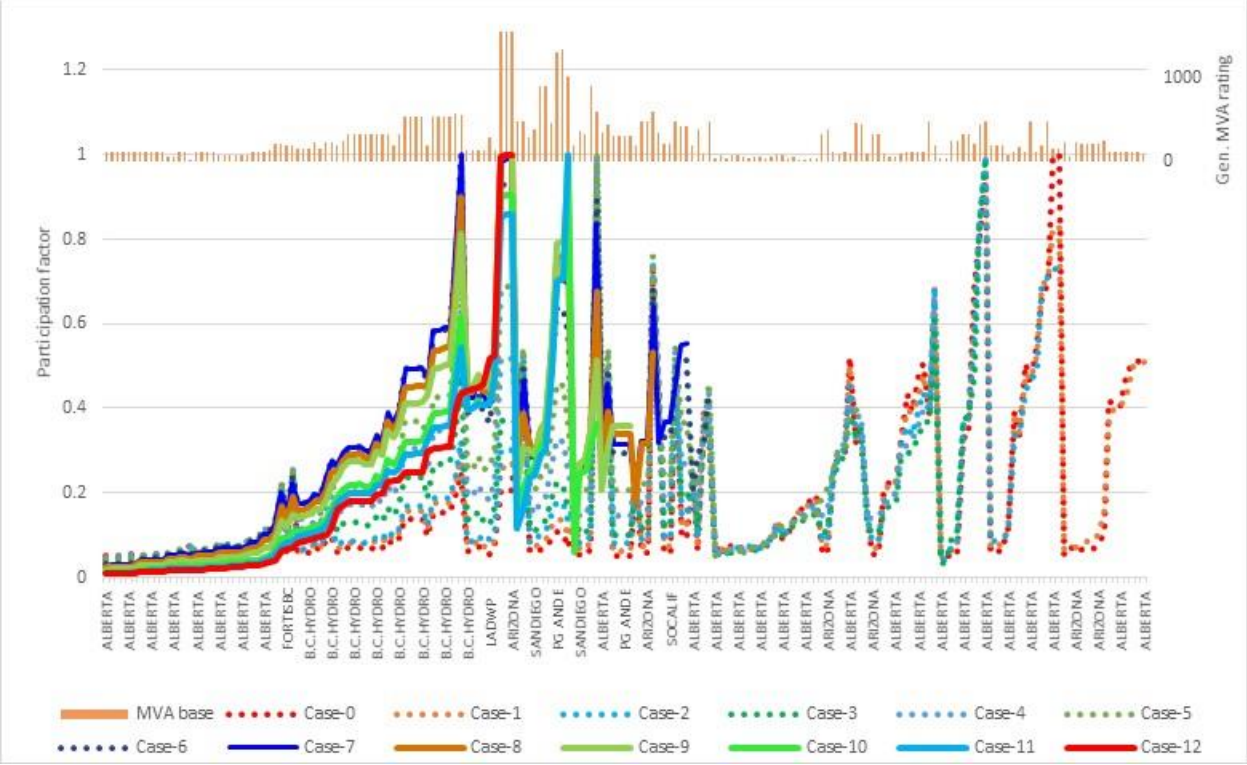

Figure 6-38. Participation factor of generators for all cases in Scenario S2 for NS-A.

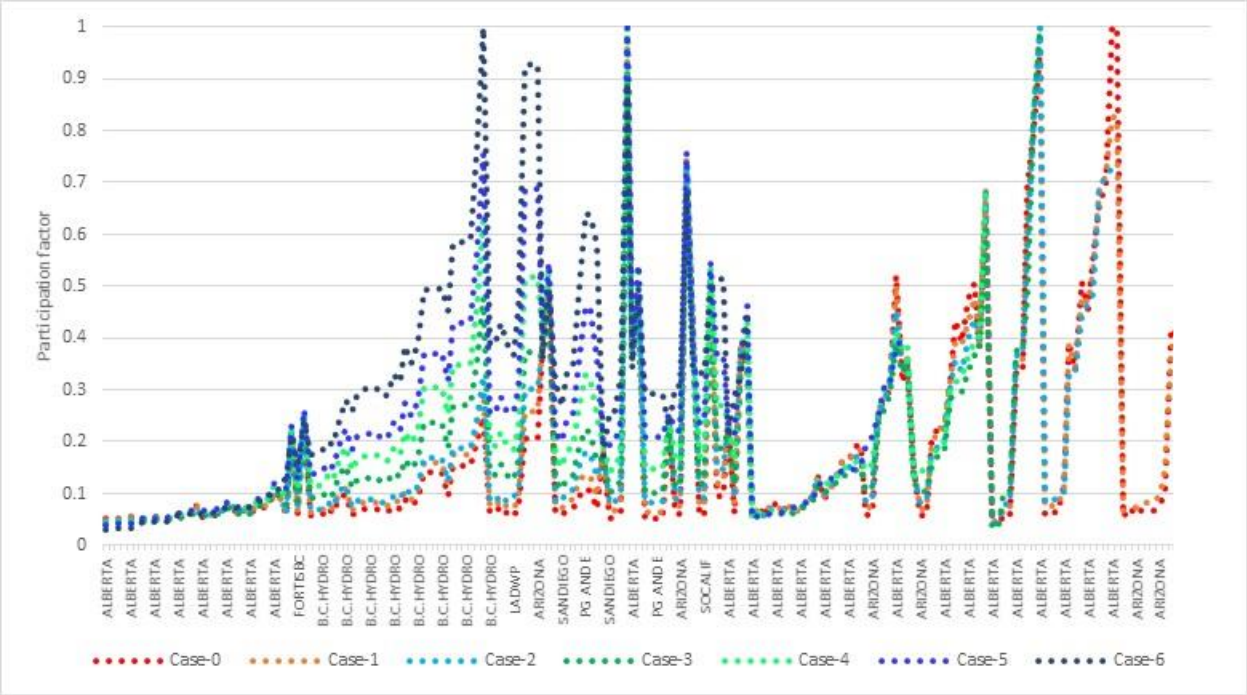

Figure 6-39. Participation factor of generators for cases 0–6 of Scenario S2 for NS-A.

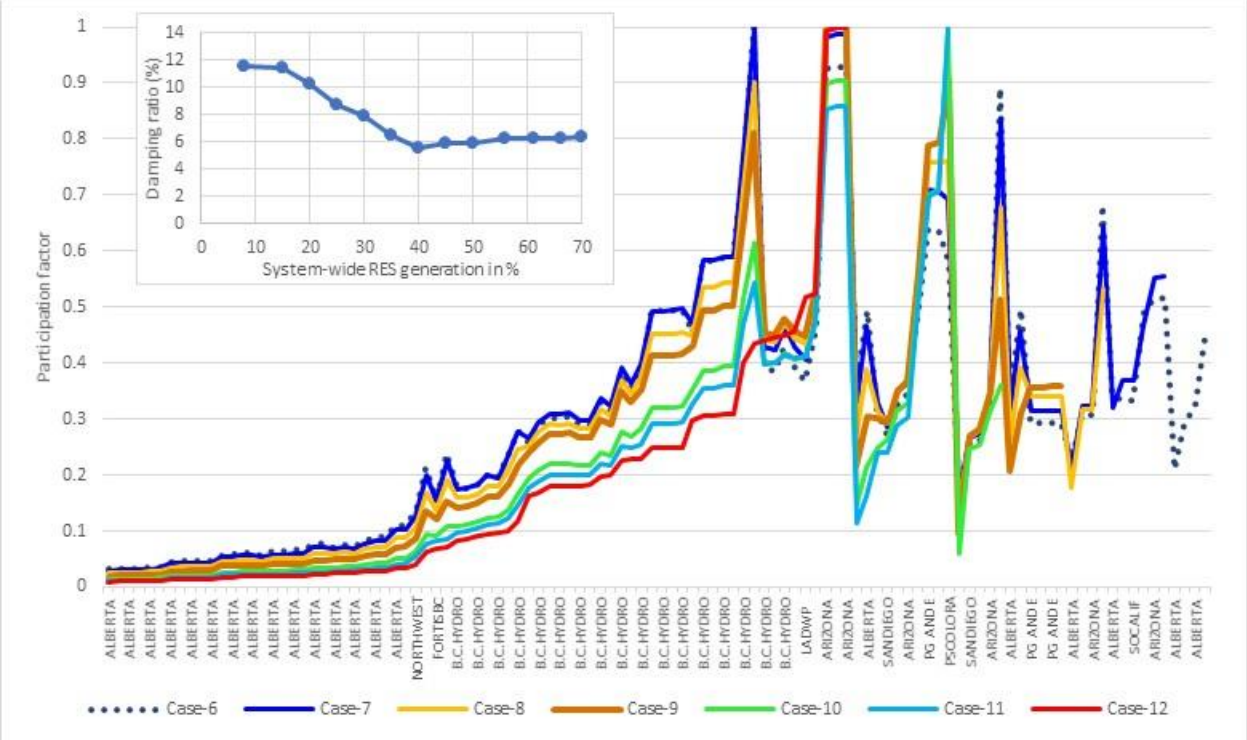

Figure 6-40. Participation factor of generators for cases 6–12 of Scenario S1 for NS-A.

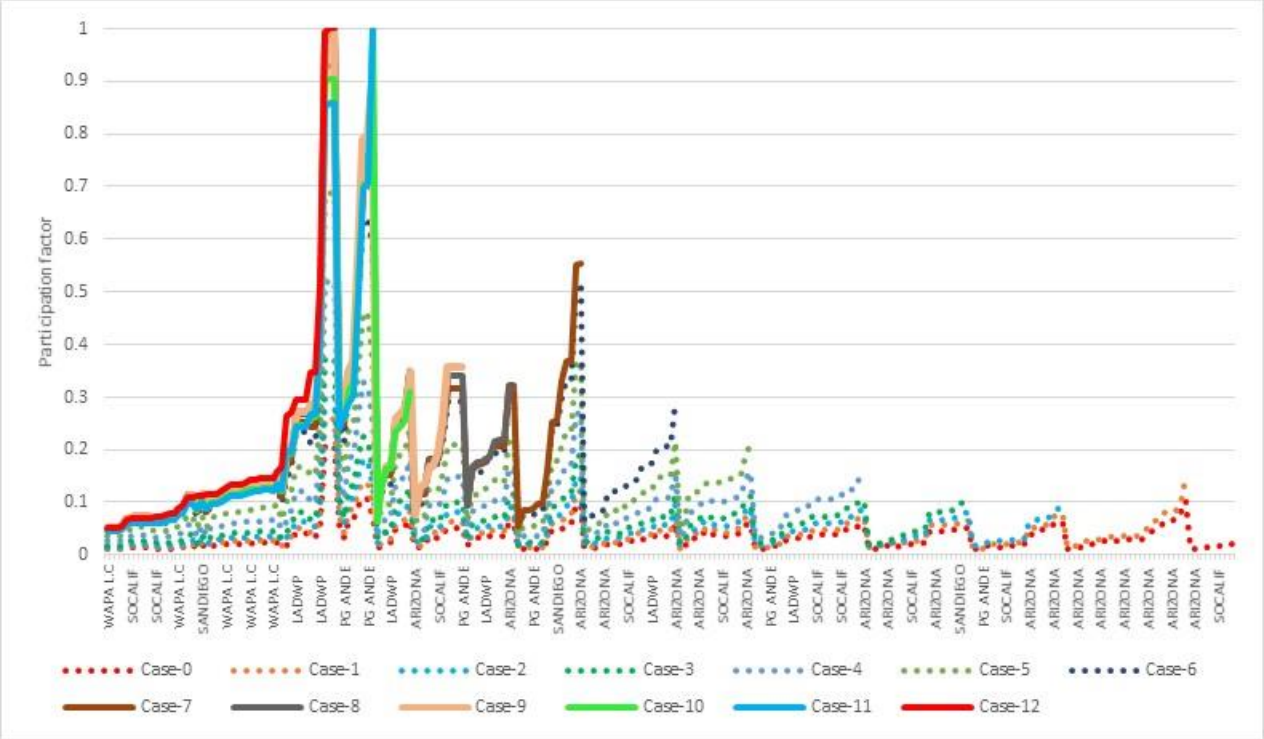

Figure 6-41. Participation factor of generators in all areas except Alberta, B.C. Hydro, Montana, and the Northwest for all cases in Scenario S2 for NS-A.

6.5.2.2 Eigenvalue Analysis of NS-B

Figure 6-42 and Figure 6-43 show the variations observed in the mode shape and participation factor of generators with increased renewable penetration for NS-B. In Figure 6-43, only those generators included that had a value of the participation factor at least 0.1 in the base case were included.

Figure 6-42 shows the mode shape of generators in B.C. Hydro start changing from Case-6 onward where some generators started to oscillate with Alberta and other generators in the South against generators in the North. In Case-8, where the damping ratio of NS-B is the highest, the mode shape of generators changed such that Alberta and some generators in B.C. Hydro oscillated against other generators in B.C. Hydro, and generators in the Northwest oscillated against generators in the South. From Case-9 onward, mode shape again looked like the previous cases. The sudden changes observed in the participation factor of generators in several areas can be explained by the changes observed in the mode shape of generators.

As shown in Figure 6-44, the participation factor of generators in B.C. Hydro decreased significantly until Case-7, then it increased significantly for some generators in Case-8, the case in which the mode shape looked different and then the participation factor of those generators started decreasing again. In cases 11–12, participation factor of generators in B.C. Hydro was not significant. Figure 6-46, Figure 6-47, and

Figure 6-48 show the participation factor of generators in other areas not including Alberta and B.C Hydro decreased until Case-6, increased in Case-7, decreased in Case-8, increased in Case-9, decreased in Case-10, and then increased in cases 11 and 12. As shown in Figure 6-45, the participation factor of most of the generators in Alberta increased until case 5 and then it decreased significantly in case 6 in which a generator in P.S. Colorado became the highest participation factor. After case 6, the participation factor of generators again increased from Case-7 onward. In cases 11 and 12, the participation factor of the generators increased significantly.

From the above explanation, it is clear that the trends observed in the participation factor and mode shape of generators for NS-B for several cases in Scenario S2 were somewhat inconsistent, which is also true for the damping ratio of NS-B.

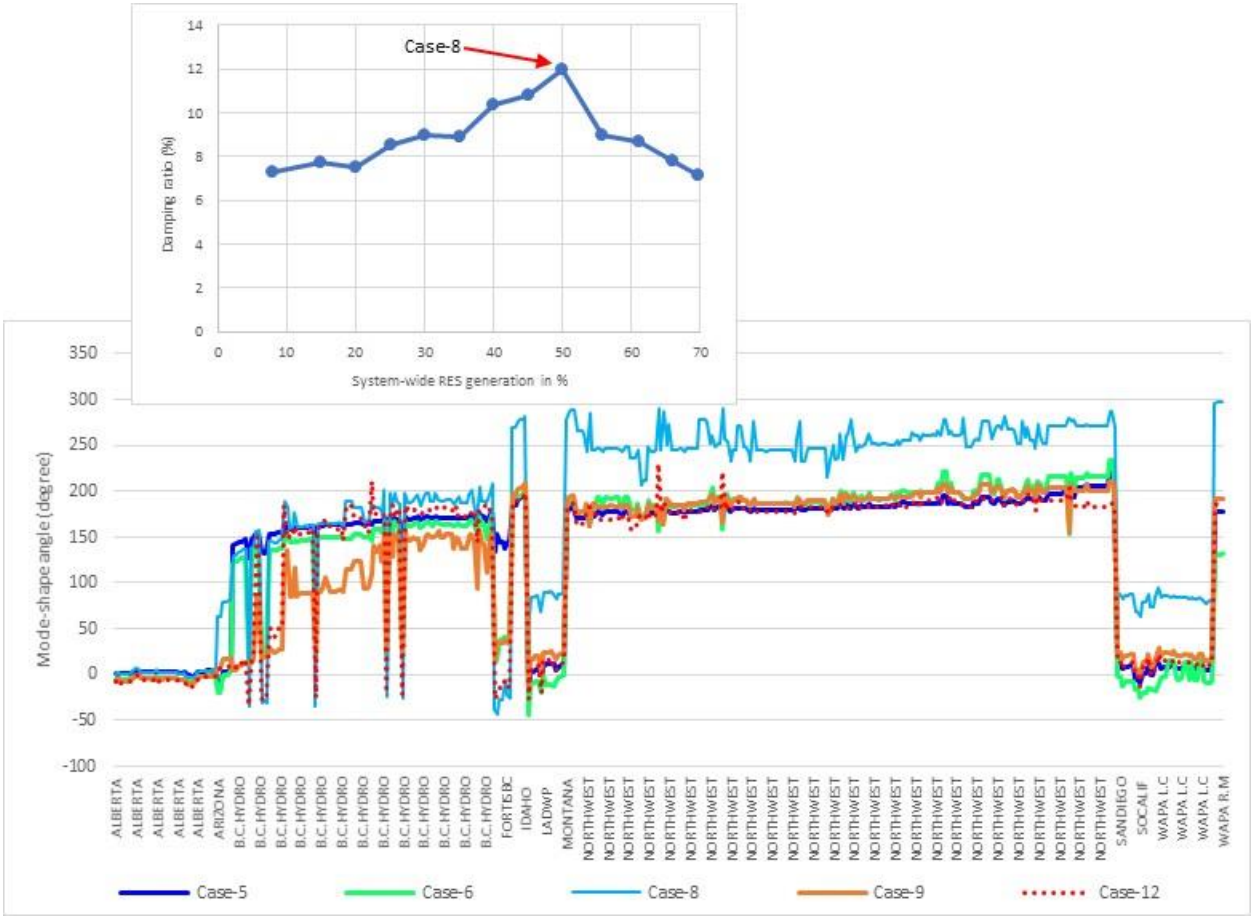

Figure 6-42. Comparison of mode shape of generators for selected cases in Scenario S2 for NS-B.

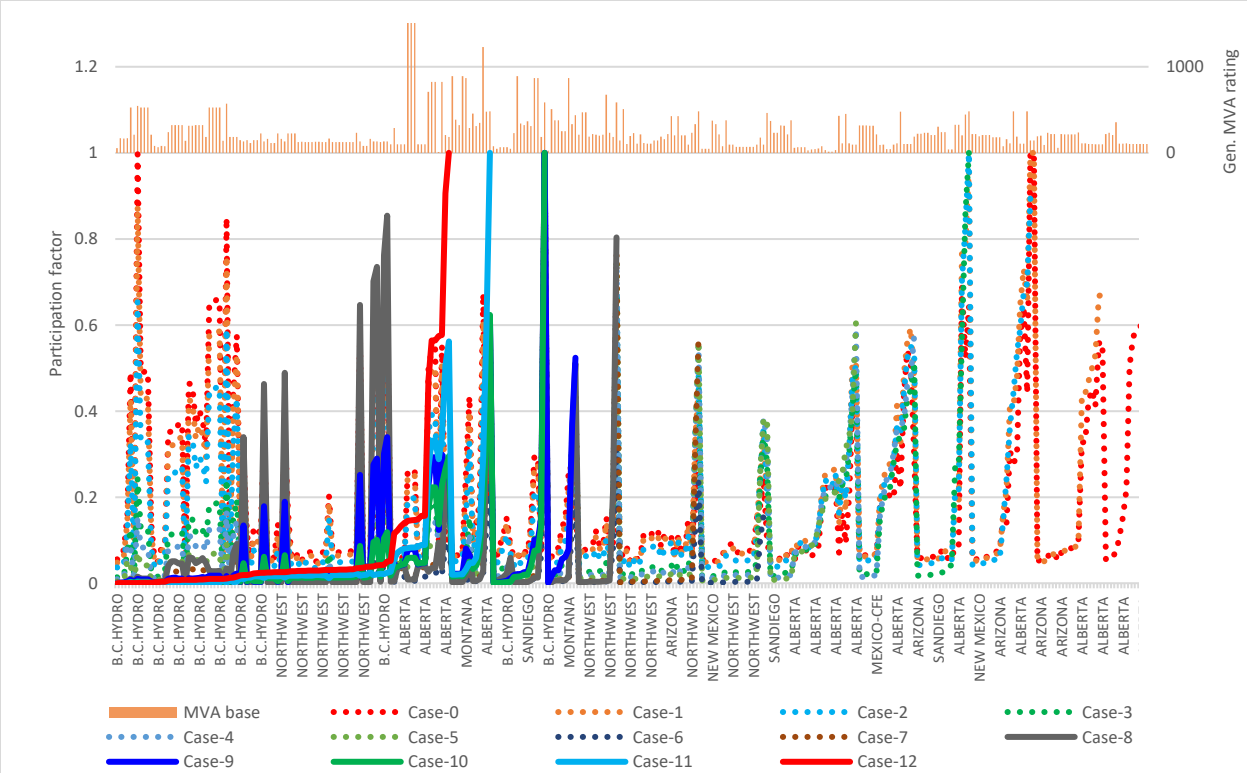

Figure 6-43. Participation factor of generators for all cases in Scenario S2 for NS-B.

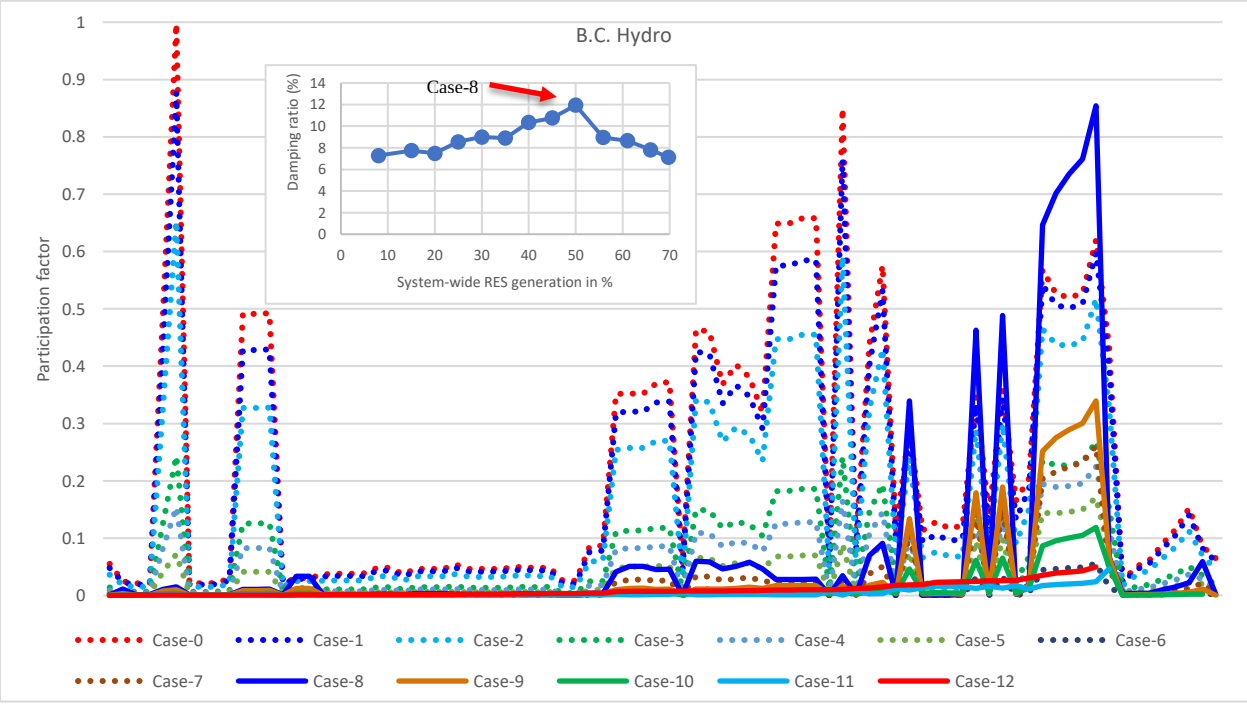

Figure 6-44. Participation factor of generators in B.C. Hydro for all cases in Scenario S2 for NS-B.

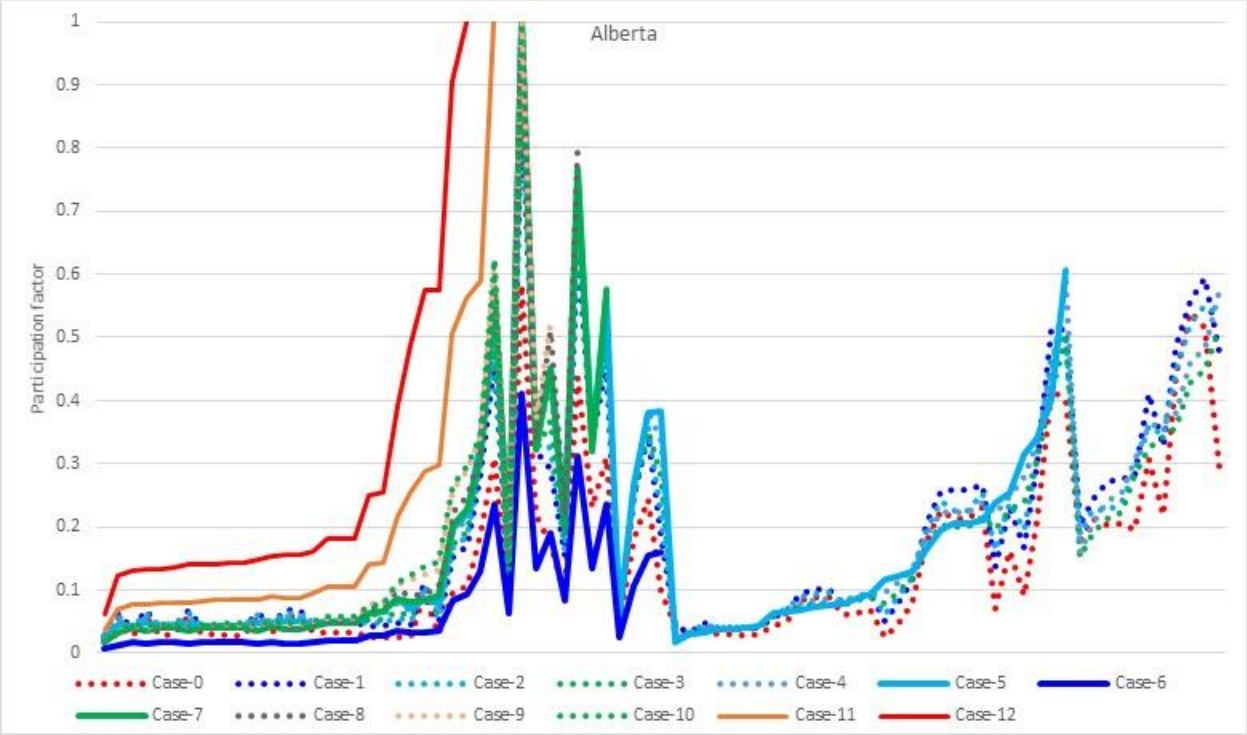

Figure 6-45. Participation factor of generators in Alberta for all cases in Scenario S2 for NS-B.

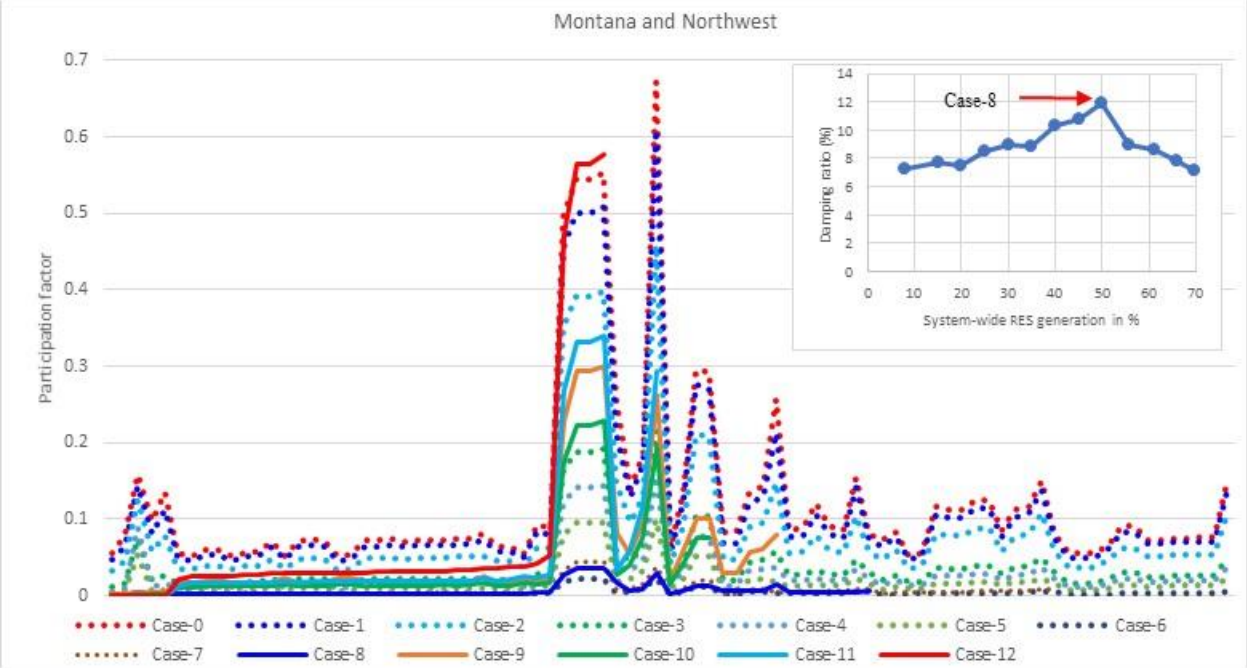

Figure 6-46. Participation factor of generators in Montana and the Northwest for all cases in Scenario S2 for NS-B.

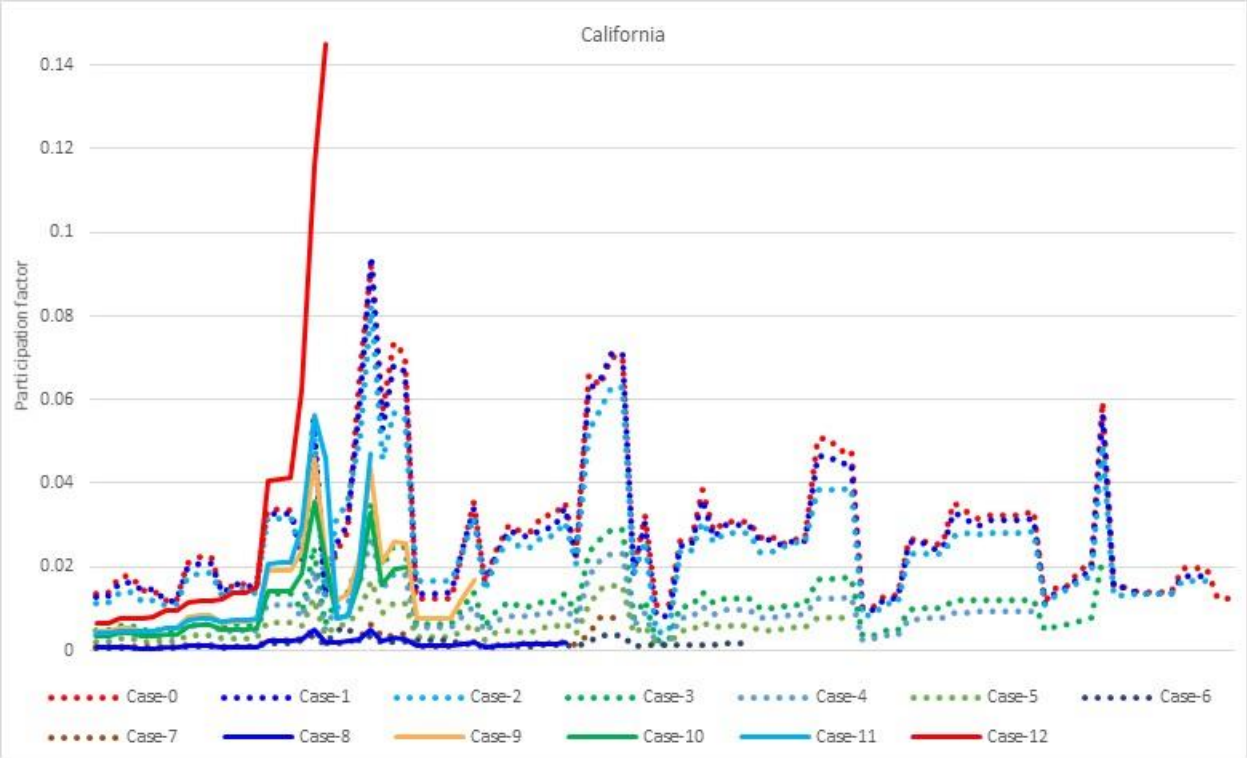

Figure 6-47. Participation factor of generators in California for all cases in Scenario S2 for NS-B.

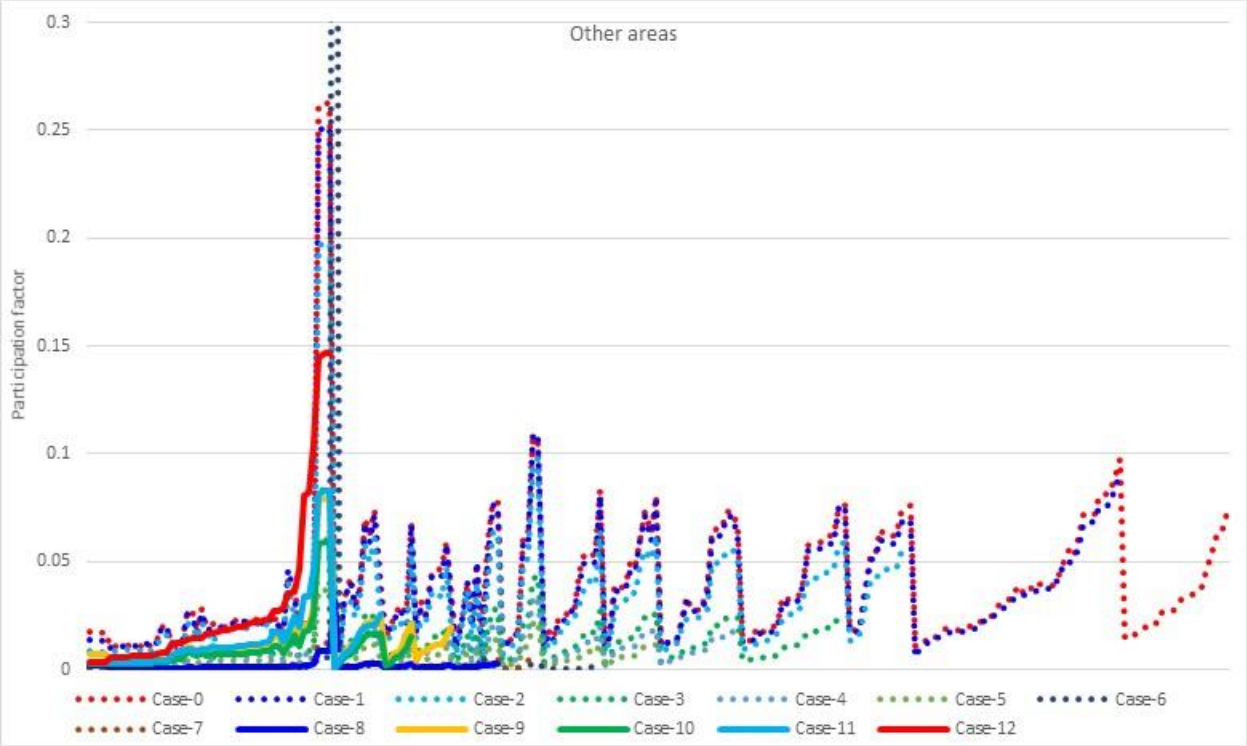

Figure 6-48. Participation factor of generators in other areas for all cases in Scenario S2 for NS-B.

6.5.3 Increase of Renewable Penetration Level in Alberta Only – Scenario S3

Figure 6-49 shows the actual frequency and damping ratio of NS-A and NS-B obtained using SSAT which closely resemble with the estimates obtained using the Prony method.

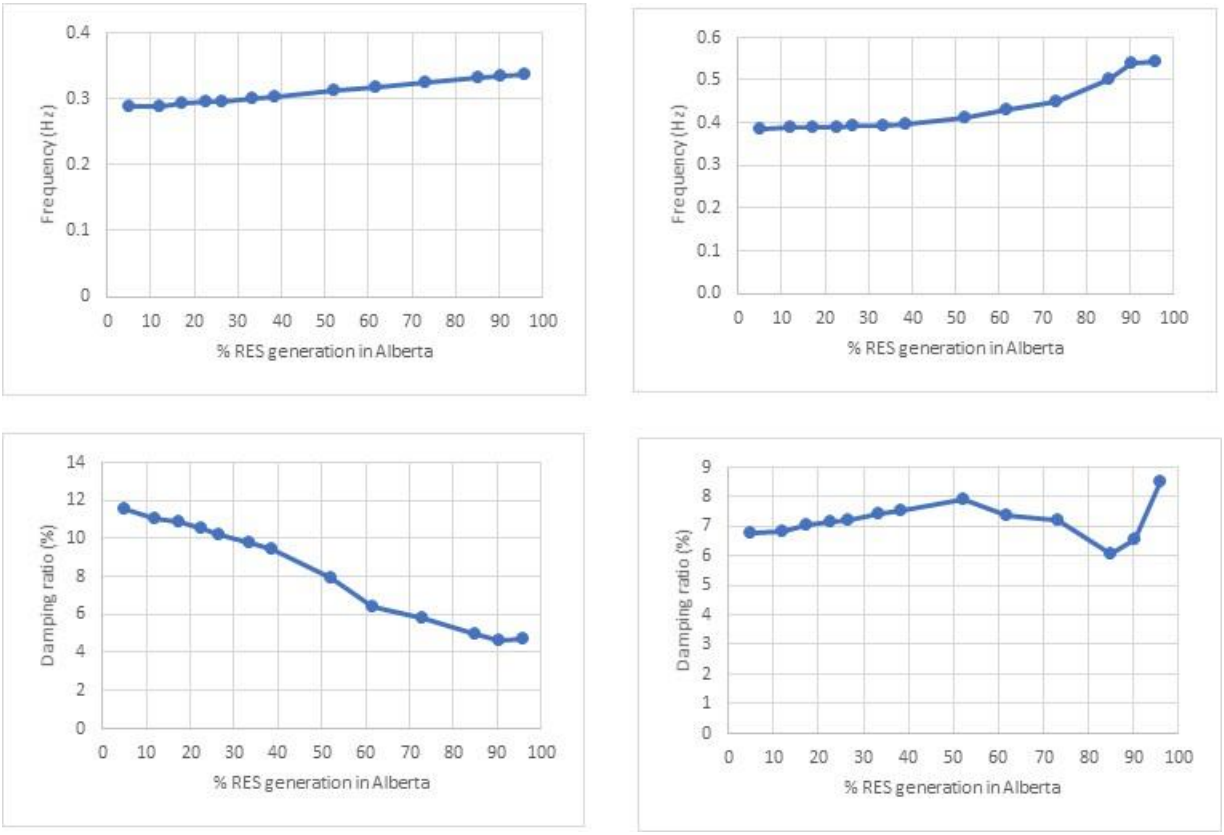

Figure 6-49. Frequency and damping ratio of NS-A (left) and NS-B (right) obtained using SSAT for Scenario S3.

6.5.3.1 Eigenvalue Analysis of NS-A

Figure 6-50 and Figure 6-51 show the variations observed in the mode shape and participation factor of generators in several areas with increased renewable penetration. In Figure 6-27, only those generators that had a value of the participation factor at least 0.05 in the base case are included.

In Figure 6-50, it can be seen that the mode shape of generators remained the same as the base case for all cases. As synchronous generators were replaced with inverter-based resources in Alberta only, the participation factor of generators in B.C. Hydro increased significantly until Case-9 and then did not change much as shown in Figure 6-51. On the other hand, the participation factor of generators in Alberta did not change much until Case-9, decreased significantly in Case-10, and then decreased slightly in cases 11 and 12. Therefore, the trends observed in the damping ratio of NS-A can be explained by the variations

observed in the participation factor of generators as shown in Figure 6-52 and Figure 6-53. These results also indicate that with increased renewable penetration in Alberta, generators in B.C. Hydro will participate heavily in NS-A and therefore will have more control over NS-A.

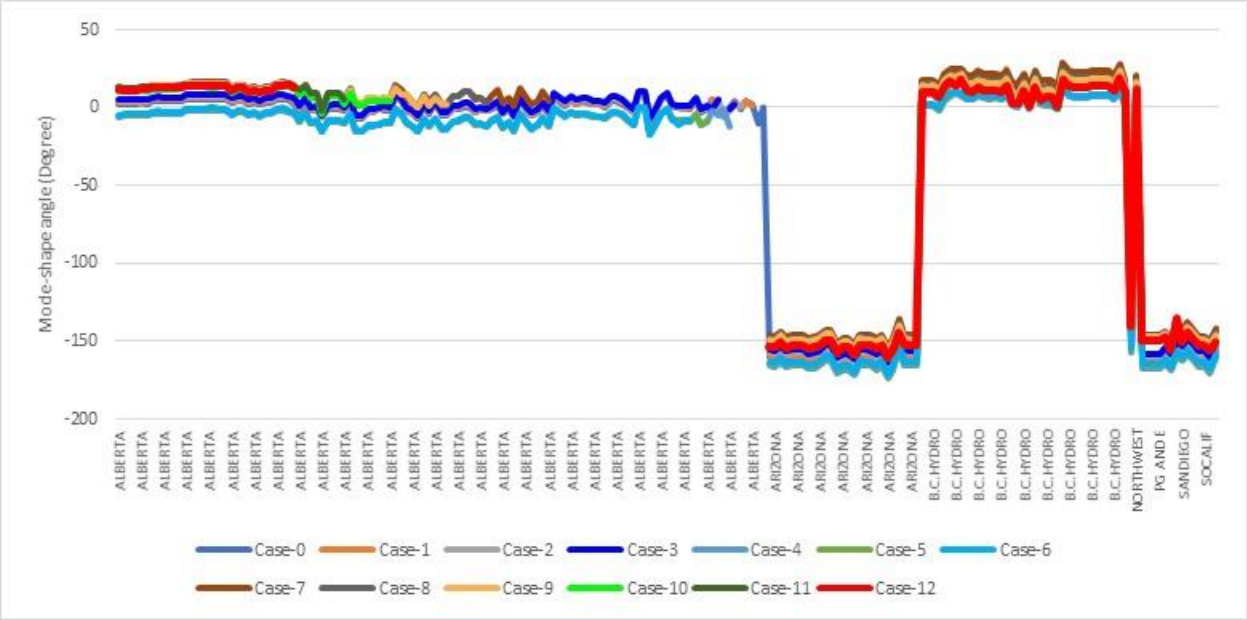

Figure 6-50. Comparison of mode shape of generators for all cases in Scenario S3 for NS-A.

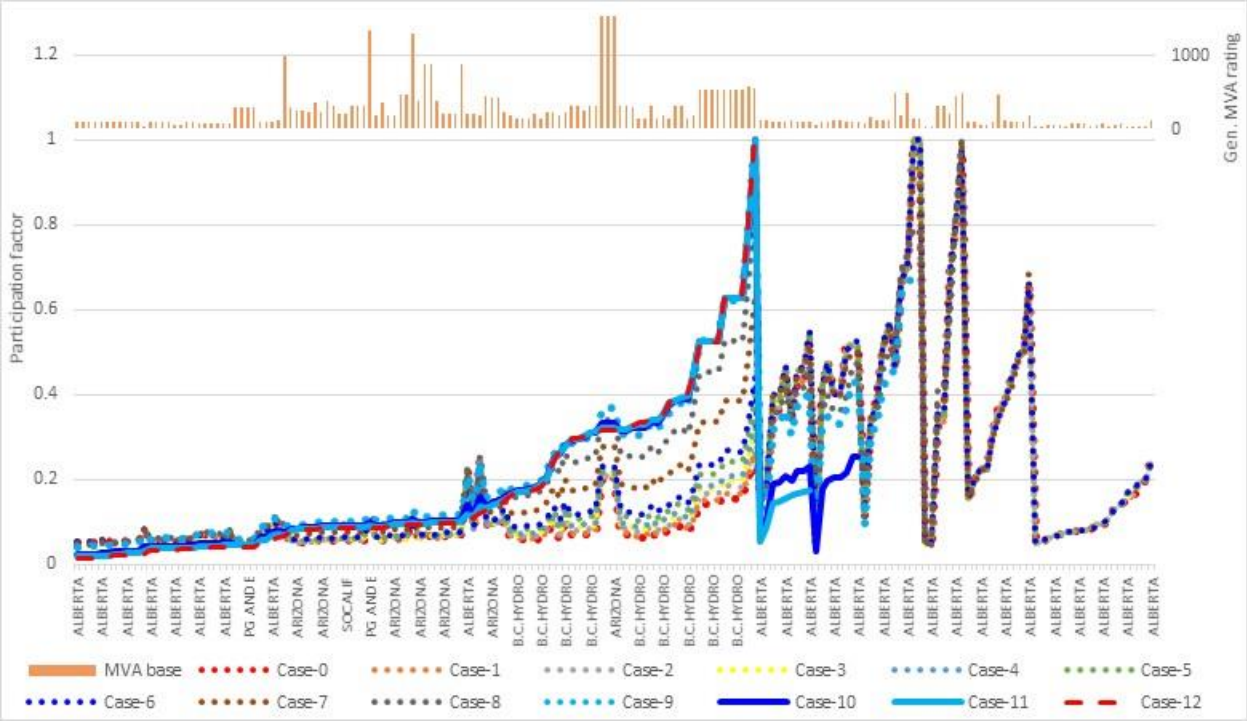

Figure 6-51. Participation factor of generators for all cases in Scenario S3 for NS-A.

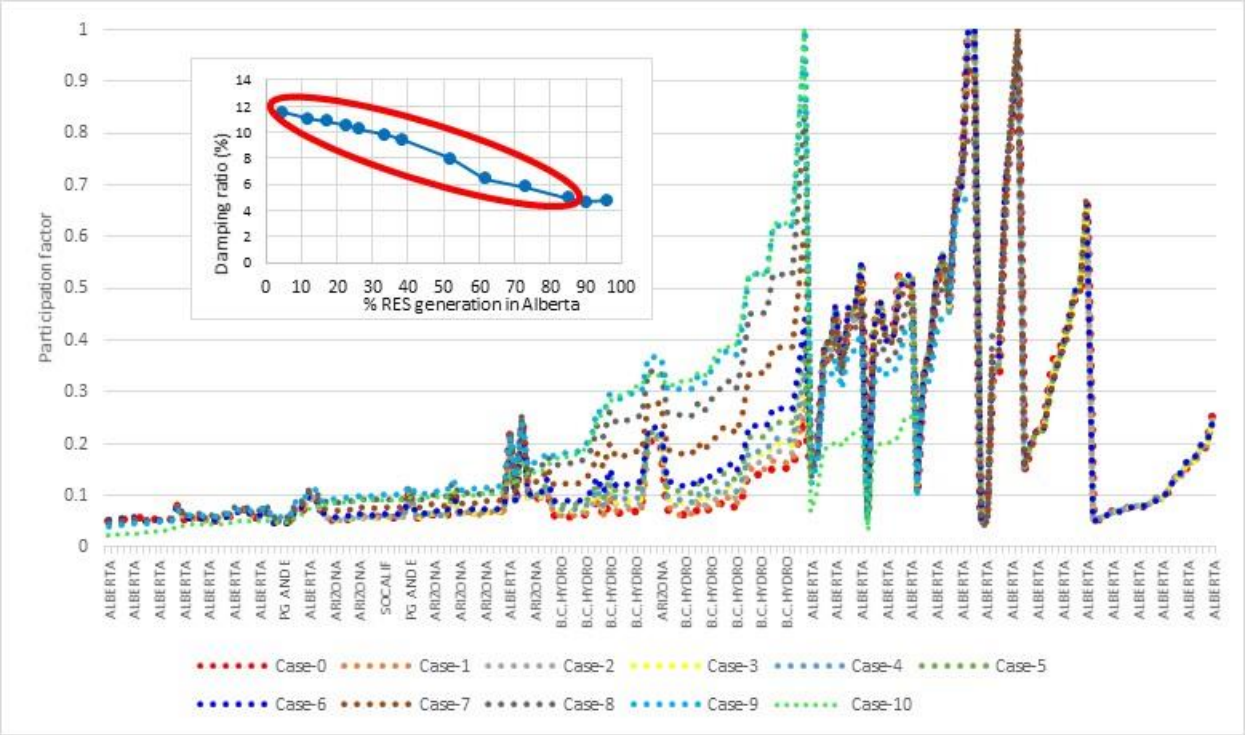

Figure 6-52. Participation factor of generators for cases 0–10 in Scenario S3 for NS-A.

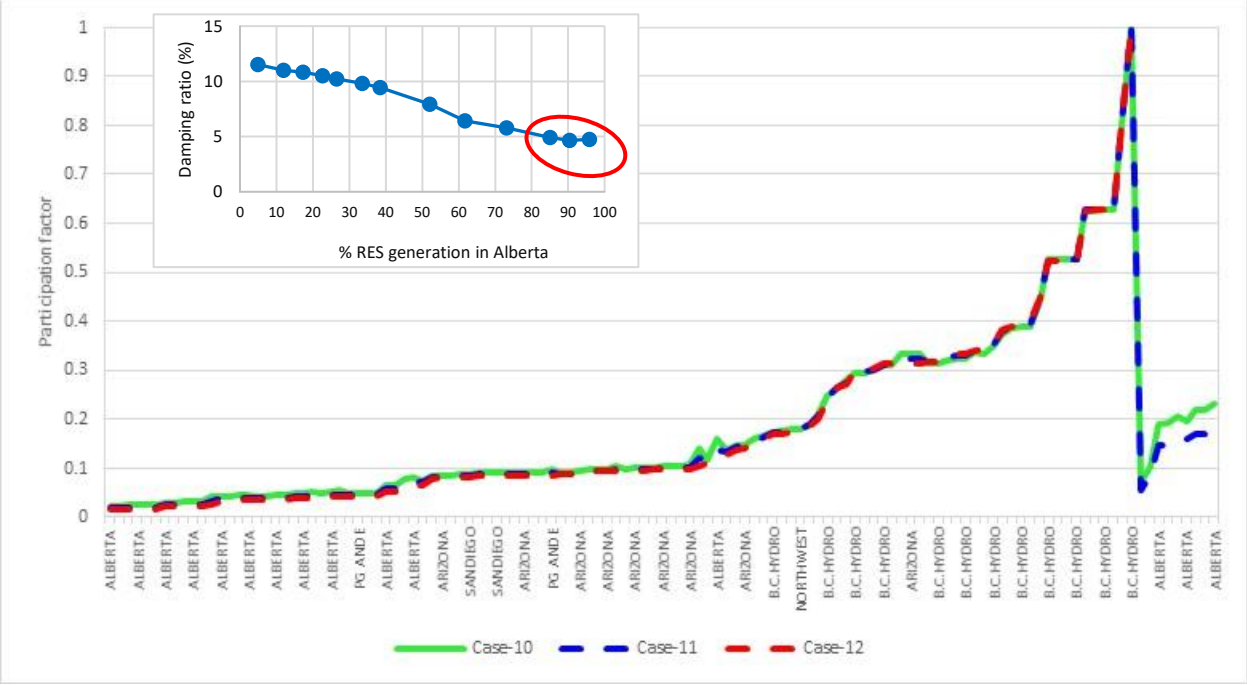

Figure 6-53. Participation factor of generators for cases 10–12 in Scenario S3 for NS-A.

6.5.3.2 Eigenvalue Analysis of NS-B

Figure 6-54 and Figure 6-55 show the variations observed in the mode shape and participation factor of generators in several areas with increased renewable penetration for NS-B. Figure 6-55 shows participation factor of only those generators included that had a value of at least 0.1 in the base case.

As seen in Figure 6-54, the mode shape for NS-B remained unchanged with increased renewable penetration level until Case-9. From Case-10 onward, generators in B.C. Hydro started to oscillate with Alberta and other generators in the South against generators in the North. In cases 11 and 12, generators in Alberta, B.C. Hydro, and the Northwest started oscillating with generators in the South against other generators in the North. This explains the trend change observed in the damping ratio of NS-B in cases 11 and 12.

Analyzing Figure 6-55 and Figure 6-58, it can be seen that the participation factor of generators in all areas except Alberta decreased significantly from Case-0 to Case-10 and then it started increasing as the mode shape of generators in B.C. Hydro changed. However, the participation factor of generators in Alberta did not change much until Case-7 and then started increasing until Case-10. The participation factor of generators in Alberta decreased in Case-12 as the generators in B.C. Hydro started oscillating with the generators in Alberta.

The variations observed in the mode shape and the participation factor explain the trend observed in the damping ratio of NS-B, which increased until Case-7, decreased until Case-10, and then started increasing again.

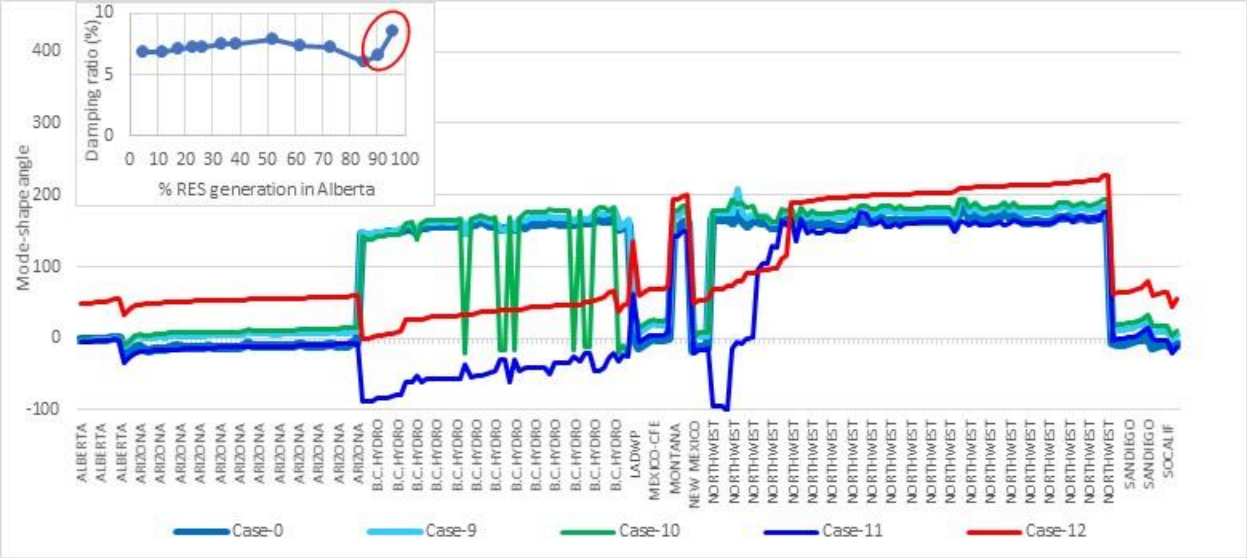

Figure 6-54. Comparison of mode shape of generators for selected cases in Scenario S3 for NS-B.

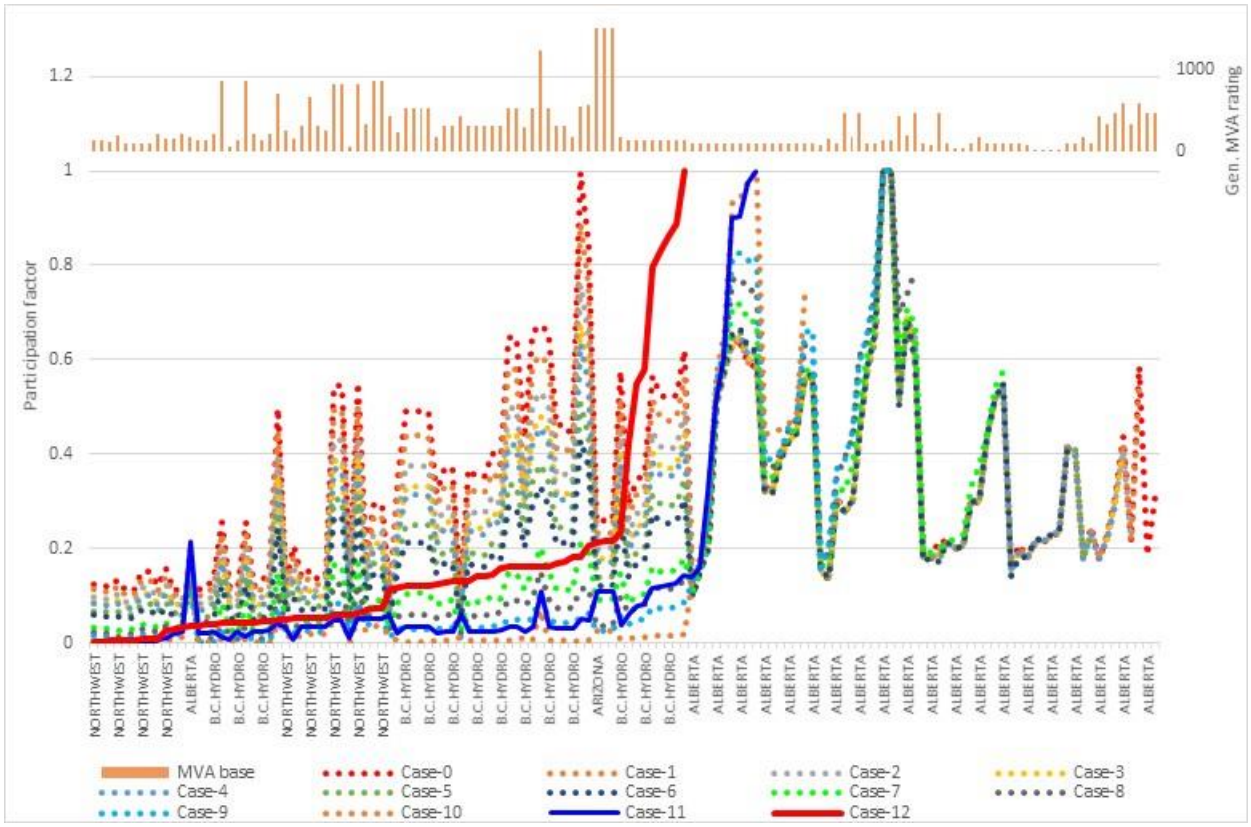

Figure 6-55. Participation factor of generators for all cases in Scenario S3 for NS-B.

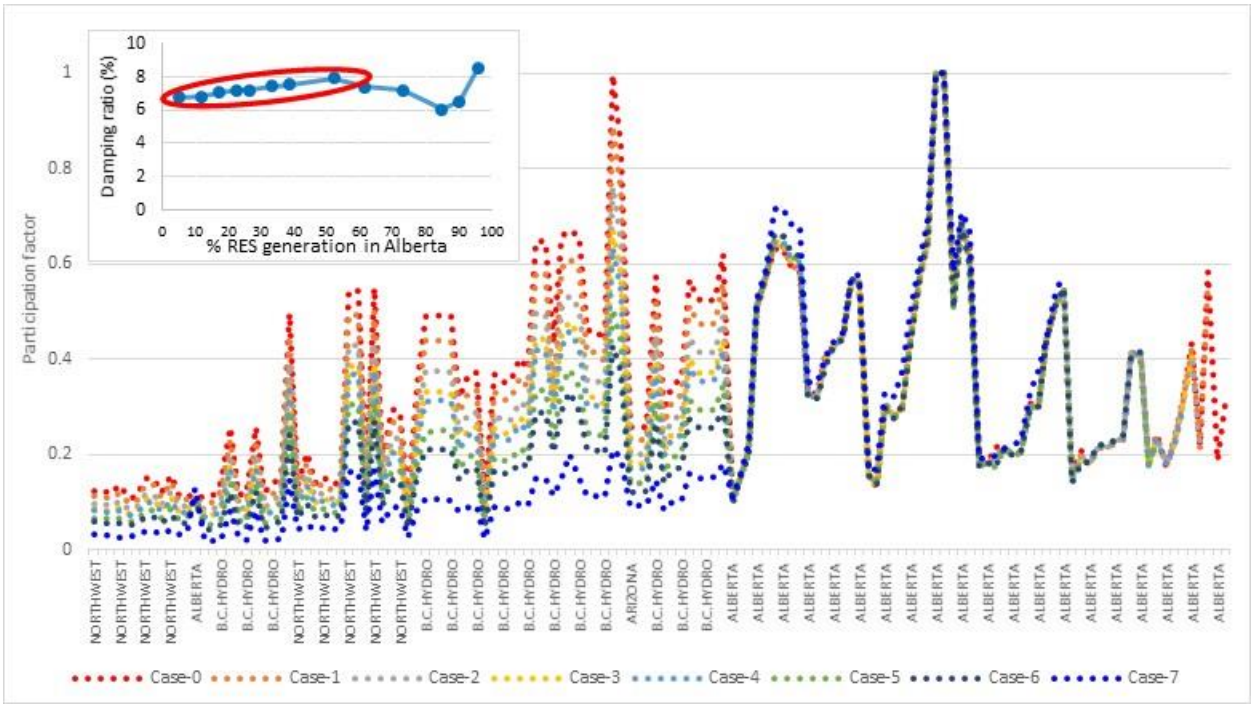

Figure 6-56. Participation factor of generators for cases 0–7 in Scenario S3 for NS-B.

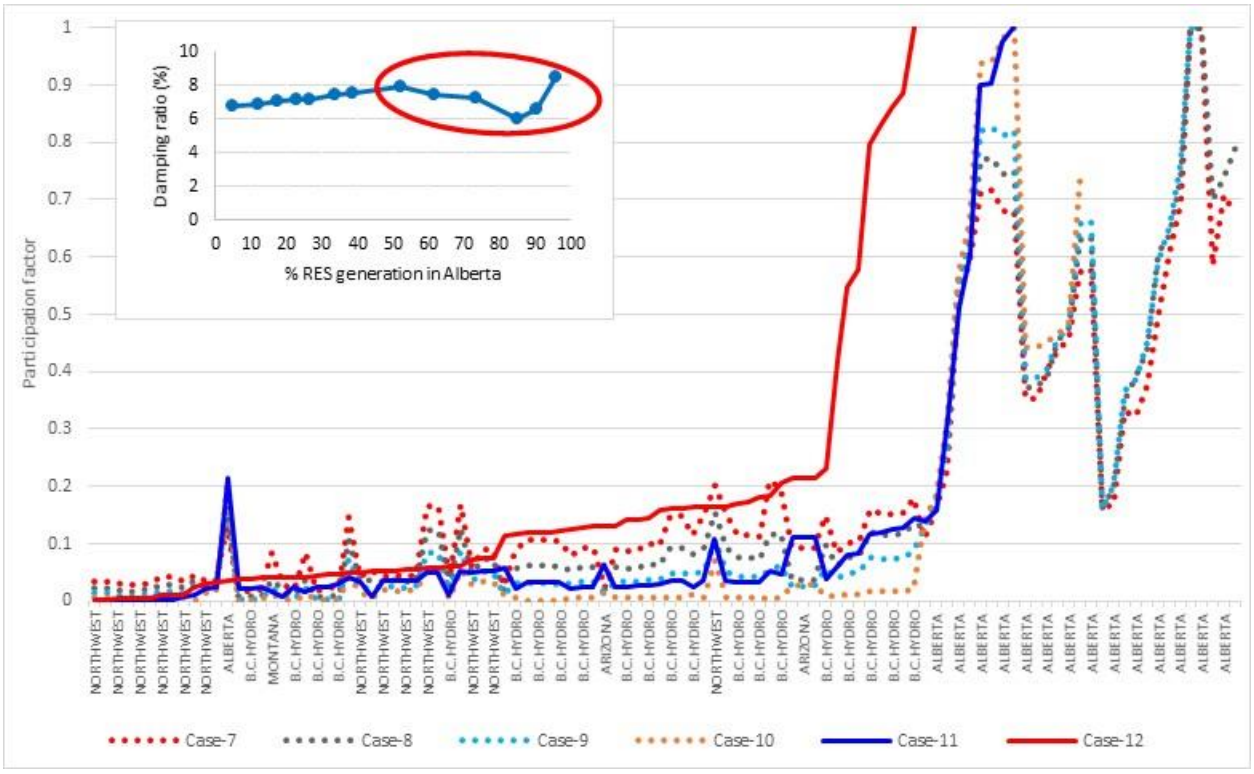

Figure 6-57. Participation factor of generators for cases 7–12 in Scenario S3 for NS-B.

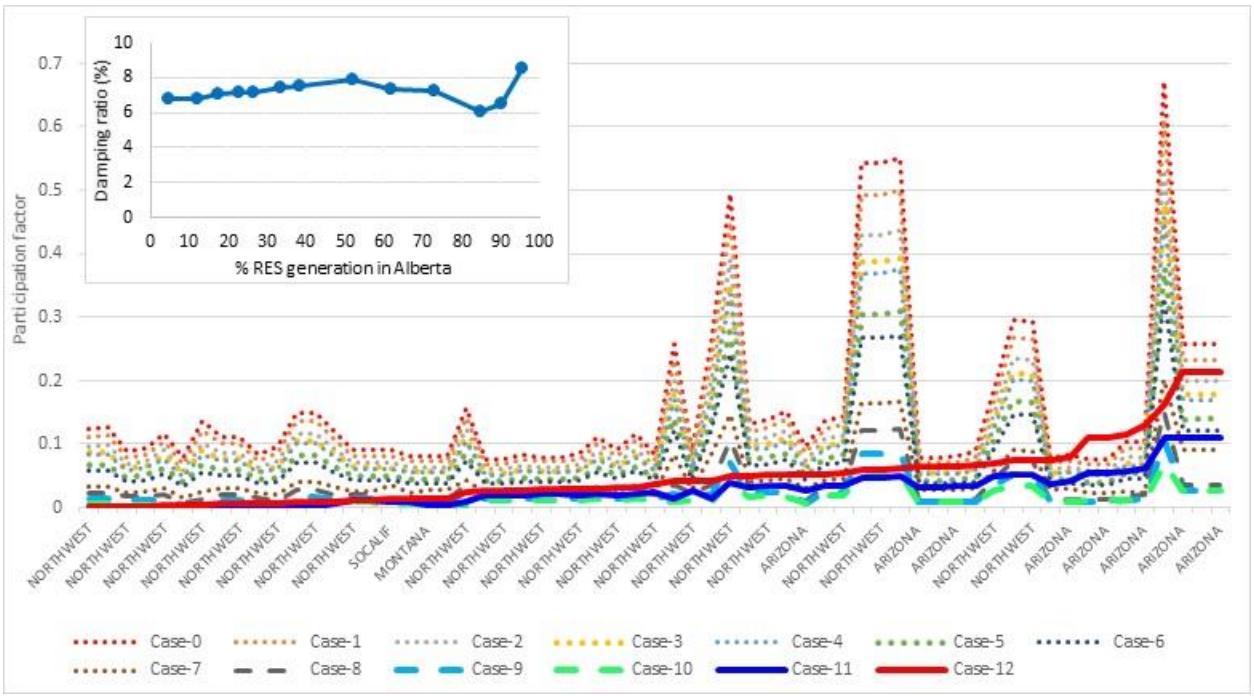

Figure 6-58. Participation factor of generators in areas not including Alberta and B.C. Hydro for all cases in Scenario S3 for NS-B.

6.5.4 Increase of RES Penetration Level in All Areas Except Alberta – Scenario S4

Figure 6-59 shows the actual frequency and damping ratio of NS-A and NS-B obtained using SSAT and the estimates from the Prony method. The estimates of frequency and damping ratio of both modes had overall good match with their actual values obtained by using SSAT. However, there was some discrepancy in the estimates of damping ratio of NS-A from Case-8 onward. This is partially because the Prony method provides estimates and there will be some mismatch with the actual value. However, analyzing SSAT results found there was another new mode in the frequency range of NS-A that resulted in biased estimate as the Prony method could not resolve these two modes. The eigenvalue analysis results will be discussed next for NS-A and NS-B for Scenario S4.

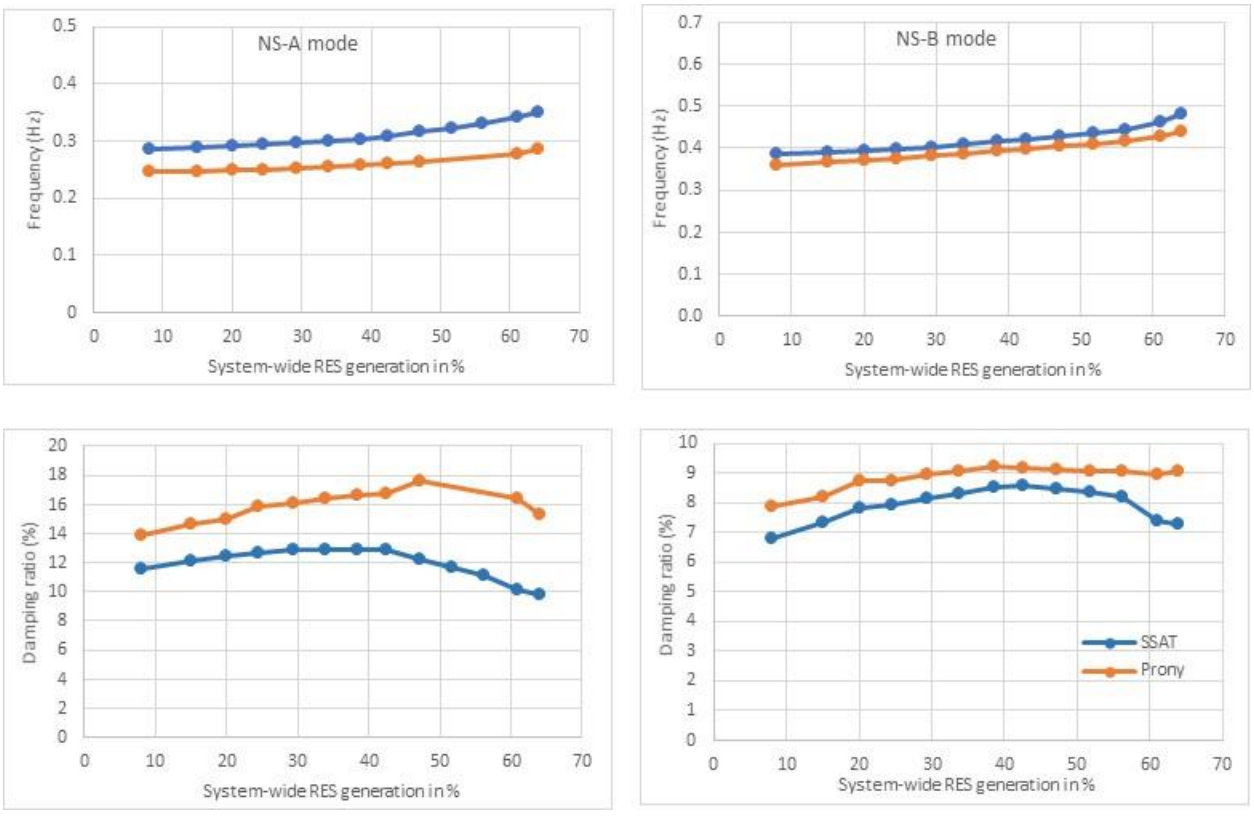

Figure 6-59. Frequency and damping ratio of NS-A (left) and NS-B (right) obtained using SSAT and the corresponding estimates obtained using the Prony method for Scenario 4.

6.5.4.1 Eigenvalue analysis of NS-A

Figure 6-60 and Figure 6-61 show the variations observed in the mode shape and participation factor of generators with increased renewable penetration, only those generators that had a value of the participation factor at least 0.05 in the base case were included.

In Figure 6-60 and Figure 6-61, it can be seen that from case 7 onward generators in the Northwest started to oscillate against Alberta. Also, from Case-10 onward, generators in B.C. Hydro started to oscillate against Alberta. These results show that as the amount of synchronous generation decreases system wide except in Alberta, generators in Alberta will start oscillating against rest of the system for NS-A. These changes in the mode shape explain the trend change observed in the damping ratio of NS-A for Scenario S4. The effect of this change in mode shape also can be seen in the participation factor of generators in Montana, the Northwest, and B.C. Hydro as shown in Figure 6-64. The participation factor of generators in Montana and Northwest decreased until Case-7, after which it started to increase. Similarly, participation factor of generators in B.C. Hydro decreased until Case-9, after which it started to increase. The participation factor of generators in Alberta did not change much for all the cases but increased slightly while others decreased slightly. The participation factor of generators in other areas increased until Case-10, after which it decreased slightly as shown in Figure 6-65. Overall, the participation factor of generators did not change much. The change in the trends observed in the damping ratio was more likely caused by the change in mode shape of generators in Montana, the Northwest, and B.C. Hydro.

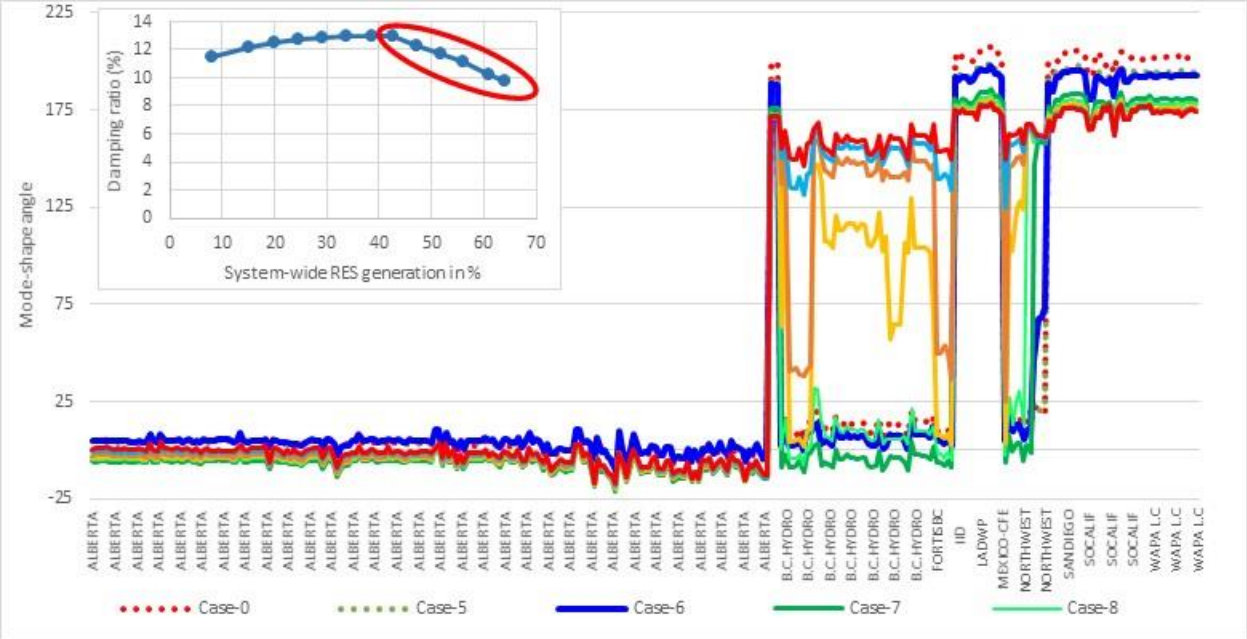

Figure 6-60. Comparison of mode shape of generators all cases in Scenario S4 for NS-A.

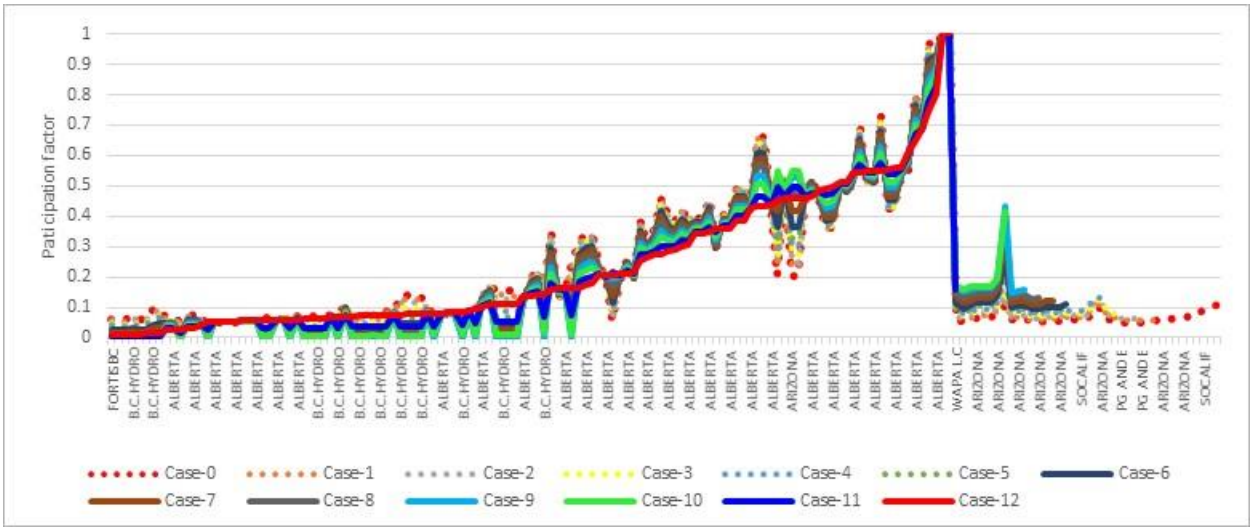

Figure 6-61. Participation factors of generators for all cases in Scenario S4 for NS-A.

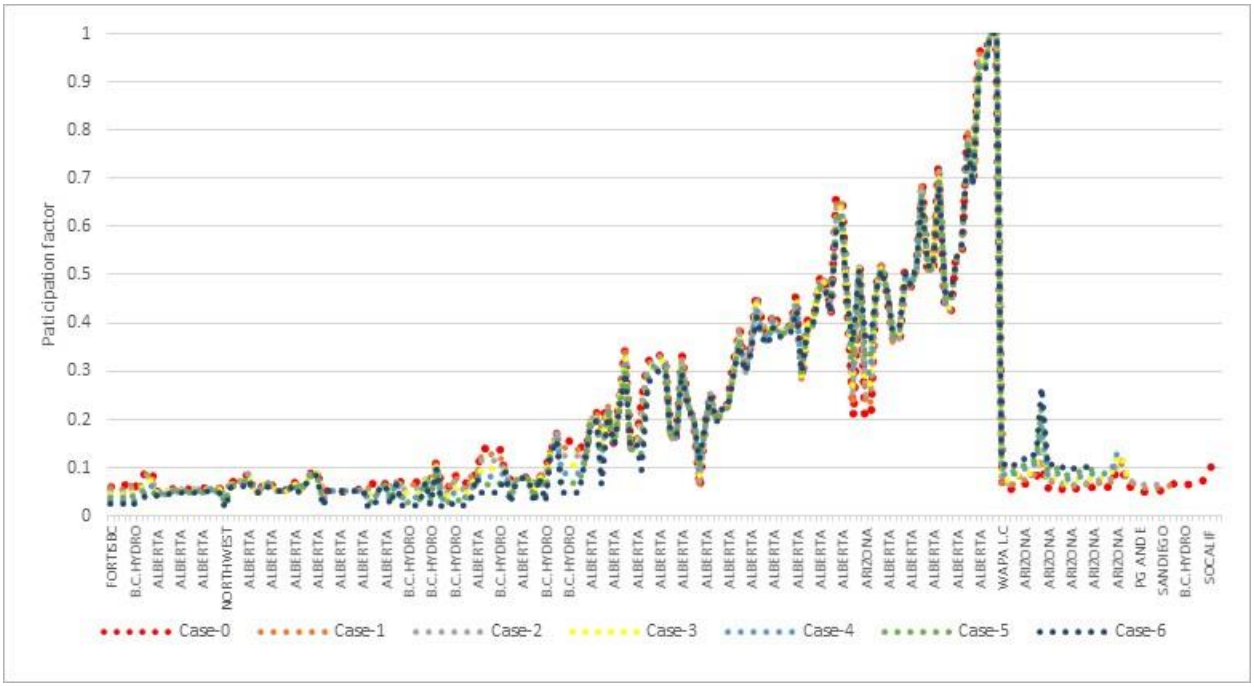

Figure 6-62. Participation factor of generators in several areas for cases 0–6 in Scenario S4 for NS-A.

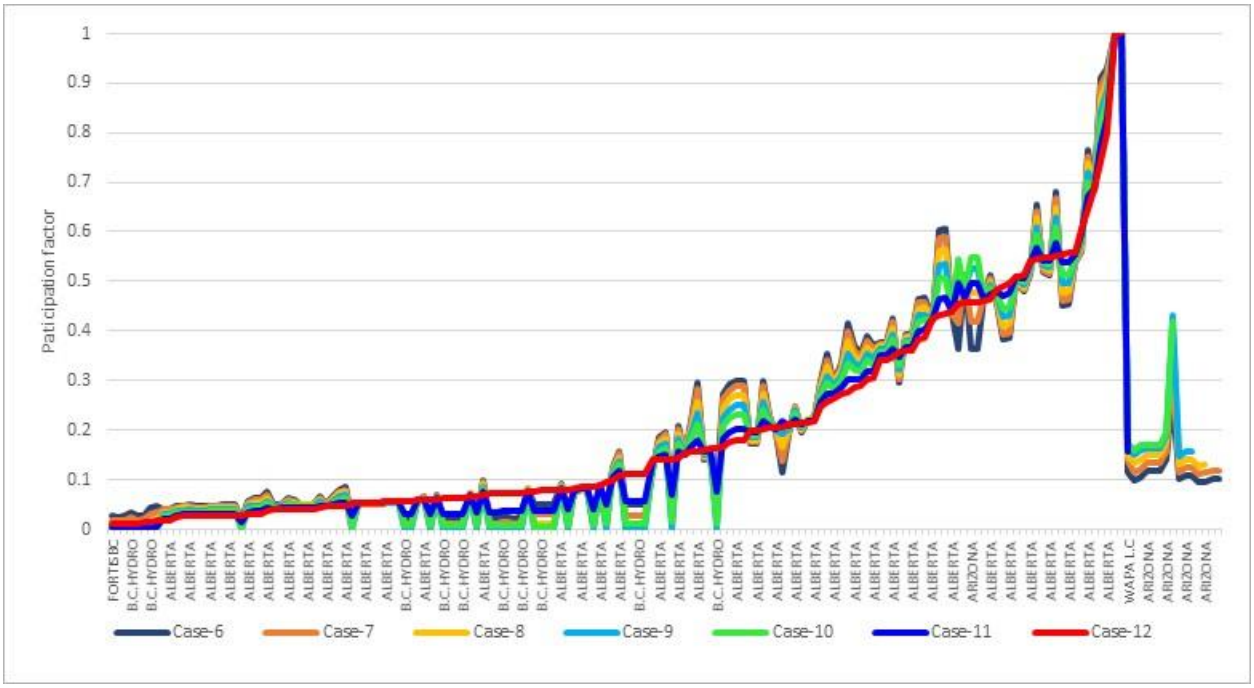

Figure 6-63. Participation factor of generators for cases 6–12 in Scenario S4 for NS-A.

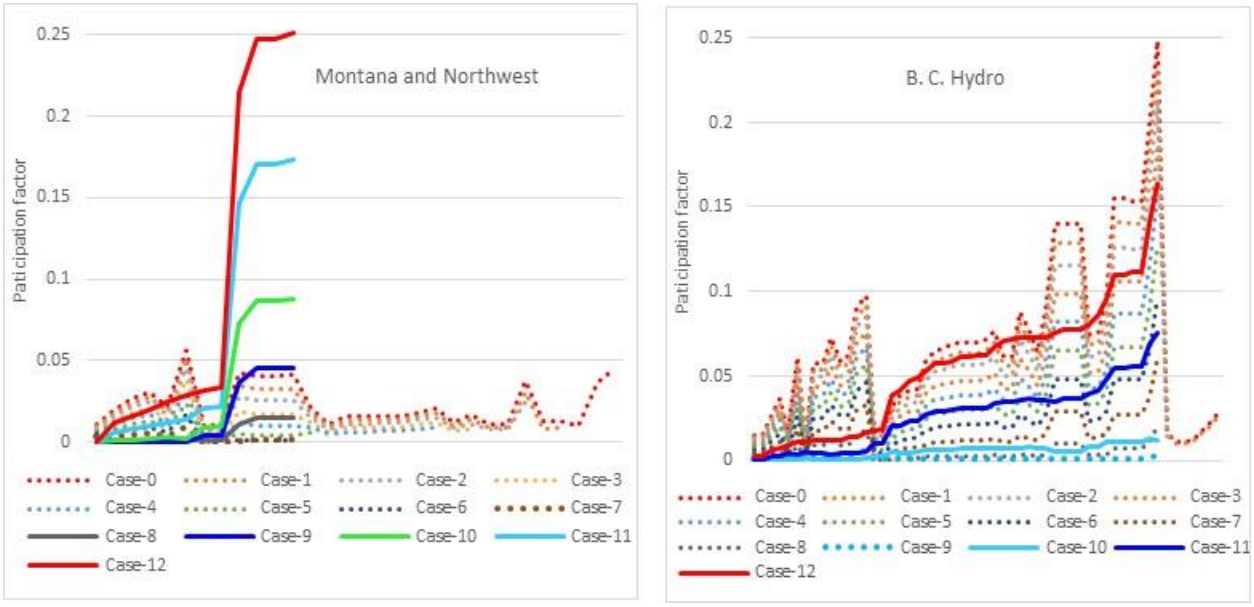

Figure 6-64. Participation factor of generators in B.C. Hydro, Montana, and the Northwest for all cases in Scenario S4 for NS-A.

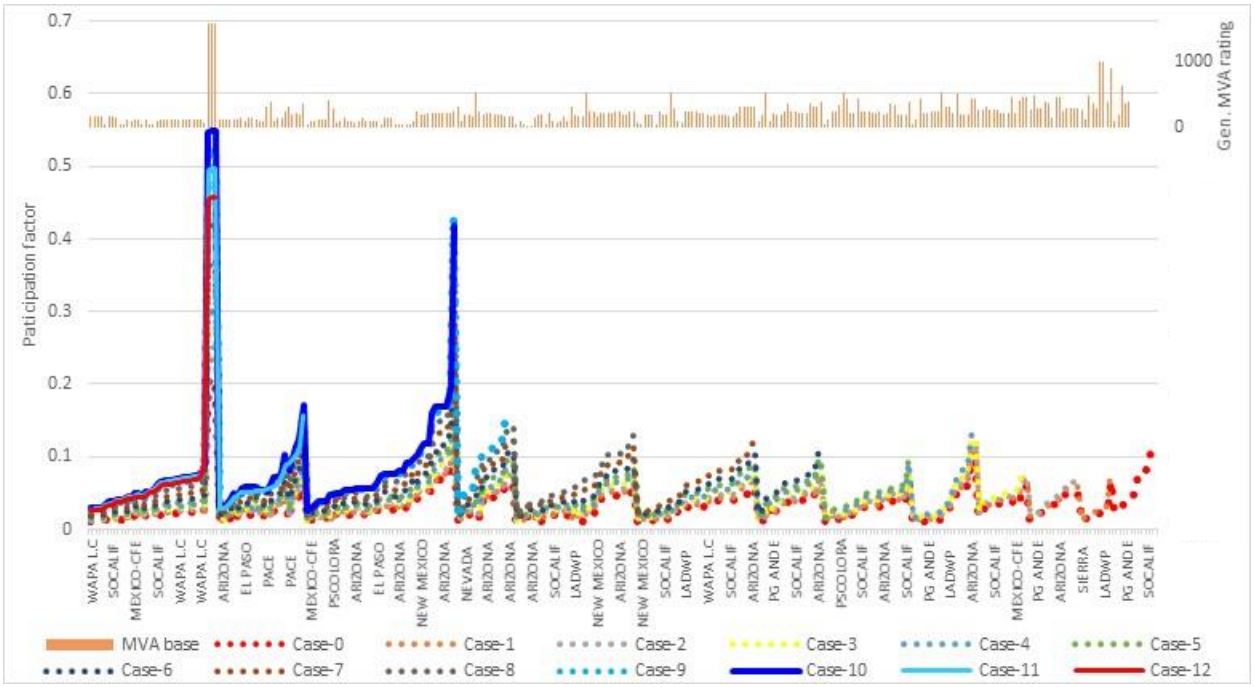

Figure 6-65. Participation factor of generators in areas not including Alberta, B.C. Hydro, Montana, and the Northwest for all cases in Scenario S4 for NS-A.

6.5.4.2 Eigenvalue Analysis of NS-B

Figure 6-66 and Figure 6-67 show the variations observed in the mode shape and participation factor of generators with increased renewable penetration for NS-B. In Figure 6-67, participation factor of some generators included that had a value of at least 0.1 in the base case.

As seen in Figure 6-66, the shape of NS-B remained unchanged with increased renewable penetration level until Case-6. From Case-6 onward, some of the generators in PG&E started to oscillate with Alberta and other generators in the South against generators in the North. From Case-9 onward, all generators in PG&E started oscillating with Alberta. The mode shape of generators in other areas did not change as the synchronous generators were replaced throughout the system except in Alberta.

Also, as the generators were replaced in all areas except Alberta, the participation factor of generators in Alberta continuously dropped. The participation factor of most generators in B.C. Hydro did not change much until Case-10, after which it decreased as shown in Figure 6-67. The participation factor of some generators increased from base case until Case-10, after which it did not change much. Also, participation factor of generators in other areas not including Alberta, B.C. Hydro, Montana, and the Northwest did not change much until Case-6, after which it started increasing. For this case, it was difficult to identify justification to the trends observed in the damping ratio. The only explanation was the change in the mode shape of generators in PG&E and the increase in the participation factor of generators in the South.

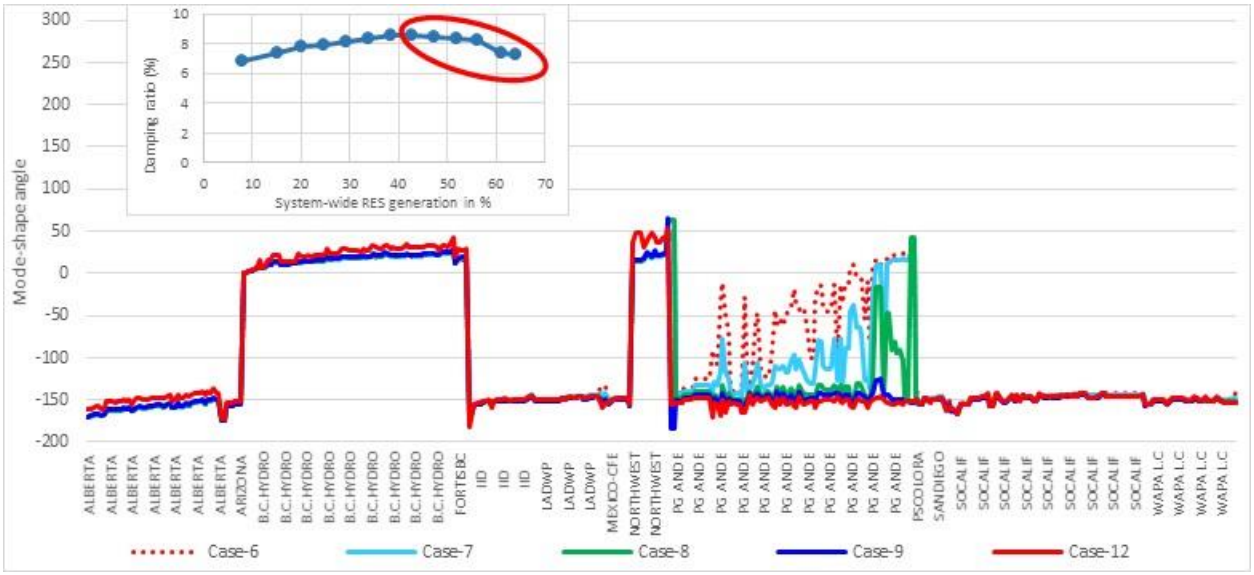

Figure 6-66. Comparison of mode shape of generators for selected cases in Scenario S4 for NS-B.

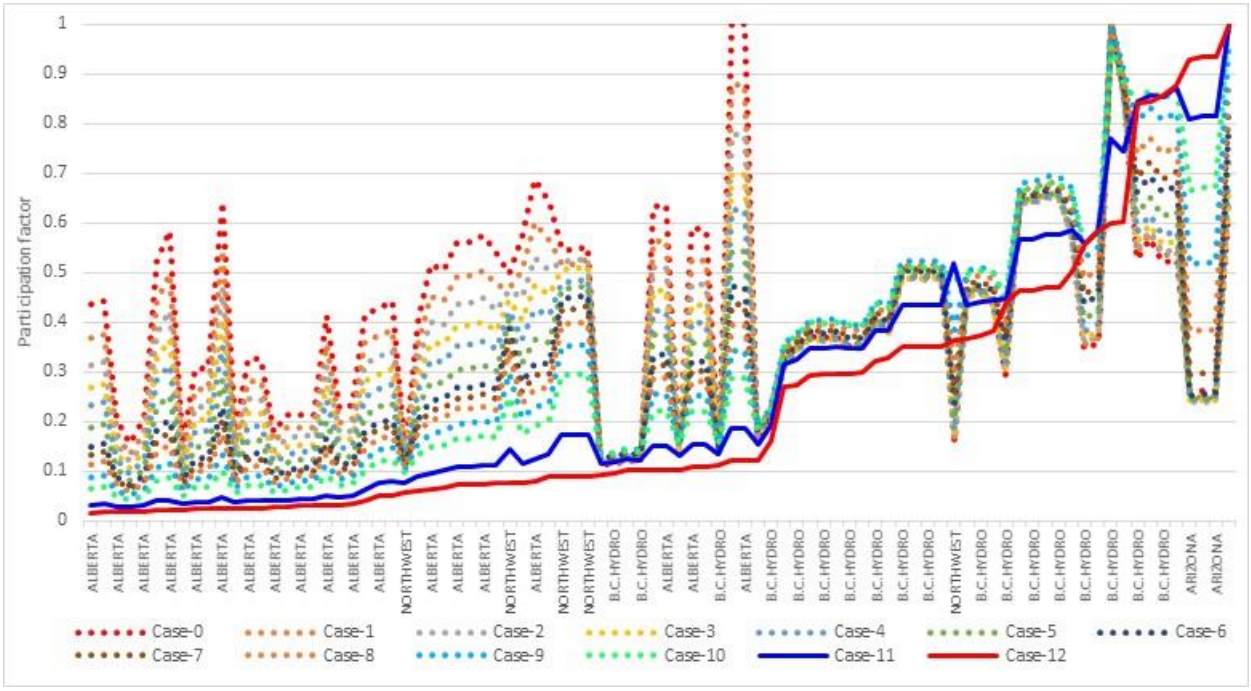

Figure 6-67. Participation factor of generators for all cases in Scenario S4 for NS-B.

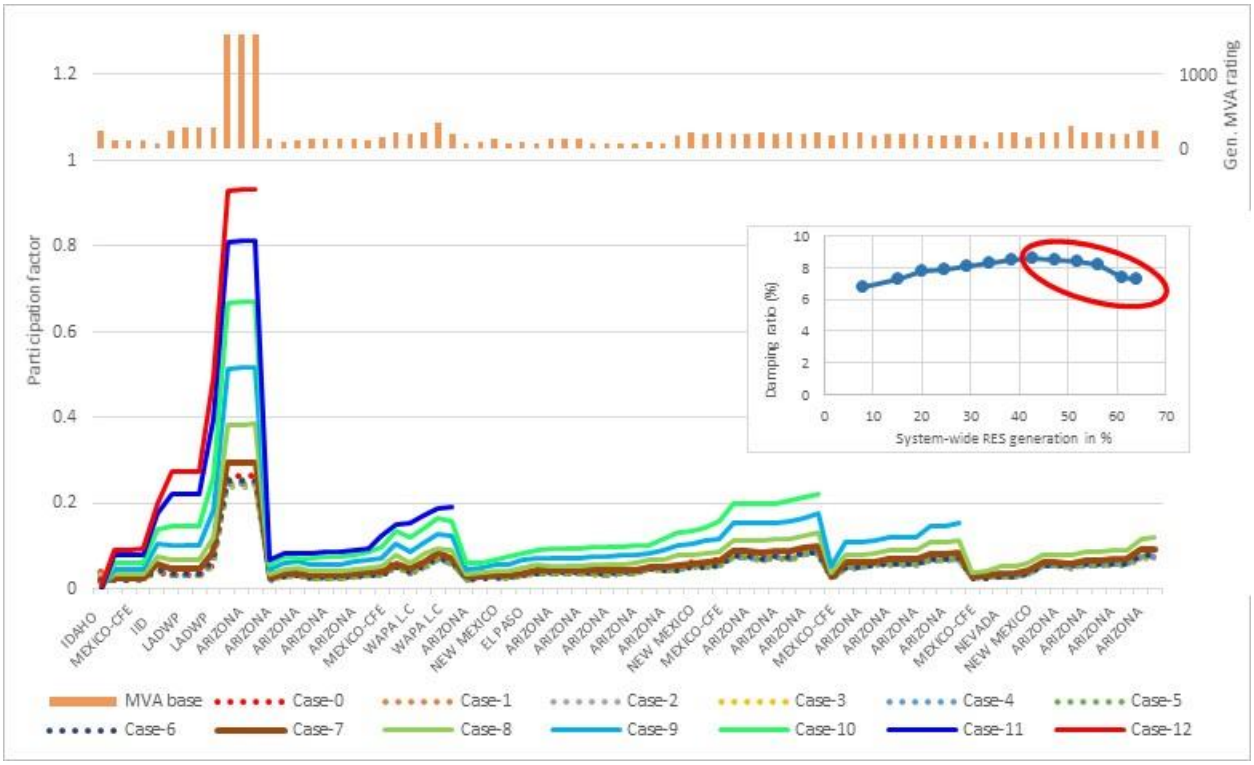

Figure 6-68. Participation factor of generators in several areas not including Alberta, B.C. Hydro, Montana, and the Northwest for all cases in Scenario S4 for NS-B.

6.6 Summary

Table 6-2 summarizes model-based wide-area oscillation assessment with respect to future operation scenarios with high-RES penetration for the HS load WECC model. Five scenarios of future generation-mix scenarios are investigated: Scenario S1 is systemwide RES high-penetration level up to 70% in the whole WECC system; Scenario S2 reverses the order of generators replaced in Scenario S1; Scenario S3 increases renewable penetration level in Alberta only; Scenario S4 increases renewable penetration in all areas except Alberta; and Scenario S5 looks at significant decrease in the COI power flow from north to south caused by an increased RES generation in the south of WECC.

As shown in Table 6-2. , under heavy load operation conditions of the WECC system:

- For NS-A, the systemwide RES generation increase will change damping ratio for Scenarios S1 and S2 depending on which generators are replaced. For Scenario S1, the damping ratio initially did not change much and then it decreased sharply. The trend reversed by reversing the order of replacing generators in Scenario S2.
- For NS-A, increasing renewable penetration level only in Alberta will result in decreased damping ratio.

- For NS-A, increasing renewable penetration throughout the system except in Alberta decreases damping ratio slightly.
- For NS-A, the DR will decrease if COI flow decreases from north to south as a result of an increased RES generation in the south of WECC.
- For NS-B, the generation-mix change with high-RES penetration does not have a significant impact on the damping ratio.

The trends observed in the damping ratio and frequency of modes cannot be directly related to the renewable penetration level or system inertia. These trends are in fact determined by which generators are replaced and how remaining synchronous generators interact among each other with respect to their mode shape and participation factor.

Table 6-2. Summary of impact of RES penetration level increase on the inter-area oscillation modes – model-based assessment.

Scenarios	Damping Ratio (%)		Frequency (Hz)	
	NS-A	NS-B	NS-A	NS-B
Systemwide RES increase (S1, S2)	Depends on generator being replaced	Not significant	Increase	Increase
Area-specific RES increase in Alberta only (S3)	Decrease	Not significant	Increase	Increase
Systemwide increase in all areas except in Alberta (S4)	Depends on generator being replaced	Not significant	Increase	Increase
Increase in RES in south and decrease in COI + PDCI flow (S5)	Increase	Not significant	Decrease	Not significant

The trends obtained from the data-based assessment, which is summarized in Table 5-18, can be explained by the model-based detailed assessment, results of which is summarized in Table 6-2. The decreasing trend of damping ratio of NS-A with increased solar and wind generation indicates that the specific group of generators taken offline when renewable generation is high results in the decrease of the damping ratio of NS-A. The trend observed in the damping ratio and frequency of NS-A with increased COI power flow aligns well with the model-based assessment results.

7.0 Conclusion

In this report, we have presented how changes in generation mix can impact the frequency and DR of WECC wide-area oscillation modes. Thorough data- and model-based analyses were performed to analyze the current trends and then extended to evaluate oscillation behaviors of the future WECC system. More than one year of past WECC PMU data and generation-mix data were analyzed to determine the correlation and past trends between the penetration level of RES and the wide-area oscillation modes. Past WECC operation models were also collected, and a model-based wide-area oscillation assessment was conducted to validate the data-based oscillation assessment and trending analysis results. Furthermore, the model-based analysis was extended to study and correlate future system oscillation trends with multiple future generation-mix scenarios with a very high penetration of RES in the WECC system. Both the data-based and model-based trending analyses showed that high penetration of RES has a significant impact on the wide-area oscillation modes in WECC.

The data-based correlation analysis results had the following findings:

- The DR of NS-A will decrease with the increase of the penetration level of solar and wind generation.
- The DR of both NS-A and NS-B will decrease with the increase of COI power flow (from north to south).
- Impact from the increase of the penetration level of solar and wind generation on the DR of NS-B is not clear; in other words, the data-based correlation analysis does not show a strong correlation between the DR of NS-B and the solar and wind generation penetration level.

It should be noted that the data-based correlation analysis was configured to capture changes in one variable relative to another variable in the data set while the other variables remained at the same value. The results do not indicate causality, more specifically, no particular cause and consequence relationship can be drawn.

The model-based wide-area oscillation assessment with respect to future operation scenarios with high RES penetration for the HS load WECC model showed that:

- For NS-A, the systemwide RES generation increase will change damping ratio for Scenarios S1 and S2 depending on which generators are replaced. For Scenario S1, the damping ratio initially did not change much and then it decreased sharply. The trend reversed by reversing the order of replacing generators in Scenario S2.

- For NS-A, increasing renewable penetration level only in Alberta will result in decreased damping ratio.
- For NS-A, increasing renewable penetration throughout the system except in Alberta decreases damping ratio slightly.
- For NS-A, the DR will increase if COI power flow decreases from north to south as a result of an increased RES generation in the south of WECC.
- For NS-B, the generation-mix change with high RES penetration does not have a significant impact on the damping ratio.

It should be noted that the trends observed in the damping ratio and frequency of modes, are in fact determined by which generators are replaced and how remaining synchronous generators interact among each other with respect to their mode shape and participation factor. In addition, throughout the grid transformation the generator controls in general and dampening devices have a prominent impact; therefore, interconnection wide generation unit retirement decisions should be taken with such impacts on the future system performance in mind, to ensure relevant planning studies are performed to identify potential issues, and implement mitigatory measures as an integral part of the preparations for fleet retirement planning.

The trends obtained from the data-based assessment, summarized in Table 5-18, can be explained by the model-based detail assessment, summarized in Table 6-2. The decreasing trend of damping ratio of NS-A with increased solar and wind generation indicates that the specific group of generators taken offline when renewable generation is high results in the decrease of the damping ratio of NS-A. The trend observed in the damping ratio and frequency of NS-A with increased COI flow aligns well with the model-based assessment results.

Going forward, it is important to determine the changes in system oscillatory behavior and potential new oscillation modes as RES penetration level increases, while synchronized resources retire, new IBR control strategies emerge, and the transmission infrastructure evolves. Additional advanced control strategies for the IBRs, as well as novel control strategies to dispatch conventional synchronized generation as well as IBRs, to stabilize the wide-area oscillation modes, should be explored and evaluated through close collaborations among national laboratories' teams, academia, manufacturers, and the industry.

8.0 References

Agrawal, U., & Pierre, J. W. (2019). Visual Validation of Estimated Parametric Models of Power Systems Under Ambient Conditions. *Proceedings of the 52nd Hawaii International Conference on System Sciences.* Maui, HI.

Anderson, M. G., Zhou, N., Pierre, J. W., & Wies, R. W. (2005). Bootstrap-based confidence interval estimates for electromechanical modes from multiple output analysis of measured ambient data. *IEEE Transactions on Power Systems, 20*(2), 943-950.

Cohen, J., Cohen, P., West, S. G., & Aiken, L. S. (2002). *Applied multiple regression/correlation analysis for the behavioral sciences.* Psychology Press.

Du, W., Wang, H., & Dunn, R. (2009). Power system small-signal oscillation stability as affected by large-scale PV penetration. *2009 International Conference on Sustainable Power Generation and Supply* (pp. 1-6). IEEE.

Durkay, J. (2016). State renewable portfolio standards and goals. *National Conference of State Legislatures.* Retrieved from https://www.ncsl.org/research/energy/renewable-portfolio-standards.aspx

Eftekharnejad, S., Vittal, V., Heydt, G. T., Keel, B., & Loehr, J. (2013). Small signal stability assessment of power systems with increased penetration of photovoltaic generation: A case study. *IEEE Transactions on Sustainable Energy, 4*, 960-967.

EIA. (2019). *Hourly Electric Grid Monitor*. Retrieved 3 1, 2020, from https://www.eia.gov/electricity/gridmonitor/dashboard/electric_overview/regional/REG-NW

Elliott, R., Byrne, R., Ellis, A., & Grant, L. (2014). Impact of increased photovoltaic generation on inter-area oscillations in the Western North American power system. *2014 IEEE PES General Meeting| Conference & Exposition* (pp. 1-5). IEEE.

Hahn, J. (1995). Bootstrapping Quantile Regression Estimators. *Econometric Theory, 11*(1), 105–121 .

Hauer, J., Demeure, C., & Scharf, L. (1990). Initial results in Prony analysis of power system response signals. *IEEE Transactions on Power Systems*, 80-89.

Huang, Z., Zhou, N., et al. (2010). *Mango-modal analysis for grid operation: A method for damping improvement through operating point adjustment.* Richland, WA: Pacific Northwest National Lab. (PNNL-19890).

Koenker, R. (1994). *Confidence Intervals for Regression Quantiles.* (P. Mandl, Ed.) Heidelberg: Physica-Verlag HD.

Koenker, R., & Hallock, K. F. (2001). Quantile regression. *Journal of economic perspectives, 15*(4), 143-156.

Leys, C., Ley, C., Klein, O., Bernard, P., & Licata, L. (2013). Detecting outliers: Do not use standard deviation around the mean, use absolute deviation around the median. *Journal of Experimental Social Psychology , 49*(4), 764-766.

Makarov, Y. V., Lu, S., et al. (2011). Integration of uncertainty information into power system operations. *IEEE Power and Energy Society General Meeting* (pp. 1-13). Detroit, MI: IEEE.

NERC. (2017). *NERC Reliability Guideline Forced Oscillation Monitoring & Mitigation.* NERC. Retrieved from https://www.nerc.com/comm/PC_Reliability_Guidelines_DL/Reliability_Guideline_-_Forced_Oscillations_-_2017-07-31_-_FINAL.pdf

NERC. (2019a). *NERC Detailed Event Analysis.* NERC. Retrieved from https://www.nerc.com/comm/PC/SMSResourcesDocuments/Detailed_Event_Analysis.pdf

NERC. (2019b). *NERC Interconnection Oscillation Analysis.* NERC. Retrieved from https://www.nerc.com/comm/PC/SMSResourcesDocuments/Interconnection_Oscillation_Analysis.pdf

Pierre, J., Trudnowski, D., & Donnelly, M. (1997). Initial results in electromechanical mode identification from ambient data. *IEEE Transactions on Power Systems*, 1245-1251.

PNNL. (2019). *Archive Walker Software*. Retrieved from GitHub: https://github.com/pnnl/archive_walker

PowerWorld Simulator. (2020). Retrieved from https://www.powerworld.com/

Quint, R. D. (2019). *NERC Eastern Interconnection Oscillation Disturbance January 11, 2019 Forced Oscillation Event.* NERC. Retrieved from https://www.nerc.com/pa/rrm/ea/Documents/January_11_Oscillation_Event_Report.pdf

Quintero, J., Vittal, V., Heydt, G. T., & Zhang, H. (2014). The impact of increased penetration of converter control-based generators on power system modes of oscillation. *IEEE Transactions on Power Systems, 29*(5), 2248-2256.

Shah, R., Mithulananthan, N., & Bansal, R. (2012). Damping performance analysis of battery energy storage system, ultracapacitor and shunt capacitor with large-scale photovoltaic plants. *Applied energy, 96*, 235-244.

Shah, R., Mithulananthan, N., & Bansal, R. (2013). Oscillatory stability analysis with high penetrations of large-scale photovoltaic generation. *Energy Conversion and Management, 65*, 420--429.

Shah, R., Mithulananthan, N., Sode-Yome, A., & Lee, K. Y. (2010). Impact of large-scale PV penetration on power system oscillatory stability. *IEEE PES general meeting* (pp. 1-7). Minneapolis: IEEE.

Sierra Club. (2019). 100% Commitments in Cities, Counties, & States. Retrieved from https://www.sierraclub.org/ready-for-100/commitments

Smith, E. M. (1967). Least square regression lines: Calculations assuming a constant percent error. *Journal of Chemical Education, 44*(12), 757.

Tamimi, B., Cañizares, C., & Bhattacharya, K. (2011). Modeling and performance analysis of large solar photo-voltaic generation on voltage stability and inter-area oscillations. *2011 IEEE Power and Energy Society General Meeting* (pp. 1-6). Detroit: IEEE.

Trudnowski. (2012). *Properties of the Dominant Inter-Area Modes in the WECC Interconnect.* Butte MT: Montana Tech.

Trudnowski, D. J., Pierre, J. W., Zhou, N., Hauer, J. F., & Parashar, M. (2008). Performance of Three Mode-Meter Block-Processing Algorithms for Automated Dynamic Stability Assessment. *IEEE Transactions on Power Systems*, 680-690.

Trudnowski, D., Johnson, J., & Hauer, J. (1999). Making Prony analysis more accurate using multiple signals. *IEEE Transactions on Power Systems*, 226-231.

WECC JSIS. (2013). *Modes of Inter-Area Power Oscillations in Western Interconnection.* Retrieved from https://www.wecc.org/oc/Pages/jsis.aspx

You, S., Kou, G., Liu, Y., et al. (2017, March). Impact of high PV penetration on the inter-area oscillations in the US eastern interconnection. *IEEE access, 5*, 4361-4369.

Pacific Northwest
NATIONAL LABORATORY

www.pnnl.gov

902 Battelle Boulevard
P.O. Box 999
Richland, WA 99352
1-888-375-PNNL (7665)

U.S. DEPARTMENT OF
ENERGY